Fundamentals of micro-particle removal by liquid oxide

Fundamentals of micro-particle removal by liquid oxide

By

Mukesh Kumar Sharma, B.E., M.Sc.

A Thesis

Submitted to the School of Graduate Studies

In Partial Fulfilment of the Requirements

for the Degree

Doctor of Philosophy

McMaster University

DOCTOR OF PHILOSOPHY (2019) **McMaster University**
(Materials Science and Engineering) **Hamilton, Ontario**

Title: Fundamentals of micro-particle removal by liquid oxide

Author: Mukesh Sharma, M.Sc. (IIT Kharagpur)

Supervisor: Dr. Neslihan Dogan (McMaster University)

Number of Pages: xv,168

Abstract

The grades of steel used for automotive bodies are interstitial free steel grades and titanium stabilized ultra-low carbon steel grades. During the manufacturing of these grades, the addition of titanium in liquid steel is achieved in the steel refining units and may cause processing problems. Titanium reacts with the dissolved aluminum and oxygen to form complex solid aluminum titanate type micro-particles (inclusions). During the flow of titanium alloyed steel grades containing solid inclusions (such as aluminum titanate and alumina type inclusions), the clog accompanied by steel skull can be formed at the submerged entry nozzle between the tundish and the mold. To reduce the effects of aluminum titanate type inclusions, they can be either modified or removed.

The current study focused on the removal of Al_2O_3, TiO_2, and Al_2TiO_5 inclusions by dissolving them in slag in the temperature range of 1430 – 1600 °C using a high-temperature confocal scanning laser microscope. In this technique, a single particle (inclusion) is placed on the surface of a solid slag, and the inclusion-slag system is heated to steelmaking temperatures. The dynamic changes in inclusion size are measured to determine dissolution kinetics and mechanism.

This work has developed a complex oxide particle synthesis technique and provides the first-ever kinetic data for removal of aluminum titanate inclusions into steelmaking slags. It is found that Al_2O_3 inclusions have a slower dissolution rate than that of Al_2TiO_5 inclusions followed by TiO_2 inclusions. The rate-controlling steps are investigated using a shrinking core model. It is shown that the rate-controlling step for dissolution of both Al_2O_3

and Al_2TiO_5 inclusion types is the mass transfer of alumina. Evidence in support of this finding is the particle-slag interface characterization by line scan analysis and calculated diffusivity values being inversely proportional to the viscosity of slag.

The dissolution path of aluminum titanate is proposed in the following steps. First, aluminum titanate dissociates into alumina, titanium oxide and oxygen while slag penetrates through the particle. In the next step, the alumina and titanium oxide dissolves in slag, and the oxygen leaves the system. The existence of gas bubbles enhances the overall rate of Al_2TiO_5 dissolution.

The current work establishes a detailed understanding of the dissolution of Al-Ti-O type inclusions in steelmaking slags. This knowledge will inform steelmakers on which inclusions of different chemistry can be removed preferably and develop strategies on better slag design to produce superior quality steel with reduced operational downtime.

Acknowledgements

I take this opportunity to express my deep gratitude to my supervisor, Dr. Neslihan Dogan for her invaluable guidance and constant inspiration throughout the Ph.D. program. You provided invaluable insights into enriching my research work to bring it from zero to the place it stands now. I want to thank Dr. Ken Coley in changing my way to approach a problem and to build a solution. I would extend my thanks to Dr. Joseph McDermid, who made me realize the bigger picture of errors in engineering and how they can be game-changing. The invaluable guidance and enthusiasm by all three of you motivated me to work to my full potential. It is under the scrutiny of my work at the supervisory committee meetings that it stands strong.

I would also like to thank my friends in the McMaster Pyro Metallurgy Group for their help and support throughout the last five years. It was a great pleasure for me to spend time at group meetings. Thank Yousef Tabatabaei for all the pre-review of the papers and the extremely useful squash time. Thank you Aliyeh Rafiei, Michelia Alba, Ameya Kadrolkar, Kezhuan Gu and Brian Jamieson for their help and support.

I am also thankful to all my friends outside the laboratory premises. Thank you, Josh, for all the coffee walks. Thanks to Diyar for all the good talks and lunch. Thank to Dr. Anthony Petric for teaching me thermodynamics. The work would have never got off without the help of Professor Yurij Mozharivskyj, Dr. Hanna Dabkowska, Dr. Jim Britten and Victoria Jarvis, from the department of chemistry at McMaster University. I want to

thank Doug Culley, Ed McCaffery, and Xiaogang Li for the help and support with the research.

It would be a lie if I would say this research is all my hard work. This work is by the support of everyone mentioned above and my family. I want to express my gratitude to my family members who are in my thoughts every moment I spent during my Ph.D. My brother Rakesh, who despite being younger to me, is my philosophical guru who taught me about the purpose of life. My sister Rinki, who provided emotional support and encouragement throughout the last five years. To my sister in law who holds the family together along with my brother. To my mother, who literally showed us that tough people last longer than tough times. She showed us that education is the only way out of tough situations. I want to thank my father, who supported me with all confidence and complete trust when it came to education. I would also like to thank my uncle, who taught us the values in life. Last but not least, I would like to thank my nephews Rudransh and Rajvir, who are the source of motivation for me to keep moving forward every day.

Table of Contents

List of Figures

List of Tables

Chapter 1
Introduction

1.1 Motivation

Titanium is an important alloying element in the production of automotive body steel grades. It combines with the interstitial elements in steel such as oxygen, nitrogen, and carbon to form titanium carbides, titanium nitrides, and complex carbon nitrides [1–3]. These compounds reside at the grain boundaries and impede the motion of dislocations during deformation. The pinning action by carbides and nitrides enhances the strength and formability of these steels [3–7].

In stainless steel grades such as those from 300 and 400 series, titanium plays an important role in protecting the steel against sensitization [8–11]. The phenomenon of sensitization can be described as the reaction of chromium with carbon in the temperature range of 773 K-1073 K to form chromium carbides. This reaction leads to depletion of chromium in the steel. When chromium is considerably less (< 10.5 pct.), that steel is not referred to as stainless steel. The addition of titanium and accurate heat treatment stabilize the steel and prevent sensitization [8].

Although titanium is beneficial for enhancing the mechanical properties of steel, its presence in liquid causes unwanted upstream processing problems [12–14]. During the steel refining process, aluminum is added to the steel to reduce the excessive amount of dissolved oxygen. The dissolved aluminum and oxygen react to form solid alumina inclusions in the liquid steel. After that, titanium is added to provide desired mechanical properties in the finished product. On addition of titanium, the alumina inclusions in the liquid steel further react with titanium and form solid Al-Ti-O inclusions. The alumina and Al-Ti-O type inclusions stick to the wall of the submerged entry nozzle (SEN). The inclusions adhering to the walls hinder the path of the flowing steel. This can lead to two major deleterious consequences [6,13,15,16]. The first effect is the formation of slivers. The inclusions can detach and fall during casting to appear as surface defects called slivers in the rolled products [5]. The second effect is the clogging of SEN, which can reduce the flow of steel during the continuous casting process. An industrial study by Basu et al. [13] on clogging behavior suggested that steel containing titanium congests SEN more aggressively than steel without any titanium. The clog mass in a titanium alloyed steel consists of powdery inclusions of alumina, spinel, and aluminum titanium oxides along with a frozen steel skull. The secondary effect of clogging is poor titanium recovery at the caster and mold level fluctuations [14].

Removing inclusions from liquid steel to slag in the ladle, tundish, or mold before casting can minimize the issues discussed above. However, to the author knowledge, there is only one study [1] focusing on the dissolution of Ti –containing inclusions available in the open literature. Given the industrial importance of Ti containing inclusion removal in steelmaking, this area requires fundamental study to fill key knowledge gaps in this area.

1.2 Objectives of this study

The overarching aim of this research is to develop a fundamental understanding of the dissolution mechanism of titanium-containing inclusions during the refining of titanium alloyed steel using high-temperature confocal scanning laser microscopy. The research objective was accomplished through the following sub-objectives:

1. Produce high purity and dense titanium-containing particles (inclusions) which are not available from reagent suppliers.
2. Assess the phase stability and reactivity of the liquid slag and inclusion systems through thermodynamic modeling.
3. Obtain experimental kinetic data for inclusion dissolution as a function of slag composition, inclusion composition, and temperature.
4. Determine the dissolution mechanism of inclusions by applying modeling techniques and characterizing the slag-inclusion interface.

The new data generated will have an important bearing on future steel processing and will act as a precursor for further research. The steel industry is currently working on a whole new generation of steels, which differ significantly in composition from those currently produced. This will inevitably lead to a new range of inclusion types which will require detailed study to optimize the processing.

1.3 Thesis outline

This thesis consists of seven chapters. Chapter 1 provides a general introduction to the research; describing the motivation for this study, defining detailed research objectives and presenting an outline of this thesis. Chapter 2 reviews relevant literature from non-metallic inclusion dissolution studies using CSLM. A brief discussion regarding the secondary steelmaking and inclusion modification is presented. A critical analysis of mathematical models proposed in the literature to determine the rate-controlling mechanism is included. Chapter 3 introduced the use of the OFZM as a potential technique for the preparation of pure and dense non-metallic inclusion particles. This chapter is published in Steel Research International. Chapter 4 is titled “In situ observation of dissolution of oxide inclusions in steelmaking slags”. This chapter presents the results of a laboratory investigation on the effect of inclusion composition on the dissolution rates in steelmaking slag. It is published in the Journal of Mining, Metals and Materials Society. Chapter 5 is titled “Dissolution behavior of aluminum titanate inclusions in slag”. This chapter explains the dissolution path and mechanism of aluminum titanate inclusions. This chapter is submitted for publication in the Metallurgical and Materials Transactions B. Chapter 6 is titled “Effect of slag composition on dissolution behavior of aluminum titanate inclusions”. This chapter is to be submitted to the Journal of Mining, Metals, and Materials Society. This chapter compares the dissolution rate of aluminum titanate inclusions in three Al_2O_3-CaO-SiO_2 type slags at 1773 K. Chapter 7 draws conclusions from the thesis work and explains the importance of this work and offers future works and directions.

Chapter 2
Literature review

2.1 Overview of the steelmaking process

Steel is produced by two main routes [17]. The first process is the electric arc furnace (EAF), where the heat required for the steelmaking process is provided by an electric arc produced between three graphite electrodes and the metallic charge. Heat is also obtained by reaction of impurities in the steel melt with oxygen. The oxygen is supplied through a lance [18]. The charge used in EAF is recycled scrap, hot metal from the blast furnace, or iron ore bearing pellets [17]. The second process is the basic oxygen furnace (BOF), where oxygen is blown into the hot metal to produce steel. Since basic refractories are used and oxygen is blown, the process is called a basic oxygen process [19]. The charge used in BOF are recycled steel scrap and hot metal obtained from the blast furnace. After the primary steelmaking, molten steel is treated separately in a ladle to design the composition as required by the customer. The series of operations carried out on molten steel is called secondary steelmaking [17,20]. After processing for secondary steelmaking, the molten steel is sent to the mold then to the caster [20]. At the end of the caster, solid steel is obtained which can be rolled to shipment or further processed as desired. Figure 2-1 shows an overview of the steelmaking processes, including BOF, secondary steelmaking, and casting [21].

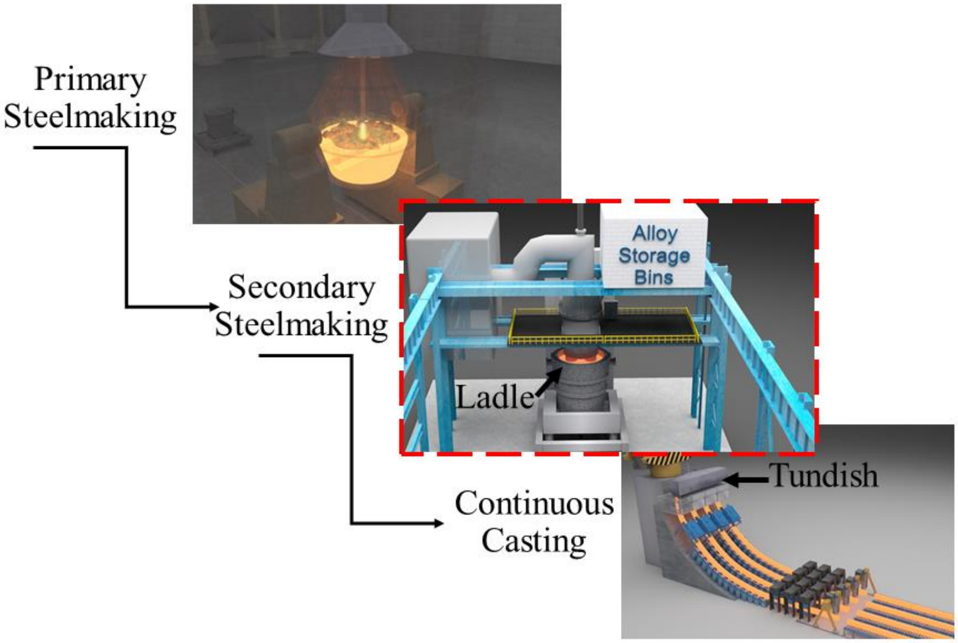

Figure 2-1 Overview of the steelmaking process showing primary steelmaking, secondary steelmaking and continuous casting [21]

2.2 Secondary Steelmaking

Secondary steelmaking is crucial to current steel makers because of the flexibility it presents in fine-tuning the composition of the steel obtained from the primary steelmaking. The unit processes in secondary steelmaking can be placed into four categories [19,22].

1. Stirring processes: This process includes passing of argon gas through liquid steel. The gas is purged either through a porous plug at the bottom or a submerged lance through the top [19]. The purpose of stirring is to achieve chemical homogenization of the bath. The operation of stirring can be classified as hard or soft, depending on the amount of energy used. A top slag can be used along with bottom stirring to

enhance slag metal interaction. The purpose of increased slag metal contact is to promote desulfurization and deoxidation [19,23].

2. Injection processes: This process involves injecting a material into liquid steel. The material is injected through a cased wire, through a submerged lance with the help of a carrier gas or by stirring through the bottom and dumping the powder on the top. The purpose of injection processes is to achieve desulfurization, deoxidation, and alloying [23].

3. Vacuum processes: This process involves reducing the partial pressure of hydrogen, nitrogen, and carbon monoxide in the atmosphere of the reactor. The purpose is to lower the amount of interstitial hydrogen, nitrogen, and carbon in steel [19]. The degassing can be either vacuum stream degassing, ladle degassing, or recirculation degassing [19]. In vacuum stream degassing, the steel falls through a vacuum into another vessel. In ladle degassing, the steel is placed in an evacuated vessel and argon is purged through the bottom. In recirculation degassing, the liquid steel is circulated through an evacuated atmosphere. Examples of recirculation degassing are RH and DH processes [19].

4. Reheating processes: This process is used for temperature correction of the steel melt. Various processes in secondary steelmaking lead to temperature loss of metal to the surrounding. Besides, processes such as alloying and mixing are heat demanding. In order to compensate for the heat loss, the melt is heated in an additional process. The furnace used is called LF. Finkl-Mohr and VAD [19].

The oxygen, nitrogen, carbon, and sulfur contents of the steel, as well as the inclusions formed due to reactions within the steel melt, can be controlled to the desired effect. The application of secondary steelmaking can be explained as follows [24]:

1. Deoxidation

The oxygen level in liquid steel after processing in BOF is 600-1000 ppm [19]. The maximum amount of oxygen that can be dissolved in gamma iron is approximately 30 ppm [19]. If the steel is cast with a high content of dissolved oxygen, it causes defects such as gas holes and porosity in the cast product due to the evolution of carbon monoxide [25,26]. To prevent such defects, the dissolved oxygen is removed from molten steel by adding elements that have a strong affinity for oxygen such as Al, Si, Mn, Ca, Zr and Ce either individually or in combination [27,28]. In common deoxidizers, Al offers the strongest deoxidation, while Mn is the weakest deoxidizer [29]. The deoxidizer added to molten steel reacts with dissolved oxygen to form the corresponding oxide. A deoxidation reaction is shown in equation 2-1.

$$2[\mathrm{Al}] + 3[\mathrm{O}] = \mathrm{Al_2O_3(s)} \tag{2-1}$$

where square brackets refer to species dissolved in steel. The product is solid and remains suspended in liquid steel. The deoxidation power of any element depends on the activity of the deoxidant in steel and stability of its oxide in the slag.

2. Degassing and decarburization

Elements of gaseous species such as nitrogen, hydrogen, and oxygen remain dissolved in the liquid steel. However, their solubility in the solid product is close to negligible. While oxygen can be removed by deoxidation, nitrogen and hydrogen remain dissolved in steel. Low amount of nitrogen is preferred in deep drawing steel because it can prevent excessive cold working [30]. Nitrogen is essentially picked up by the interaction of steel with air. An excessive amount of hydrogen presents problems of formation of gaseous hydrogen, which lead to the formation of defects such as pinholes and blowholes [30]. Hydrogen is picked by liquid steel from moisture present in solid charges. A lower nitrogen and hydrogen contents in steel are achieved by degassing. The overall degassing reaction for hydrogen and nitrogen removal is represented by equation 2-2 and equation 2-3. The removal of hydrogen is fast during degassing while removal of nitrogen is relatively slow due to kinetic reasons. Carbon dissolves in steel melt up to 300 ppm [30]. For interstitial free steels, carbon is required at the levels of 25 ppm [13,14]. The amount of soluble carbon in liquid steel is lowered by reacting with oxygen as illustrated in reaction 2-4. To achieve this, circulation degassing reactors such as RH is used. The RH is modified by oxygen blowing under vacuum (RH-OB) to achieve ultra-low carbon level in the melt. The VOD process is used to manufacture ultra-low carbon steel grades [20].

$$[\mathrm{H}] = \frac{1}{2}\mathrm{H_2(g)} \tag{2-2}$$

$$[\mathrm{N}] = \frac{1}{2}\mathrm{N_2(g)} \tag{2-3}$$

$$[\mathrm{C}] + [\mathrm{O}] = \mathrm{CO(g)} \tag{2-4}$$

3. Desulfurization

Desulfurization is practiced by two principal methods depending on the level of desulfurization required. The first method is by dissolution in CaO saturated synthetic slag along with gas stirring. This type of desulfurization is performed in a separate ladle, LMF, or VAD. The second method is by injection of CaSi particles from a lance or via wire feeding. This method is employed when sulfur levels are desired at ultra-low levels of 10-20 ppm. The calcium from calcium silicide reacts with the sulfur and oxygen in steel [19].

4. Alloy addition

The chemistry of steel can be tailored to the desired composition during secondary steelmaking. Alloying can be done during vacuum treatment or gas stirring [19]. The alloys are grouped into two class [19]. Class 1 alloys include Fe-Si, Fe-Mn, and Fe-Ca where the melting point of ferroalloys is less than that of liquid steel. Class 2 alloys such as Mo, V, Nb, and W have a higher melting temperature than that of liquid steel. The kinetics of dissolution of class 2 ferroalloys is slower than that of class 1 ferroalloys. For alloying and minimizing alloy losses, the CAS (composition adjustment by sealed argon bubbling) process was developed by Nippon Steel [20]. Argon is blown through the bottom of the reactor creating a rising argon plume. The argon bubbling provides stirring, which enhances mass transfer of alloy within the melt. The plume is enveloped by a snorkel at the top which is partially immersed in liquid steel. Alloy addition is done at the top, where the snorkel covers the plume [20].

5. Inclusion formation and control

Inclusions are small particles embedded within the steel matrix. These particles are mostly non-metallic by nature. They can form (a) as a reaction product of deoxidation within the steel, (b) due to an erosion of refractories (c) reoxidation of flowing steel (d) during solidification of steel [20].

The sources of oxygen for reoxidation can be air aspiration from leakages at joints of refractories or nozzles [31], SiO_2, MnO or FeO from oxidizing ladle or tundish slags [13,32] or lining of SEN or tundish [13]. Reoxidation happens by transporting of oxygen from the melt surface to the bulk melt followed by precipitation and growth of inclusions within the steel melt [33]. The reoxidation of steel is of particular significance in the formation of Al-Ti-O type inclusions. Basu et al. [13] found that Al-Ti-O type inclusions form entirely due to reoxidation. They identified the sources of reoxidation and applied remedial steps to lower it. On the application of such corrective actions, the occurrence of reoxidation related to sliver defects on cold-rolled titanium alloyed ultra-low carbon steel sheets decreased from 80-85 % to 60 %. Since the formation of inclusions is unavoidable, the only way to minimize their effects on the steel cleanliness and defects is to control them.

The control of inclusions can be achieved by (a) modification of inclusions or (b) removal of inclusion. The most common way of modification of inclusion composition is the addition of calcium to the melt. For instance, solid alumina inclusion can react with calcium and form liquid calcium aluminates [34,35]. These liquid inclusions float out to the steel surface where they can be absorbed by the top slag and do not contribute to clogging as much as irregularly shaped alumina inclusions [17].

Another beneficial effect of calcium treatment is its effect on inclusion morphology [19]. Calcium addition controls the shape of manganese sulfide inclusions from elongated to globular in shape. The globular particles are less detrimental to the properties of steel in comparison to other inclusion shapes.

A challenge with calcium treatment is that its recovery is less than 10 % [19]. Thus, calcium is added in the form of Ca-Si, which provides a longer time for Ca to dissolve in comparison to pure Ca addition. Calcium is introduced in molten steel by two methods [36]. In the first method, Ca-Si particles are injected with the help of carrier gas through a submerged lance. The second method is calcium addition via wire feeding. The recovery of calcium is higher in wire feeding in comparison to the lance injection. In contrast, the use of cored wires is more costly than particles fed through the lance [36].

Rare earth metals such as cerium, tellurium, and selenium are also used to control the sulfide shape, and they improve hot working properties of steel [24]. Although cerium has better solubility than calcium, the high reactiveness of cerium increases its chance of reaction with refractories and atmosphere [19]. The density of cerium is similar to that of steel, which presents difficulty in its floatation. In addition, the inclusions formed by cerium in reaction with oxygen and sulfur in steel are fine and non-deformable. The factors mentioned above make cerium an unfavorable candidate for inclusion modification.

To the best knowledge of the author, there is no literature in the modification of aluminum titanate type inclusions and limited research available on the evolution of such inclusion types in steel [37]. Matsuura et al. [37] conducted high-temperature experiments to study the effect of the sequence of addition of Al and Ti to molten iron on inclusion evolution at 1873 K. They reported that the spherical Al_2O_3 inclusions are formed after the deoxidation by dissolved Al. These inclusions grow in the melt resulting in a decrease in the concentration of Al locally. Thus, TiOx or Al-Ti-O type oxides are formed on the surface of existing Al_2O_3 inclusions. These inclusions are polygonal in shape, which is more prone to agglomeration. Thus, the morphology of inclusion is modified during evolution, which affects the agglomeration and hence clogging tendency [37].

2.3 Clogging phenomena during continuous casting

After treatment in the ladle, the molten steel with solid inclusions is transferred to a tundish as part of the casting process. The tundish is a shallow vessel with dams and weirs to control the flow of steel [38]. The steel exits the tundish through an upper tundish nozzle. A slide gate exits at the bottom of the upper tundish nozzle to control the flow. Beyond the slide gate, it joins another nozzle called the submerged entry nozzle through which the steel enters the mold. The lower end of the submerged entry nozzle can have one or more ports to deliver the steel into the mold. Figure 2-2 shows a schematic of a steel transfer from the tundish to the mold [39]. As liquid steel passes through the submerged entry nozzle, some regions within the nozzle can be clogged due to the presence of inclusions as highlighted in Figure 2-2. Nozzle clogging can cause problems such as mold level fluctuation or trapped impurities in cast product [12,39,40]. These inclusions act as stress raisers [41] in the final product and are harmful to the mechanical properties of the cast product.

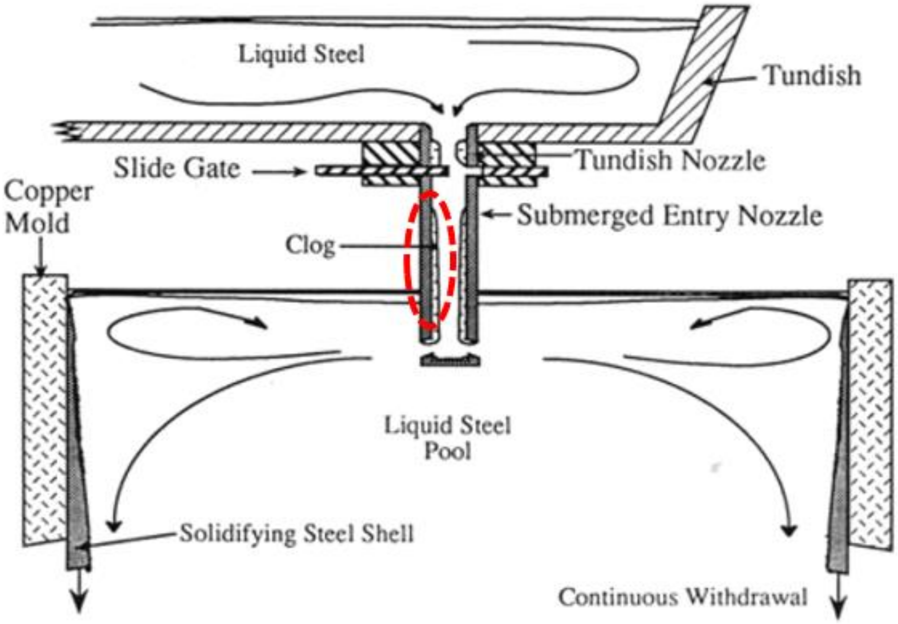

Figure 2-2 Transfer of steel after secondary steelmaking from tundish to the mold through ceramic nozzles [39]

Cramb et al. [40] and Kaushik et al. [14] discussed different kinds of solid inclusions reported in the clogged nozzles. Table 2-1 lists the inclusions found in a particular steel grade and the reason for the formation of inclusions. Alumina type inclusions are often encountered in aluminum killed steel. They are present as a result of deoxidation or reoxidation of steel. Inclusions of titanium nitrides are often reported during casting of stainless steel. Inclusions of magnesium aluminates types are formed by the reaction of magnesium in steel and alumina inclusions. They have been reported in both low carbon aluminum killed steel and stainless steel grades. Calcium aluminate types of inclusions are formed due to insufficient calcium treatment or reoxidation of steel. Aluminum titanate type inclusions are found in Ti stabilized ultra-low carbon steel and interstitial steel grades. Ti in the steel reacts with Al_2O_3 inclusions to form Al-Ti-O type inclusions. These inclusions are formed within the steel melt or at the SEN refractory-metal interface [41].

Table 2-1 Materials found in clog mass of nozzles used in steelmaking [14,40]

Inclusion	Steel grade	Reason
Al_2O_3	Al killed steel	Deoxidation of steel, reoxidation of steel by nozzle refractory or air
Ti- oxide	Al killed steel treated by Ti	Reoxidation of steel after Ti addition
Mg-Aluminates	Low carbon Al killed steel, 400 series stainless steel	Reaction between soluble Mg in steel and Al_2O_3 inclusions
TiN	400 series stainless steel	Precipitation product during casting
Ca-Aluminate	Ti stabilized ultra-low carbon steel, Ca treated Al killed steel	Insufficient Ca addition in Ca treated Al killed steel, reoxidation after Ca addition
Al- Titanate	Ti stabilized ultra-low carbon steel, Interstitial free steel	Reoxidation after Ti addition

Basu et al. [13] analyzed 40 SENs, their corresponding liquid steel and slag samples from titanium bearing and titanium free ultra-low carbon steels. A transverse section of the nozzle was prepared, and the clogged mass from the SEN was analyzed by SEM/EDX analysis. The chemical compositions of the steel and slag were analyzed. Figure 2-3 shows the image of clogged mass obtained from the SEN used for casting 700 tonnes of titanium alloyed ultra-low carbon steel grade [13]. The broken line is drawn to show the positions of the base and port of the nozzle which were removed to expose the clog. The deposit inside the SEN consists of coarse alumina and spinel inclusions as main constituents. Fine Ti bearing Al_2O_3-TiO_x type complex inclusions were also observed. A large volume of frozen steel skull was found.

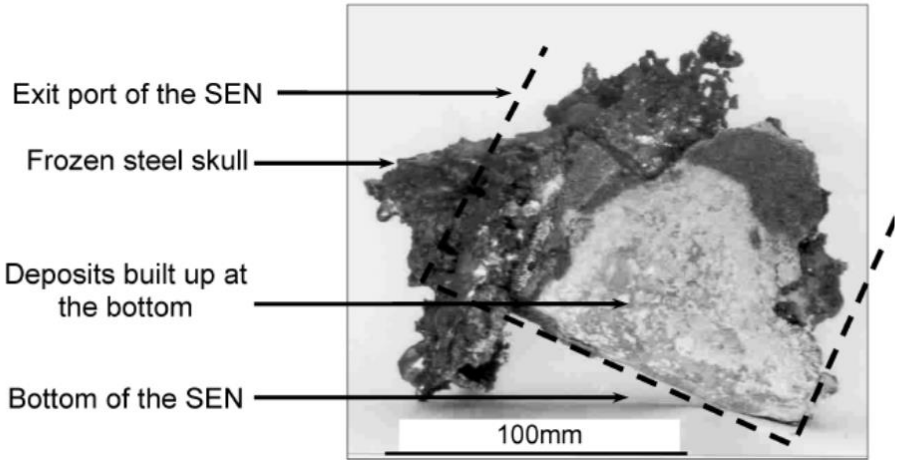

Figure 2-3 Shape of clog obtained from SEN used in the casting of Ti alloyed interstitial free steel [13]

Basu et al. [13] found that clogging can be reduced by controlling the initial attachment of alumina to the refractory surface. This control is achieved by lining the inner surface of the SEN with materials such as zirconia, boron nitride, or calcia-zirconia [13]. They identified that the Al-Ti-O inclusions are formed due to reoxidation and suggested a change in ladle slag and tundish slag could be led to lower clogging. They conditioned the ladle slag by adding 150 kg of Fe-Al chips to the slag. The slag conditioning helps bring down the FeO+MnO content of slag to less than 15%, which is considered less oxidizing to the dissolved Al and Ti in steel. A dual slag type practice is followed for the plant study by Basu et al.[13]. The layer on top of the molten steel is a basic slag type with 46-50 % CaO - 42-45 % Al_2O_3 - 3% SiO_2 - 2 % Fe_2O_3 and 1.8-2.5 % TiO_2 and the liquidus temperature of slag was 1380 °C. The second layer is that of a rice husk, which has more than 94 % SiO_2. Since the basic slag layer has a liquidus lower than the temperature of steel, it would melt, and the silica layer would dissolve in it. Once the silica layer dissolved in basic slag layer, it becomes oxidizing to the Al and Ti in the liquid steel. It was found that increasing the thickness of the basic slag layer led to reduction in clogging.

Similarly, Kaushik et al. [14] proposed a strategy to control the non-metallic inclusions, thereby reduce the nozzle clogging issue. They studied the recovery of Ti at the tundish by varying the circulation time between 3-6 minutes. They found that the following sequence of operations at RH degasser improved Ti yield: (1) Al addition (2) circulation for 5 minutes and (3) Addition of Ti. The increase in yield of Ti indicates a lower amount of Ti lost to inclusions. Another way of controlling inclusions is by changing the SEN design. Kaushik et al. [14] compared the clogging behavior of two nozzles with the varying configuration of outlet ports and lining. The first SEN was a straight nozzle with round outlet ports and without any lining.

The second SEN had two annular steps with square outlet ports and a non-sticking coating. It was found that the second nozzle showed few clog deposits and increased sequence length of casting. A disadvantage of the second nozzle is its more considerable wear in comparison to the first nozzle type. Although the use of such nozzles shows improvement in nozzle clogging, the phenomenon is not eliminated. There exist other theories to explain the source of clogging in the SEN [39,41–43]. Rackers and Thomas [39] calculated that in general, a clogged nozzle contains 16 % of the oxide inclusions that flow through the nozzle. They reported that the steel in the clog freezes due to heat loss through the nozzle wall. The freezing can happen either due to low preheat of the nozzle or wide freezing temperature range of the liquid steel. The first clog layer forms by accruing and sintering small oxide particles. The inclusion network and the solidified steel grow into the molten steel and propagate the clog [39].

Gao and Sorimachi [42] analyzed samples obtained from plant to investigate the inclusion types found in the SEN used for the casting of Ti stabilized stainless steel. SEM/EDX analysis, optical microscopy and EPMA of the clogged mass showed the presence of Al_2O_3, TiN and Ti oxides along with solid steel. The primary inclusion types were globular Ti oxide chains and Al_2O_3. They further conducted laboratory tests on steel samples similar in chemistry to the samples obtained from the tundish in the plant study. They remelted the steel and used different gas atmospheres to understand its effect on inclusions composition. It was found that when the atmosphere was Ar-O_2 with PO_2 of 0.25 atm, the inclusions were mostly Al_2O_3, Cr_2O_3, and FeO type. Ti oxides were not observed for this case. For an atmosphere of Ar-N_2 gas mixture with PN_2 of 0.25 atm, the inclusions were continuous granular TiN type. For a gas atmosphere of Ar-O_2 gas mixture with PO_2 of 0.07 atm, the inclusions formed are Ti oxide and TiN type. The laboratory tests showed that TiN could transform to Ti oxide only after reoxidation of steel, which contained some dissolved nitrogen. They concluded that in the SEN, the Al_2O_3 is formed by deoxidation while TiN forms by reaction of dissolved Ti in steel with adsorbed N. Some TiN precipitates at the nozzle surface. The portion of the nozzle at the base of the tundish has a porosity of 11-15 %. Air ingression through porous refractory reoxidizes the TiN to form TiO_2 type inclusions.

Lee et al. [41] proposed a stepwise mechanism to delineate the mechanism of growth of clog in SEN from titanium alloyed ultra-low carbon steel as follows: (1) The increasing temperature inside the SEN refractory leads to a carbothermic reduction of refractory oxides such as Al_2O_3 and SiO_2. (2) The CO formed by carbothermic reduction reacts with Al, Ti, and Fe in the liquid steel simultaneously to form liquid Fe_tO-Al_2O_3-TiO_x and solid Al_2O_3 at the steel-refractory interface. (3) The presence of the liquid Fe_tO-Al_2O_3-TiO_x alters the wettability of alumina by steel. (4) The Fe_tO-Al_2O_3-TiO_x is reduced by Al and Ti in the steel to form Al_2O_3-TiOx complex phase. This proposed mechanism by Lee et al. [41] explains why a small amount of Ti addition to steel affects the clogging by a significant amount. However, the primary cause of clogging is suspected as adhesion of non-metallic inclusions to the refractory walls and can happen by the attachment of inclusions to the walls of the nozzle [41].

2.4 Removal of inclusions

The ultimate goal of secondary steelmaking is to remove the inclusions, thereby minimize the number of inclusions in the final product. The removal process is achieved in three steps [44,45]. The first step is floatation of the inclusions [46]. Inclusions tend to float out of the liquid steel because their density is less than the density of steel. The stirring can be provided by bubbling argon through the bottom plugs of the reactor [47]. Since most inclusions are not wetted by steel, the inclusions separate from the steel and attach to the argon bubbles [47,48]. A stepwise process for attachment of inclusions to the bubbles is presented by Wang et al. [49].

1. The approach of a particle to a bubble
2. Formation of a thin liquid film between the particle and the bubble
3. Oscillation and/or sliding of the particle on the bubble surface
4. Drainage and rupture of the film with the formation of a dynamic three-phase contact
5. Stabilization of bubble/particle aggregates against external stress and
6. Floatation of the bubble/particle aggregates

The second step is the separation of the inclusion at the interface to the slag side [45,50–52]. The interfacial energy is the primary criterion for the separation of inclusion from the metal to the metal slag interface. For the process of separation of inclusion, the free energy can be written in terms of the interfacial energies, shown in equation 2-5 [53].

$$\Delta G = \gamma_{SI} - \gamma_{MS} - \gamma_{MI} < 0 \tag{2-5}$$

where ΔG is the free energy for the emergence of inclusion to metal slag interface, γ_{SI} is the slag inclusion interfacial energy, γ_{MS} is the metal slag interfacial energy and γ_{MI} is the metal inclusion interfacial energy. The interfacial energy for slag inclusion interface is low, which implies that liquid inclusions emerge to the slag metal interface with ease after which they can be quickly absorbed by the slag. It is important to note that the condition described in equation 2-5 can be thermodynamically favorable, but the kinetics may still be unfavorable for separation.

The third step is the dissolution of the inclusion in the slag [54–61]. The density of inclusions is usually higher than that of the slags. This creates the risk that even after separation into the slag phase, the inclusions can re-entrain back to the slag metal interface and prevent other inclusions from being removed [61]. Thus, it is vital that the inclusions dissolve quickly into the slag phase. The inclusion absorption ability is affected by the slag composition. Kaushik et al. [14] found that ladle slag with a ratio of CaO/Al_2O_3 of 1-1.25 is useful for alumina inclusion absorption and tundish flux has a better absorption capability compared to ladle slag for the titanium stabilized ultra-low carbon steel grades [14]. The comparison was based on thermodynamics and are mostly equilibrium calculations.

The kinetics of inclusion dissolution into slag can be studied by laboratory experiments using two techniques, namely the dip test and the high-temperature confocal scanning laser microscope.

2.4.1 Dip test

The life of refractory is an essential factor which critically affects the performance of high-temperature reactors. The dip test is widely used in the study of corrosion of refractories such as Al_2O_3 [62], and MgO [63], MgO-C [64] by slags. The dip test is further classified as the rotating dip test or the static dip test depending on the test conditions, i.e., whether the substrate rotates or not [62]. Figure 2-4 shows the experimental set up for static dip test [62]. The apparatus consists of an outer graphite crucible of 50 mm diameter and 120 mm length, which holds the slag. The substrate is dipped into the slag. The substrate is in the form of a cylinder, approximately 7 mm in diameter and 12.5 mm in height [62]. The substrate is wrapped in a platinum foil for the length above the slag to reduce any effect of slag-gas interface on dissolution. The substrate is brought in the vicinity of the slag and held there until the slag reaches the desired experimental temperature. The substrate is dipped into the slag for a predetermined time.

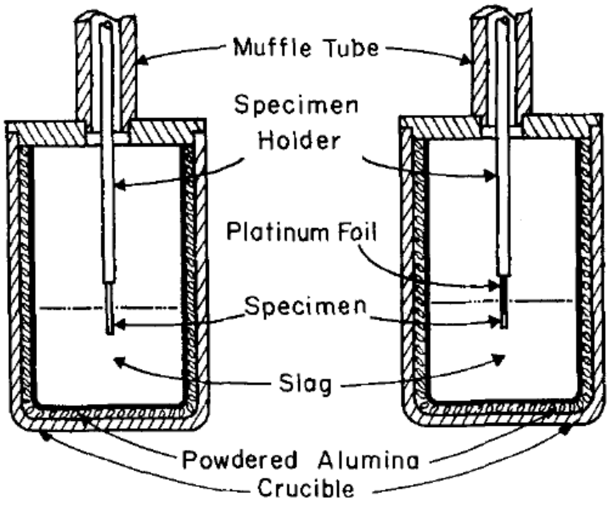

Figure 2-4 Experimental set-up for static dip test [62]

To examine the substrate, it is quenched by raising it to a location near the top of the muffle tube. The substrate is removed from the furnace, and the adhering slag is dissolved using concentrated hydrofluoric acid or hydrochloric acid. The change in the size of the substrate is measured along the axis. Using the size change data with time, the dissolution rate, and the mechanism of the species into the slag can be calculated [62]. The following sections summarize work related to the dissolution of different oxides such as Al_2O_3, MgO, Al_2TiO_5, and TiO_2 in various slag systems using dip test.

2.4.1.1 Dissolution of Al_2O_3

Cooper and Kingery [62] studied the dissolution of the alumina in an Al_2O_3-CaO-SiO_2 type melt at 1550 °C using rotating dip test. The rate of dissolution of a sapphire substrate is found to be proportional to the square root of the angular velocity of rotation. The dissolution rate increased with an increase in temperature. The dissolution rate for the case of a cylindrical sample is predicted under the assumption of mass transfer control. The measured dissolution rate for alumina in slag is compared with the theoretical curve. It is found that the predicted curve is in close agreement with the measured data. This confirmed that the dissolution of sapphire is mass transport control in slag.

Samaddar et al. [65] studied the dissolution of single crystal and polycrystal alumina in 20 Al_2O_3-40 CaO-40 SiO_2 (in wt %) slag at a temperature range between 1350-1500 °C. They found that the rate of dissolution of single crystal and polycrystal alumina were similar. For the experiment at 1500 °C, the dissolution rate of polycrystal alumina is higher in the beginning because of greater surface roughness. However, the rate of dissolution of single crystal and polycrystal alumina are similar after the first 20 minutes. The rate of dissolution is controlled by dissolution in a boundary layer.

Taira et al. [66] studied the dissolution behavior of sintered alumina substrate in Al_2O_3-CaO-SiO_2 type slag at a temperature range between 1500 - 1580 °C. The rate of dissolution of alumina was found to be directly proportional to the speed of rotation and the temperature. The rate of dissolution increased with an increase in CaO/SiO_2 ratio of slag due to a decrease in slag viscosity with an increase in CaO/SiO_2. The rate of dissolution of alumina is controlled by diffusion of solute in the slag boundary layer.

Yu et al. [67] studied the dissolution of the alumina in an Al_2O_3-CaO-SiO_2-Na_2O-CaF_2 type mold flux at 1530 °C using the rotating dip test. It was found that the rate of dissolution of alumina was proportional to the slag viscosity.

Sandhage and Yurek [68] studied the dissolution of a sapphire substrate in an Al_2O_3-CaO-MgO-SiO_2 type slag. A spinel layer was observed at the interface of the sapphire and slag. They suggested that the amount of MgO in slag controlled the morphology of the spinel at the interface. The morphology of spinel dictated the rate of dissolution of the sapphire substrate. For slag with 5 % MgO isolated spinel droplets were detected, and the overall rate was high. For slag with 15, 20, and 25 % MgO continuous spinel layer were present at the interface, and the total dissolution rate was low. For slag with 10 % MgO the spinel was present as an incomplete layer at the interface, and the total dissolution rate was in between that for the case of 5 % MgO and 15-25 % MgO.

2.4.1.2 Dissolution of MgO

Monaghan et al. [69] studied the dissolution of MgO in Al_2O_3-CaO-SiO_2 type slag using the rotating dip test. In this study, two slag compositions were used, the first slag without

Al_2O_3, and the second slag containing 20 % Al_2O_3. The profile of substrate depended on the time of dipping and speed of rotation. For high rotation speed with short dip time the corrosion stayed at refractory-air-slag interface retaining the cylindrical shape while for high rotation speed and long dip time, the dipped portion of substrate corroded turning it into a cone shape. For slag without alumina, the dissolution was found to be mass transfer control at speed below 600 rpm while it was chemical reaction control above 600 rpm. For slag with alumina, a spinel layer was detected at the interface. However, the overall rate of corrosion of the MgO substrate was not affected by the spinel layer.

2.4.1.3 Dissolution of Al_2TiO_5

The dissolution of Al_2TiO_5 into a 15% Al_2O_3-35% CaO-50% SiO_2 slag was studied at 1550 °C using the static dip test by Wang et al. [1]. They reported the dissolution behavior of substrate by dipping it into the slag for 0, 10, 30 and 60 s. The substrates were quenched in argon to room temperature. To reveal the dissolution path or mechanism, the section of the substrate was prepared to study the substrate-slag interface by SEM-EDX. It was observed that the substrate dissolution and slag penetration occurred simultaneously. The rate of dissolution of Al_2TiO_5 substrate to bulk slag was faster than the rate of diffusion of the slag at the interface for the first 30 seconds, but the two rates became equal from 30 to 60 seconds.

2.4.1.4 Dissolution of TiO_2

Ren et al. [2] studied the dissolution mechanism of TiO_2 in three slag compositions with basicity of 0.8-1.2 at temperatures of 1370 °C, 1400 °C, and 1430 °C. From the study, they found that the dissolution of TiO_2 proceeds in three distinct steps: (1) dissolution of Ti^{4+}

ions into the bulk slag, (2) accumulation of Ti $^{4+}$ ions in a boundary layer adjacent to the TiO_2 substrate and (3) the precipitation of $CaTiO_3$ at the boundary layer due to high local concentration of TiO_2. The formation of $CaTiO_3$ in the third step slowed down the diffusion of Ti^{4+} ion to the bulk slag. Thus, the diffusion of Ti $^{4+}$ ions from the boundary layer to bulk slag was assessed as the rate-controlling step.

Results based on post-analysis of the sample obtained from dip tests reported above make it impossible to observe dynamic changes in sample shape. Although the dip test has provided insight into the dissolution of bulk oxides, it is questionable whether the data generated from the cm-sized refractory can be applied to kinetics and mechanism at micron-sizes. The confocal scanning laser microscope allows for continuous “in situ” observation of micron-size samples in real-time, at high resolution, under conditions relevant to the steelmaking process.

2.4.2 Confocal Scanning Laser Microscopy (CSLM)

The CSLM is a useful tool to study the dissolution kinetics of inclusions such as Al_2O_3 [54–56,58–61,69,70], MgO [71–73], $MgAl_2O_4$ [74,75] and SiO_2 [76] in the ladle or tundish type slags. There are also some studies related to the dissolution of SiC [77], CaO [78], ZrO_2 [74,75] type particles using CSLM, which are not covered in detail since these inclusions are out of the scope of the objective of current work. The following sections summarize the working principle of the CSLM, previous studies related to the dissolution of MgO, Al_2O_3, $MgAl_2O_4$, and SiO_2 in various slag systems ($CaO-Al_2O_3-SiO_2$ (CAS)/$CaO-Al_2O_3-MgO$ (CAM)/ $CaO-Al_2O_3-SiO_2$ –MgO (CASM)) using CSLM and discussion of the kinetics of inclusion dissolution.

2.4.2.1 Working Principle of the CSLM

A lot of stray light is collected while a spot on the specimen is being analyzed in conventional fluorescence microscopy. The drive behind the invention of the CSLM was to eliminate the stray light, thereby increasing the resolution of the microscope. Marvin Minsky, then a junior research fellow at Harvard University in 1956 [79] proposed that the stray light can be cut off by placing a pin-hole aperture in front of the eyepiece. He named the initial model a double-focusing stage scanning microscope. The term “stage scanning” means that the specimen stage moved during observation while the optical system remained stationary; double-focusing implies that the point of observation from the specimen is in the same focal plane as that of the image. The first apparatus consists of a light source which passes through a pinhole aperture to produce a pencil of light. The light passes through an objective lens which focuses the light on to a spot on the specimen. The focused light passes through the point on the sample and passes through another lens to magnify the image. The magnified information is sent to a photosensitive device where the data is processed in a signal and displayed on an oscilloscope. The first microscope had an optical illumination system which is sensitive to movement, because of which the microscope started as a moving stage in contrast to the moving source currently in application.

The high-temperature confocal scanning laser microscope consists of two major sections, infrared gold imaging furnace, which is gold coated form inside and a laser-based confocal optic system which scans the samples. The laser microscope collects data and sends it to the computer through cables attached to the back of the laser head collects data and sends it to the computer. A block diagram delineating the different components of a high-temperature laser scanning confocal microscope is shown in Figure 2-5.

A sharp laser beam of approximately 0.5 µm [69] is focused through an objective on the sample by the user. The pinhole aperture is situated at the back focal plane of the objective, close to the laser source where the focused light is collected. The light reflected from the sample is deflected through a bandpass filter which allows only the laser to pass through it and stops light of other wavelengths. The collected signals are processed and sent to the computer to produce a live image on the screen. Excellent instrumentation allows the sample to be moved in X, Y, and Z directions during observation at high temperatures. The IR gold image furnace is in the shape of a paraboloid with a 1.5 kW halogen lamp (shown in yellow in Figure 2-5 placed at one focus and the sample holder located at the other focus. The halogen lamp is cased in a quartz tube which is cooled by air pumped by an external air compressor. The cooling air from the quartz tube leaves the furnace chamber through an exit sleeve placed under the thermocouple and sealed by an alumina tube. The sample is placed on the sample holder using a platinum crucible for slag samples and alumina crucible for metal samples. There is a B type thermocouple sheathed in an alumina tube and placed attached to the sample holder to measure the furnace temperature. The temperature is fed back to the temperature controller, which controls the heating and cooling with the help of a PID control. The furnace lining is a steel block which is cooled by continuous running water supplied from a chiller installed alongside the furnace. The atmosphere inside the furnace is controlled by passing high purity argon through the system. The gas is cleaned by a gas purification system present alongside the furnace.

The CSLM used for the current work is the VL2000DX-SVF17SP design. The VL2000DX is the digital laser camera head using a 408 nm ultraviolet laser beam to scan and image, SVF17SP is the ultra-high temperature image heating furnace. The unit is equipped with the MC1000A temperature controller. All the features of the microscope put together can achieve a magnification up to 3000X in the temperature range of 25-1800 °C.

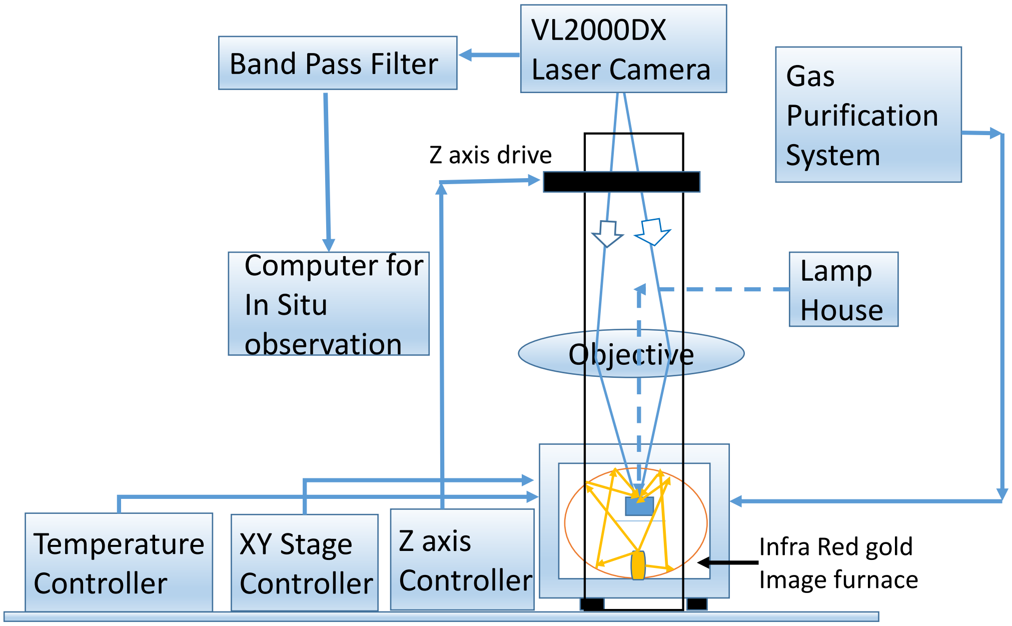

Figure 2-5 Block diagram showing essential parts of the high-temperature confocal scanning laser microscope

2.4.2.1 Dissolution of Al_2O_3

The dissolution of Al_2O_3 inclusion type is the most widely studied case with CSLM. Table 8-1 in Appendix summarizes the range of experimental conditions affecting the dissolution kinetics and mechanism of Al_2O_3 inclusions studied by previous researchers. The literature [54,56–59,61,69,70,73,80] covers a wide range of experimental parameters; particle diameters ranging from 90-500µm, several slag compositions and temperatures ranging from 1200 °C-1630 °C. It should be noted that the viscosity values are calculated using Urbain's model [81].

The pioneering work for studying alumina dissolution in slag is by Sridhar and Cramb [61]. They investigated the effect of the temperature on the dissolution of 100-180 µm alumina particles in a CASM slag. It was found that the total dissolution time of Al_2O_3 particle decreased from 2112 seconds to 203 seconds by increasing temperature from 1430 to 1550 °C. Subsequently, similar tendency on the effects of the temperature and the slag composition have been reported by Sridhar and co-workers [54,58,70], Michelic et al.[57], Monaghan et al. [56,69,80], and Liu et al.[59], regardless of the inclusion size. As a summary of the previous studies [5, 16, 18-23], the dissolution time of Al_2O_3 in the CAS-contained slag decreased with a decrease in the slag viscosity. Specifically, Lee et al.[54] and Valdez et al.[58] reported the MgO addition in the CAS slag could retard the dissolution of Al_2O_3, and the experimental evidence of the $MgAl_2O_4$ formation has been found [72]. In another study, it is observed that the addition of FeO_x to the CAS slag could increase the dissolution rate of Al_2O_3 [70].

2.4.2.2 Dissolution of MgO

The dissolution behavior of MgO in slag has been studied by a few researchers [71–73]. Yi et al. [73] investigated the effects of temperature and the slag composition on the dissolution of MgO. The detail information with MgO dissolution studies in CSLM is shown in Table 8-2. They reported that an increasing temperature from 1450 °C to 1500 °C resulted in a decrease in the dissolution time of MgO in CAM slag and this tendency could be observed in the CAM slag with varying viscosities. Furthermore, they claimed that about 5 wt. % MgO addition into the CAM slag can delay the dissolution time of MgO significantly. The dissolution time of MgO with a diameter of 200 to 400 μm was about 570 s in a CAM slag with 0.52 wt. % MgO, and this time extended to about 3000 s in a CAM slag with 5.57 wt. % MgO. Liu et al. [71] discussed the effects of temperature and MgO addition amount in CAS slag on the MgO dissolution. A similar conclusion was made on the impact of temperature. For the case of a 350~400 μm MgO dissolution in the slag without MgO (<0.5 wt.%), it is reported that the increasing temperature reduces the dissolution time, which was from about 6000 s at 1500 °C to about 3400 s at 1600 °C.

2.4.2.3 Dissolution of $MgAl_2O_4$

Monaghan et al. [80,82] studied the dissolution of magnesium spinel in CAS slag in the temperature range of 1477-1577 °C while Fox et al. [74] studied the dissolution of $MgAl_2O_4$ in a fluoride-free mold slag. For the latter, 600-800 μm diameter particles were dissolved in a 20% CaO-<10%Al_2O_3 -40% SiO_2 -<10%MgO - 20% Na_2O-1%Li_2O-1.5%B_2O_3 slag. The temperatures used for the study are 1300, 1400, and 1500 °C. The data for $MgAl_2O_4$ dissolution in the literature using CSLM is presented in Table 8-3.

Monaghan et al. investigated both the effects of temperature [80] and the slag viscosity [82]. For the former case, the slag composition was fixed with a 16.3 CaO-19.3 Al_2O_3-64.5 SiO_2 (wt. %). The dissolution time decreased from over 500 s to around 100 s with the increasing temperature from 1477 to 1504 °C. After that, the dissolution time slightly reduced from 1504 to 1532 °C. They [82] found that the dissolution time of $MgAl_2O_4$ spinel particle decreased with the decreasing viscosity of slag, which was 80 s for the case of a high viscosity slag and 30 s for the example of a low viscosity slag.

2.4.2.4 Dissolution of SiO_2

Feichtinger et al. [76] studied the dissolution of amorphous SiO_2 particle in an Al_2O_3-CaO-SiO_2 type slag at 1450 °C. The SiO_2 particle used were spherical in shape of 350 µm diameter to avoid any rotation of the particle. They found that the slag with higher viscosity had a slower dissolution rate. The viscosity of the slag changes from 32 to 160 poise, according to the difference in the composition of the slag. A comparison of dissolution data for different slag composition is presented in Table 8-4.

2.4.3 Effect of viscosity on the inclusion dissolution in the slag

From the CSLM literature [54,56–61,69,70,80], it can be inferred that there are two critical factors that affect the dissolution kinetics of inclusions, (a) the temperature and (b) the slag composition. Both the temperature and slag composition affect slag viscosity by a large extent, which in return can affect the dissolution kinetics [76]. Figure 2-6 compares the dissolution rates of alumina as a function of viscosity at 1500 °C using the data from literature [69,73]. The data is reproduced in the form of normalized size versus time and extracted using an open-source software Plot Digitizer^{TM}. Monaghan et al. [69] reported the dissolution rate of irregular alumina particles in a 19.3 Al_2O_3 – 16.3 CaO – 64.4 SiO_2 slag at 1500 °C. The initial equivalent circular radius is 50 micron and total dissolution time is 1700 s. Yi et al. [73] reported the dissolution rate of irregular alumina particles in a 48.9 Al_2O_3 – 48.4 CaO – 0.52 MgO slag at 1500 °C. The initial equivalent circular radius is 96 micron and total dissolution time is 174 s. It is found that the dissolution time of alumina decreases with lowering the slag viscosity.

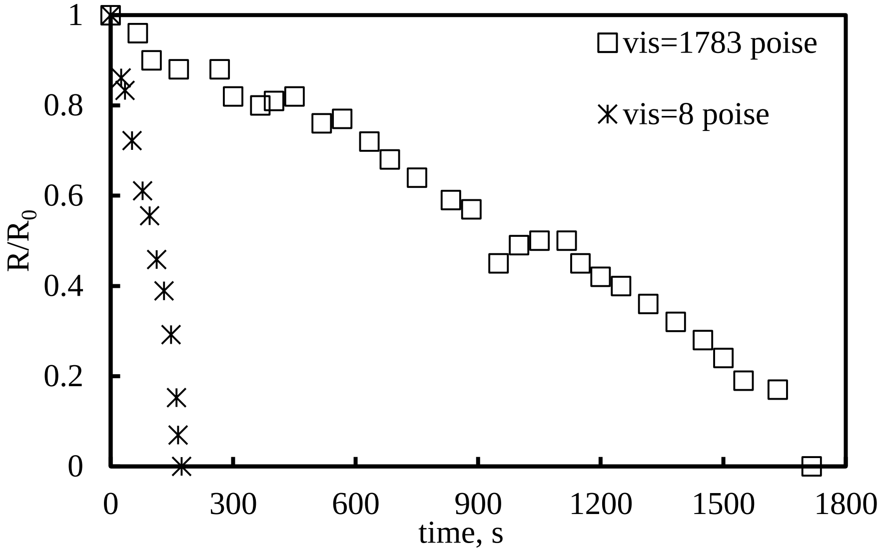

Figure 2-6 Effect of slag viscosity on the rate of dissolution of Al_2O_3 particle at 1500 °C [69,73]

It is established that the dissolution mechanism of alumina in slag is boundary layer mass transfer control [54–56,58–61,73]. Thus, the effect of slag viscosity on dissolution rate can be related to the slag structure. Equation 2-6 shows the Stoke-Einstein relationship, where the diffusivity of transported species is inversely proportional to the slag viscosity. The higher the silica content of the slag, the higher the slag viscosity. A decrease in slag viscosity leads to increase in diffusivity. The diffusivity of alumina reported by Monaghan et al. [56] is 1.9 x 10^{-11} m^2/s.

$$\mathrm{D} = \frac{\mathrm{K_b T}}{\eta\lambda} \tag{2-6}$$

where K_b is the Boltzman constant, T is temperature, η is slag viscosity, and λ is jump distance.

Similar observations were observed for the dissolution rate of MgO particles. However, the dissolution was complicated by the formation of $MgAl_2O_4$ whenever a MgO particle was in contact with CAS/CASM slag. The normalized radius versus time data for MgO dissolution at 1500 °C is plotted using CSLM literature in Figure 2-7 [71,73].

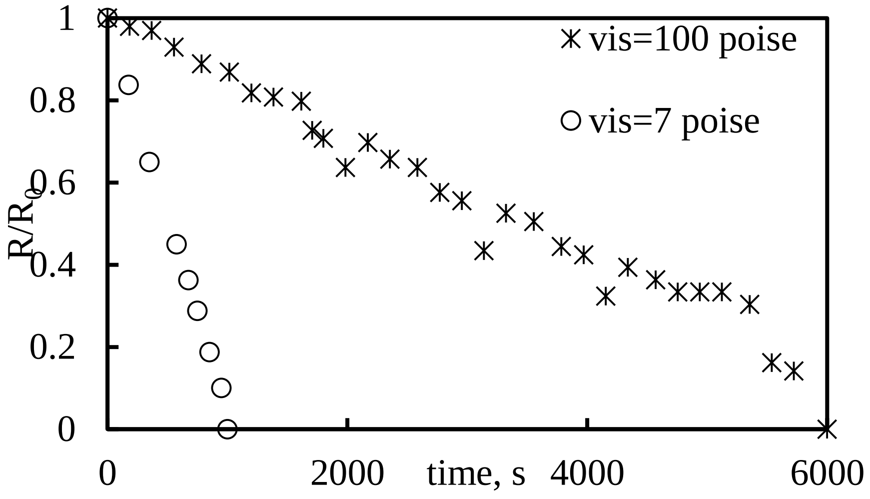

Figure 2-7 MgO dissolution reported in the literature at 1500 °C [71,73]

Yi et al. [73] reported the dissolution of MgO in a 46.7 Al_2O_3-46.3CaO-5.6MgO slag at 1500 °C. The viscosity of slag is 7 poise, the initial particle diameter is 160 micron, and total dissolution time is 1000 s [73]. Liu et al. [71] reported the dissolution rate of MgO particle in a 24.1 Al_2O_3 - 29.7 CaO – 46.7 SiO_2 slag at 1500 °C. The viscosity of slag is 100 poise, the initial particle radius is 354 micron, and the total dissolution time is 6000s. The relatively high viscosity of the slag slows down the MgO dissolution. This is reflected in the dissolution rate, which is faster in case of slag with a viscosity of 7 poise in comparison to the slag with a viscosity of 100 poise.

2.4.4 Modeling of inclusion dissolution kinetics

The measurement of dissolution is predominantly studied using the rotating cylinder test or rotating disc test [83]. The rotating disc method enables calculation of boundary layer thickness. However, this method is limited to substances which maintain their structural integrity upon melt infiltration. The rotating cylinder test can be used for almost any material. The limitation with the rotating cylinder test is that the flow field around a rotating cylinder is complex and can be only empirically modeled [83]. The introduction of in situ measurement tools provides dynamic changes in particle size with time data. Conversely, such a data can be used to establish the rate-controlling mechanism by comparing the theoretically estimated curves using the shrinking core model (SCM) with the measured values [55,58–61,73].

Based on SCM, Levenspiel [84] suggested a sequence of steps to determine the shrinkage in size of a particle with time in the absence of a reaction product layer. In terms of the dissolution of a single inclusion particle in slag, the steps are stated as follows [84]:

Step 1. Chemical reaction of the inclusion particle with the slag at the surface of the unreacted core.

Step 2. Diffusion of species through the boundary layer to the bulk slag.

Therefore, the overall dissolution of the particle faces two resistances; chemical reaction at the particle slag interface and diffusion through the boundary layer.

2.4.4.1 Chemical reaction control

The dissolving particle might react with the slag to form a reaction product. If the rate of such reaction is slower in comparison to any other mass transport step, then the rate-controlling mechanism is chemical reaction control. The dissolution happens because the concentration of solute is higher in the particle in comparison to the slag. Since the chemical reaction is the rate-controlling step, there is no concentration gradient of solute in the particle or the slag. The concentration profile of the solute in case of a chemical reaction control is shown in Figure 2-8. The size of the particle decreases as time progresses. The rate of dissolution is proportional to the available surface area of the unreacted core. The size of the unreacted particle core at any time is r_c. The thickness of the slag boundary layer is δ. The chemical reaction control shows a linear relationship of the radius with the time displayed by equation 2-7 [84].

$$\frac{r_c}{R_0} - 1 = \frac{b K_R \Delta C}{\rho_{particle} R_0} t \tag{2-7}$$

where t is instantaneous time, $\rho_{particle}$ is the density of particle under consideration, R_0 is the initial radius, b is the stoichiometric constant and equal to 1. ΔC is the difference in concentration of the rate-limiting species in bulk slag and slag saturated with that species, and K_R is the first-order rate constant for the surface reaction.

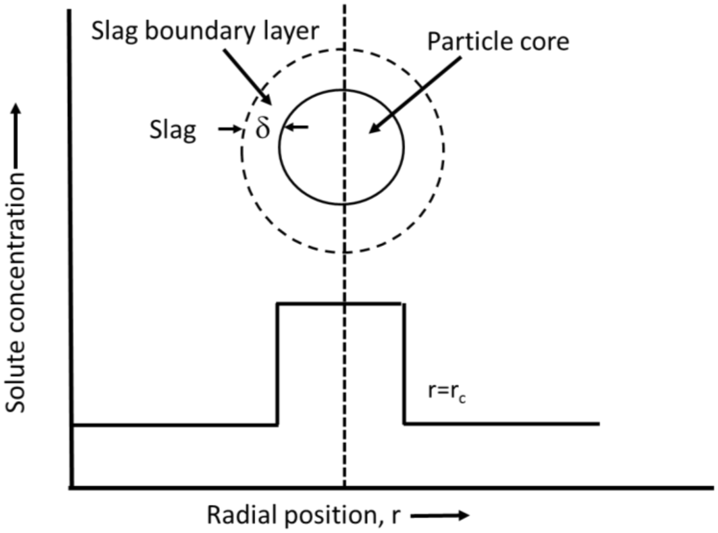

Figure 2-8 Schematic representation of particle when the chemical reaction is rate-controlling

2.4.4.2 Boundary layer diffusion control

This model assumes that the transport of species from the particle to the bulk of slag takes place by diffusion through the slag boundary layer. If the dissolution is boundary layer diffusion-controlled, the dissolution is affected by slag property, the relative velocity between the particle and slag and size of the particle [84].

Figure 2-9 shows the concentration gradient of the dissolving species when diffusion at the boundary layer is rate controlling. This model shows a parabolic relationship of the radius with time, as shown by equation 2-8 [84].

$$\left(\frac{r_c}{R_0}\right)^2 - 1 = \frac{2b\Delta CD}{\rho_{particle} R_0^2} t \tag{2-8}$$

where D is the diffusivity of the species in consideration. It is important to note that the Equation 2-8 is applicable for small particle and fluid flow within the Stokes's regime.

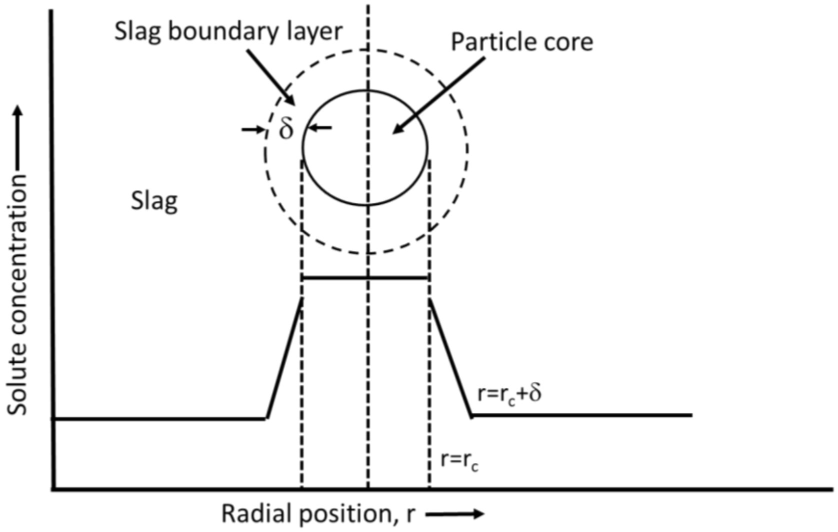

Figure 2-9 Schematic representation of particle when diffusion in the boundary layer is rate-controlling

A comparison of the dissolution curve for the assumption of chemical reaction control and boundary layer diffusion control is shown in Figure 2-10.

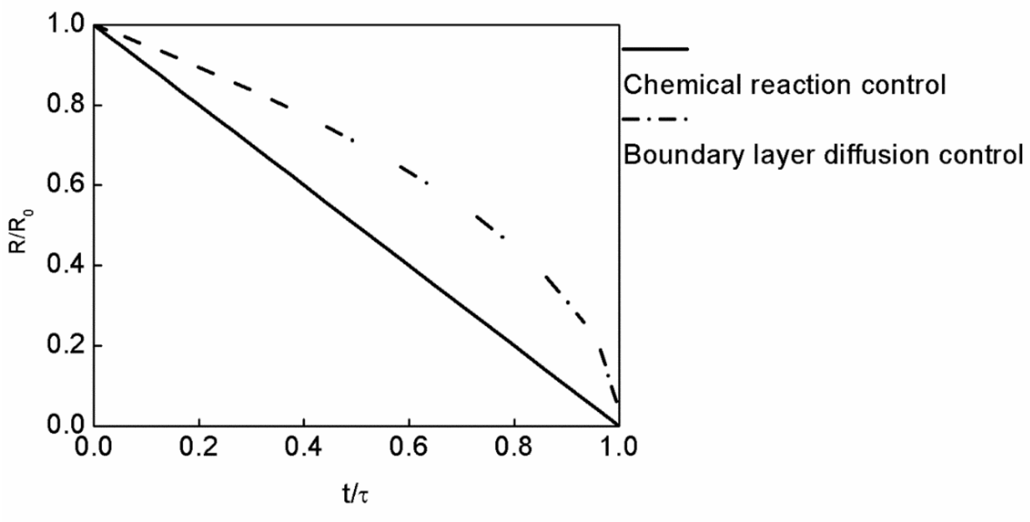

Figure 2-10 Comparison of dissolution curves based on chemical reaction control and boundary layer diffusion control moels

Numerous researchers [54,56–61,69–73,76,80,82] applied the classical shrinking core model (SCM) to investigate the mechanism for inclusion dissolution in slag. For instance, Sridhar and Cramb [61] claimed that the boundary layer diffusion is the rate-controlling mechanism since the experimental data could almost fit the predicting model results. In most of these studies [57–59,71,73,76,85], the CSLM data do not agree entirely with either of the chemical reaction control or boundary layer diffusion control curves shown in Figure 2-10.

Liu et al. [71] observed that the MgO dissolution data in CAS slag lie in between the chemical reaction control curve and boundary layer diffusion control curve however they claimed that the dissolution behavior is primarily controlled by a boundary layer diffusion mechanism. For the case of CASM slag with an addition of 7.3 wt. % MgO, the dissolution rate of MgO is retarded at both 1500 and 1600 °C. The radius of MgO just reduced about 15% with a dissolution time of about 4000 s at 1600 °C and about 5700 s at 1500 °C. The reason related to this phenomenon was due to the formation of magnesia-alumina spinel ($MgAl_2O_4$), which had been predicted by both SEM, EPMA-EDS, and thermodynamic calculation by Liu et al. [71]. A similar phenomenon has also been reported by Park et al. [72], who investigated $MgAl_2O_4$ and Ca_2SiO_4 formation around MgO inclusion during its dissolution in CAS slag. However, Yi et al. [73] found that the dissolution of MgO in the studied slag is controlled by the rate of the chemical reaction.

Yi et al. [73], Michelic et al. [57], Liu et al. [59], Verhaeghe et al. [86], and Valdez et al. [58] observed that dissolution data for alumina lies in between the chemical reaction and boundary layer diffusion control curve. Monaghan et al. [82] reported that the mechanism of the $MgAl_2O_4$ spinel particle dissolution in the CAS slag is at least in part controlled by boundary layer diffusion, since the value of calculated diffusion coefficient using CSLM data is found to be inversely proportional to the slag viscosity, see the detailed value in Table 8-3. Moreover, it is found that the value of the diffusion coefficient increased as the slag viscosity decreases [82], see Table 8-4.

Feichtinger et al. [76] observed similar discrepancy for dissolution of SiO_2 in slag and explained it by proposing a dissolution mechanism to be diffusion in a stagnant fluid. The mechanism is described by a transient one-dimensional diffusion equation for spherical coordinates [59,73] as shown in Equation 2-9.

$$\frac{\partial \mathrm{C}}{\partial \mathrm{t}} = \mathrm{D}\frac{1}{\mathrm{r}^2}\frac{\partial}{\partial \mathrm{r}}\left(\mathrm{r}^2\frac{\partial \mathrm{C}}{\partial \mathrm{r}}\right) \tag{2-9}$$

where r is the radius of particle and C is the concentration of the rate-determining species at distance r. The solution of equation 2.9 can be approximated in spherical coordinates. The first case is called the invariant interface or stationary interface approximation. In this case, the movement of the interface is considered to not affect the diffusion field. In this case, there is a concentration gradient in the bulk slag. This concentration gradient of the diffusing species in the bulk slag is time-dependent, and the concentration profile changes with time. The second case is called invariant field approximation, where a concentration gradient exists only in the boundary layer and not in the bulk slag. The concentration profile of species in the boundary layer does not change with time. The invariant field approximation yields a solution similar to that shown by diffusion in boundary layer control for the SCM. Michelic et al. [57] further claimed that two cases are due to the effect of slag viscosity. In the CAS slag with a high viscosity, the mechanism is the mass transfer through the bulk slag, named diffusion control in their report [57]. For the slag with low viscosity, it is controlled by the boundary layer diffusion control. Another approach to solving equation 2.9 is using finite difference method proposed by Liu et al. [73]. Verhaeghe et al. [87] used the Lattice Boltzman model to simulate the dissolution of the alumina in a CaO-SiO_2-Al_2O_3 type slag. The solution using a Lattice Boltzman method provides a perfect fit to the experimental data but is relatively complex.

Yan et al. [88] also suggested an approach to explain the discrepancy between the CSLM data and curves from SCM. In the models represented by equation 2-7 and 2-8 ignore the effect of rotation on the dissolution kinetics. For example, the alumina particle is seen to rotate during dissolution, and this phenomenon is confirmed by many researchers [54–56,58,61]. The rotation of the particle during dissolution affects the shape of the curve, which creates the scatter in CSLM data. Yan et al. [88] proposed a new method to predict the relationship between the mass transfer coefficient and the diffusion coefficient, as shown in equation 2-10 and 2-11. The value of the mass transfer coefficient is affected by the particle size and fluid velocity, which concerns the particle rotation during its dissolution in liquid slag.

$$\mathrm{K_s} = \frac{\mathrm{D}\left(4.0+1.21\mathrm{Pe}^{2/3}\right)^{1/2}}{2\mathrm{R}} \quad \textit{for Pe < 10,000} \tag{2-10}$$

$$\mathrm{K_s} = \frac{1.1\mathrm{DP_e}^{1/3}}{2\mathrm{R}} \quad \textit{for Pe > 10,000} \tag{2-11}$$

where K_s is the mass transfer coefficient, Pe is the Peclet number, and R is the particle radius. Pe=2RU/D. U is the fluid flow velocity around the particle. The particle velocity is estimated using the size of the particle and assuming one rotation takes 30 seconds. In equation 2-7, the mass transfer coefficient was defined by D/R in comparison to equation 2-10 and 2-11. On applying the corrections to the mass transfer coefficient, Yan et al. [88] found that the CSLM data shows a better fit to the boundary layer mass transfer curve, except for the data reported by Liu et al. [89]. However, it is essential to note that no particle rotation was observed in this experimental work.

To summarize, current inclusion removal studies using confocal scanning laser microscope (CSLM) are mostly focussed on the dissolution behavior of simple oxide particles such as Al_2O_3 and MgO in steelmaking slags. However complex inclusions such as Al-Ti-O and calcium aluminate inclusions can form and cause submerged entry nozzles (SEN) clogging during continuous casting. As the frequency of nozzle clogging negatively affects productivity, understanding the behavior of these inclusions is critical in optimizing productivity. Further, most of the literature agrees that inclusion dissolution in slag is governed by boundary layer diffusion control [55,58,61,73,88]. The shrinking core model is widely used to delineate the dissolution kinetics of inclusions in slag. However, these assumptions are usually not supported by experimental evidence such as concentration profile in bulk slag. This literature review highlights the lack of dissolution data for Ti-containing inclusions and areas of uncertainty in the rate-controlling mechanism of inclusion dissolution in slag.

Chapter 3

Application of optical floating zone method to dissolution kinetics of inclusions in a steelmaking slag

Chapter 3 is a pre-publication version of the article published in Steel Research International 2018, Volume 90, Issue 1, DOI:10.1002/srin.201800367. The following chapter details the application of the optical floating zone method (OFZM) in preparing non-metallic oxides. The microparticles used for CSLM studies are often purchased from the marketplace because of high purity and density requirements. However, complex inclusion types such as Al_2TiO_5 are not available from marketplace suppliers. These oxides closely represent the problematic inclusion types encountered in the secondary steelmaking process. To experimentally study the removability of various complex inclusions, optical floating zone method (OFZM) and sintering method are presented here to produce high purity micro-particles. The syntheses of TiO_2 and Al_2TiO_5 inclusions were employed to demonstrate the advantages and potential application of both techniques for dissolution experiments. These inclusions were then dissolved in the steelmaking slags using CSLM at 1430 °C. In situ observation showed that there is gas evolution during the reaction between slag and Al_2TiO_5 particles prepared by both techniques. However, the gas evolution is more rapid during the dissolution of particles prepared by sintering and hinders in situ observations and measurements. Thus it was concluded that the OFZM provided a better path to produce microparticles suitable for use in dissolution experiments using CSLM. All data collection and analysis, as well as manuscript drafting, was completed by the primary author. Dr. Dogan contributed to the discussions and proofread the manuscript. Dr. Hanna Dabkowska provided training for using the optical floating zone technique and reviewed the final version of the manuscript.

Application of optical floating zone method to dissolution kinetics of inclusions in a steelmaking slag

Mukesh Sharma*, Hanna A. Dabkowska, Neslihan Dogan

Mukesh Sharma, Ph.D. Student, sharmmk2@mcmaster.ca
Materials Science and Engineering Department, McMaster University, L8S4L7, Canada

Dr. Hanna A. Dabkowska, Research Scientist,
Brockhouse Institute of Materials Research, McMaster University, Canada, L8S4L7

Dr. Neslihan Dogan, Assistant Professor,
Materials Science and Engineering Department, McMaster University, L8S4L7, Canada

Abstract

The dissolution kinetics of micro-particles (inclusions) in steelmaking slags has been investigated using the high-temperature confocal scanning laser microscope (HT - CSLM). However, these studies focused on the limited type of inclusions such as Al_2O_3, SiO_2, MgO, CaO and $MgAl_2O_4$. To experimentally study the removability of various problematic inclusions that are not available in the market, optical floating zone and sintering techniques are presented here for the production of high purity micro-particles. The syntheses of TiO_2 and Al_2TiO_5 inclusions were employed to demonstrate the advantages and potential of both techniques. These inclusions were then dissolved in the steelmaking slags using CSLM at 1430 °C. In situ observation showed that there is gas evolution during the reaction between slag and Al_2TiO_5 particles prepared by both techniques. However, the gas evolution is more rapid during the dissolution of particles prepared by sintering and hinders in situ observations and measurements. The optical floating zone is capable of

preparation of microparticles with high purity and less porosity. At 1430°C, the Al_2TiO_5 particles didn't dissolve at all, whereas TiO_2 particles completely dissolved in 200 seconds.

3.1 Introduction

Titanium (Ti)-containing inclusions are of special interest to interstitial free (IF), high strength and stainless-steel producers [1–4]. These inclusions are harmful to steel properties and are produced by deoxidation and reoxidation in steelmaking processes [1,5]. Ti tends to increase the wetting of Ti-containing alumina inclusions by liquid steel, which causes difficulties in their removal [6–8]. The presence of such inclusions in molten steel causes clogging of ceramic nozzles during casting, and, if they are dislodged from the nozzle in the liquid steel, they reduce steel quality by appearing as defects on the cast product [1,9,10].

Industrial research on Ti containing inclusions has focused on their formation, modification and distribution in steel refining units [1–3,7,11–13]. Kaushik et al. [2] studied clogging incidents related to industrial operations and found that alumina and aluminum titanates are present in most of the clog mass or the steel collected at the tundish or mold samples analyzed during casting of titanium stabilized ultra-low carbon (Ti-SULC) steel. An increase in Al content in liquid steel and use of better Fe-Ti alloys, as well as using anti clogging nozzles improved the castability of these steel grades[2]. Kaushik et al. [2] reported that practices such as circulation rinse before Ti addition in Ruhrstahl Heraeus (RH) and use of anti-clogging nozzles helped to improve the Ti yield and steel castability. Basu et al. [1] analyzed 40 submerged entry nozzles (SEN) used during the casting of IF steel with and without Ti alloying. They found that reoxidation was the source of Al-Ti-O type inclusions present in the clog mass. They observed extensive melt freezing during the casting of Ti alloyed IF steel. Nunnington and Sutcliffe [14] reported that while Al_2O_3, TiN and Ti_3O_5 type inclusions are major inclusion types, minor inclusions such as Al_2TiO_5 and $MgAl_2O_4$ are encountered during stainless steel production. Given the industrial importance of Ti containing inclusion removal in steelmaking, this area requires fundamental study to fill key knowledge gaps.

The removal of inclusions by dissolution in slag is experimentally studied by either the dip test or the confocal scanning laser microscope (CSLM)[15–24]. In the dip test, a centimeter size refractory rod is immersed in a slag for a period of time, removed and then analyzed for slag corrosion and/or penetration. This method is applied to study the dissolution of inclusions such as Al_2O_3 [18,19,23,24] and MgO [17] in steelmaking slag. The CSLM technique allows for the continuous in-situ observation of micron-size samples in real time. This is a unique feature of the CSLM technique relevant to fundamental studies in the steelmaking process.

This technique was introduced to steel research by Emi et al. [25] to study the crystal growth during solidification in Fe-C melts. Since then it has been used to examine dynamic changes such as particle collision, cluster formation and solidification at steelmaking temperatures [26,27]. Several researchers [16,28–43] have also applied the CSLM technique to study the dissolution behavior of a single oxide particle in slag. A majority of these studies [28,29,31–34,36,38–40,42,43] used the inclusion types that are available for purchase. However, the inclusion types with complex chemistry such as $CaO.6Al_2O_3$, $CaO.2Al_2O_3$, $12CaO.7Al_2O_3$ and Al_2TiO_5 are not available for purchase from suppliers.

The unavailability of certain inclusion types limits the assessment and testing of key inclusion groups important in steelmaking. In such a case, the particles can be sintered from individual components to produce the required complex inclusion type [44,45]. Wang et al. [15] produced 90% pure Al_2TiO_5 rod by reactive sintering of 99.999% Al2O3 and 99.999% TiO_2 for 150h at 1400 °C under Ar atmosphere. 1wt. % SiO_2 and 1 wt. % Y_2O_3 were added for consistency. In addition, the sol-gel technique can be used to prepare Al_2TiO_5 particles [46–49]. This technique includes production of solution with titanium tetrabutoxide, aluminum chloride and monohydrate citric acid and ethanol [47] at relatively lower temperatures. This technique cannot be applicable for inclusion dissolution work for two reasons, (a) size and (b) purity. The sol-gel technique produces particles of nanometer size [47], while the initial particle size requirement for CSLM dissolution studies is 100 micrometers or higher [39]. The mechanical properties are enhanced by addition of other oxides [48] which are undesirable for studying inclusion dissolution. In order to minimize the effects of impurities on the dissolution kinetics and mechanism of micrometer size inclusions, it is especially important to establish a production technique for inclusions that are not available for purchase.

The current work aims to establish a production technique for micrometer size non-metallic particles in a laboratory environment. In the current work, two different techniques, (1) sintering and (2) the optical floating zone method (OFZM) are assessed to produce high purity particles for dissolution experiments in CSLM. The details of these techniques are presented and results for syntheses of Al_2TiO_5 inclusions using these techniques are given. The advantages and disadvantages are discussed in terms of purity and density of the particles. The reactivity of Al_2TiO_5 and TiO_2 particles produced by the two techniques are tested with ladle type slag. The steel industry is currently working on a new generation of steels which differ significantly in composition from those currently produced. This will inevitably lead to a new range of inclusion types which will require detailed study to optimize processing. Advancing our knowledge on the production method of particles will enable a broader range of inclusions to be investigated.

3.2 Experimental materials and methods

3.2.1 Sintering

The techniques to produce high purity particles for Al_2TiO_5 by reaction sintering are adapted from literature [50]. The ratio of oxides and holding temperature were selected based on the binary phase diagram of Al_2O_3 and TiO_2 [51]. A 1:1 molar ratio of Al_2O_3 and TiO_2 powders was mixed in a ball mill for 2 hours to homogenize. The oxide powders were purchased from Alfa Aesar, U.S.A. A slurry was then prepared by mixing the oxide powder mixture into 500 ml deionized water. The slurry was vacuum filtrated with a Buchner funnel and Waterman #6 filter papers with a pore diameter of 3 μm. Particles remaining on the filter papers were placed in an oven at 115 °C for 24 hours to remove moisture. Approximately 4 wt% distilled water was added as a binder to the dried oxide powders. Nearly 7 to 10 g of mixed powder was pressed under 200 MPa for 20 s to produce 2.5 cm diameter pellets. The pellets were placed in an alumina crucible and sintered in a muffle furnace. The temperature is initially increased from room temperature to 1600 °C with a heating rate of 10 °C/min and the furnace temperature is held at this temperature for 24h [15]. The furnace is then cooled to room temperature. The particles were crushed to very fine powder and pressed again for second sintering to ensure particle homogeneity.

3.2.2 Optical floating zone method

The OFZM is a variation of the zone refining process and proceeds by melting and solidification of the material. Dabkowska et al. [52] have carried out extensive work on the production of high purity and controlled doped oxides at the Brockhouse Institute for Materials Research (BIMR), McMaster University. The NEC furnace at BIMR was used to prepare the Al_2TiO_5 crystal. In the OFZM, both congruent and incongruently melting oxides with melting point as high as 2500 ^{o}C can be prepared whereas such temperatures are difficult to reach in conventional tube furnaces [53]. Another advantage of OFZM is to use different gas atmospheres at relatively high pressure. It is beneficial specially in case of compounds like TiO_2 and Al_2TiO_5 where valance of titanium depends on the partial pressure of oxygen [54].

The high purity (99.5%) laboratory grade powder mixture of TiO_2 and Al_2O_3 in the size -100 mesh was purchased from Alfa Aesar, USA. The powder mixture is first compressed to a rod of approximately 10 cm in length. To improve the strength of the compacted rod, it is placed in a hydraulic press for approximately 20 minutes under a pressure of 60 MPa followed by drying in air. An alumina boat containing the hydraulically pressed Al_2TiO_5 rod is then sintered in a Carbolite furnace. The sintering temperature is chosen such that there is no decomposition of the material at that temperature and the material can endure the temperature for an extended period without any change in physical and chemical characteristics. The furnace is heated from room temperature to 100 °C at the rate of 1.3 °C/min followed by heating from 100 °C to 900 °C at the rate of 1.7 °C /min. The Al_2TiO_5 rod is then held at 900 °C for 360 minutes and then cooled from 900 °C to room temperature at the rate of 5 °C/min. The sintered rod is then cut into two equal halves, one half to be used as a feed rod (the rod that hangs in air from above) and the other one to be used as a seed rod (the rod that stands on support) in the OFZM [52]. Figure 3-1 (a) shows the sintered feed rod and seed rod and Figure 3-1 (b) shows the Al_2TiO_5 crystalline rod produced by the OFZM.

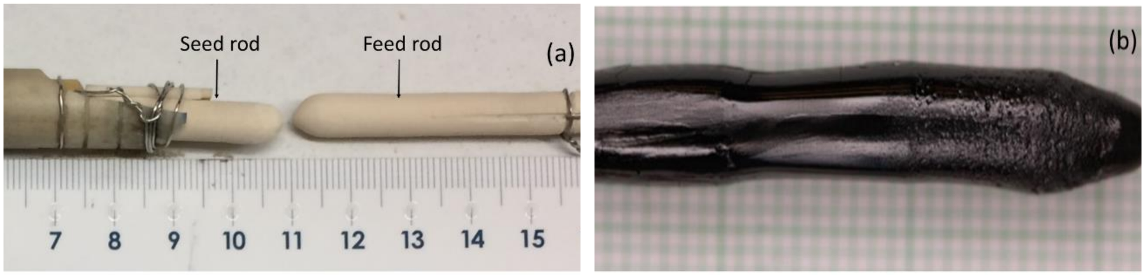

Figure 3-1 Al_2TiO_5 rod (a) after hydraulic pressing and (b) after melting

Figure 3-2 [55] shows the schematic of the set up used for the OFZM. The feed rod is held in position with the help of a platinum wire and is moved up and down as melting proceeds. The seed rod is held in a hollow alumina tube and fastened to the tube with the help of a nickel wire. The feed and seed rods rotate during the process for homogeneity of temperature and composition in the reaction zone. The halogen lamps emit radiation which is reflected by the parabolic mirrors to a point in space where the feed rod and the seed rod meet. The power of the lamp is gradually increased until a melt zone forms at the meeting point of the feed rod and the seed rod. The feed rod is moved down manually until it is used. The total time required for melting the Al_2TiO_5 rod is approximately 3 hours. After the feed rod is used and crystal forms, the furnace is shut down and the formed crystal is left to cool in the furnace for 24h.

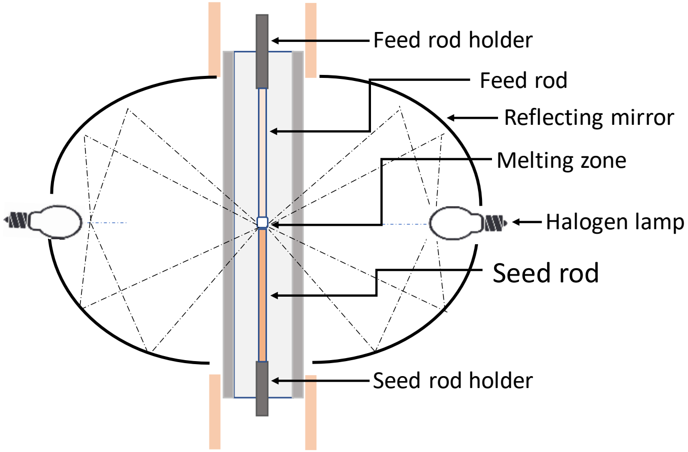

Figure 3-2 Schematic of the set up for the OFZM [86]

3.2.3 Slag preparation

There are a few considerations to be made while designing slag composition for dissolution experiments in CSLM. The slag must be transparent for clear observation of inclusion dissolution and its composition is chosen to ensure that it is liquid at the temperature of interest. Under such conditions, it is possible to follow the motion of the dissolving particle and maintain focus inside the liquid slag. Steelmaking slags mainly contain CaO, Al_2O_3, SiO_2, MgO, FeO, MnO and CaF_2. Because the CSLM technique precludes using slags containing transition oxides such as FeO and CrO_x, slag composition usually consists of CaO, SiO_2, Al_2O_3 and MgO [30, 31, 37, 41, 56, 57]. In this work, slag composition is 20.0 ± 0.7 wt% Al_2O_3, 40.0 ± 0.4 wt% CaO and 40.0 ± 0.5 wt% SiO_2. The theoretical value of liquidus temperature of slag used for dissolution experiments is 1332 ± 3 ^oC, calculated using Equilib module in Factsage 7.1^{TM}.

To prepare the slag, the laboratory grade $CaCO_3$, SiO_2 and Al_2O_3 powders were purchased from Sigma Aldrich, U.S.A. The constituent powders of appropriate proportions were initially mixed and then heated to the temperature, 50 °C higher than the liquidus temperature of slag, to fully melt in a platinum crucible. After homogenization of molten slag, it was quenched and crushed. This process was repeated twice to ensure slag homogeneity. The slag composition is confirmed by the inductively coupled plasma optical emission spectroscopy (ICP-OES). Approximately 0.1 g of crushed slag powder is compacted into a platinum crucible (10 mm O.D. x 5 mm height) that is used for dissolution experiments in CSLM. The platinum crucible is placed in a vertical tube furnace at a temperature 50 °C above its liquidus temperature to completely melt the slag. After holding for half an hour at the elevated temperature, the slag is degassed for 15 seconds at 760 millitorr. The vertical tube furnace is refilled with argon and vacuumed again for 15 seconds at 760 millitorr to remove the gas bubbles entrapped in molten slag.

3.2.4 Experimental set-up for reactivity test

The reactivity of the particles with slag was tested using a Lasertec VL2000DX-SVF17SP CSLM. The equipment consists of an infrared gold imaging furnace and a laser microscope situated immediately above the furnace. The particle-slag system was placed inside the furnace. The schematic diagram of the experimental setup inside the heating chamber is illustrated in Figure 3-3 [57]. A single TiO_2 or Al_2TiO_5 particle was placed on the surface of the pre-molten slag in a platinum crucible. The particle, sample holder and crucible were heated to the experimental temperature under 99.999% pure Ar atmosphere at 200 ml/min flow rate and a pressure of 1 atm.

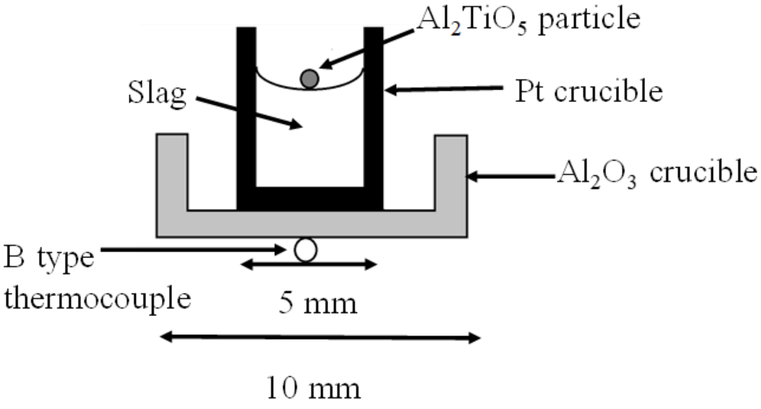

Figure 3-3 Schematic of sample and crucible configuration in CSLM

The temperature was measured using a B type thermocouple, attached to the bottom of the crucible holder. A 99.99 % pure Fe disk with 1 mm thickness was used to calibrate the surface temperature of a sample. It was found that the surface temperature of the sample is 63 ± 5 °C higher than that of thermocouple temperature when pure Fe was melted. This temperature difference was applied for all the experiments. A programmable temperature controller provides support to rapid heating and cooling rates up to 1000 °C/min with a maximum temperature of 1700 °C. Figure 3-4 provides the thermal cycle for the reactivity experiments. The system is initially heated from room temperature to 150 °C at a rate of 40 °C/min, followed by heating at 1000 °C/min to a temperature which is 100 °C below the desired experimental temperature. Then the temperature is raised to the dissolution temperature at the rate of 100 °C/min. It is held at 1430 °C during the dissolution process and cooled to room temperature with a cooling rate of 100 °C/min. In this study, the rapid heating rate of 1000 °C/min is selected to avoid any dissolution before the desired experimental temperature is reached. Similar heating rates were selected in the study of Feichtinger et al. to study the dissolution of SiO_2 particles[76].

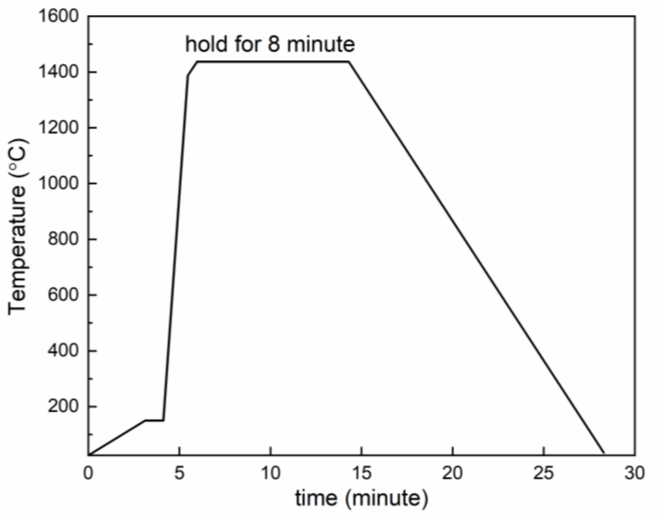

Figure 3-4 Schematic of thermal cycle used for dissolution experiments of Al_2TiO_5 particles in slag

3.2.5 Thermodynamics of inclusion dissolution

Figure 3-5 shows equilibrium phases that may form during dissolution of TiO_2 as well as Al_2TiO_5 in slag at 1430 °C. The phase diagram is constructed with the help of Factsage 7.1 using the Factoxid data base. The four-component phase diagram is presented on a ternary graph by assuming a fixed proportion of Al_2O_3 in the Al_2O_3-CaO-SiO_2-TiO_2 and Al_2O_3-CaO-SiO_2-Al_2TiO_5 system. Dark marker on the CaO-SiO_2 axis represents the initial slag compositions. Based on an assumption of a straight dissolution path (dotted lines), $CaTiO_3$ is likely to form on the surface of TiO_2 particle while CaO.6Al_2O_3 and Al_2O_3 might form on the surface of Al_2TiO_5 particle. In a previous study on dissolution mechanism of TiO_2 in same slag by Ren et al. [58] $CaTiO_3$ phase was detected at the interface between $CaO-SiO_2-Al_2O_3$ type slag and TiO_2 rod in the temperature range between 1370 and 1430 °C. The liquid phase field on the phase diagram for TiO_2 is much larger than the corresponding phase profile for the Al_2TiO_5 slag system which implicates a higher thermodynamic driving force for TiO_2 dissolution than Al_2TiO_5 dissolution.

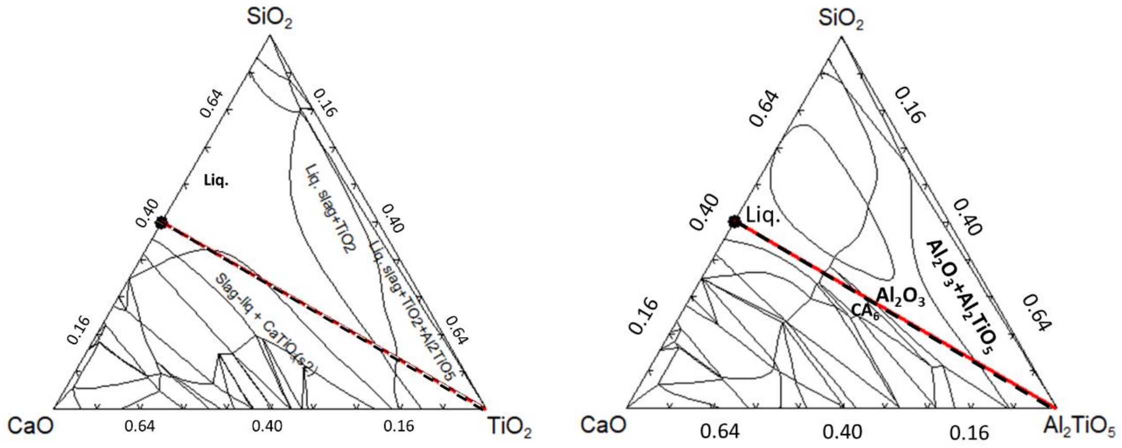

Figure 3-5 Prediction of phases that might form during dissolution of (a) TiO_2 and (b) Al_2TiO_5 in a 20 Al_2O_3-40 CaO-40 SiO_2 slag at 1430 °C using FactSage 7.1^{TM} thermochemical software

3.3 Results and discussions

3.3.1 Synthesis of Al_2TiO_5 particles

Figure 3-6 shows the comparison of the powder X-ray diffraction (XRD) pattern from powder mixture and sintered pellet. The pellet obtained from sintering of Al_2TiO_5 powder was crushed to obtain fine powder to be analyzed using XRD technique. A quantitative analysis of the pattern shows that there was 76 % Al_2TiO_5 phase in the sintered structure.

This finding indicates that production yield of Al_2TiO_5 particles using current sintering technique is relatively lower than the technique reported by Wang et al.[1] They obtained a yield of 90% by sintering Al_2O_3 and TiO_2 with 1 wt % Y_2O_3 and 1 wt. % SiO_2 at 1400 °C for 150 h under argon atmosphere. Sintering technique has been conventionally used to produce oxides such as Al_2TiO_5 because it is a cheap and easily accessible technique for researchers. Additives like MgO and SiO_2 are introduced to form a liquid phase which acts as a binder and increases the mechanical properties of Al_2TiO_5 [54]. The authors prefer not to add MgO and SiO_2 since these oxides can influence the dissolution path. In summary, the sintering technique is not suitable to investigate the in-situ dissolution of Al_2TiO_5 particles.

A section from the facetted region of the grown crystal of Al_2TiO_5 is extracted and is crushed to form particles. The particle size ranges between 10 µm and 1000 µm. The Al_2TiO_5 phase was confirmed by XRD as provided in Figure 3-7. The comparison of the XRD pattern generated by solving the crystal structure of Al_2TiO_5 and pattern generated from the database [59] shows excellent agreement. The comparison of XRD results for Al_2TiO_5 particles indicates that OFZM provides a solution to produce particles with high purity. Using a similar procedure, OFZM was applied to produce TiO_2 particles.

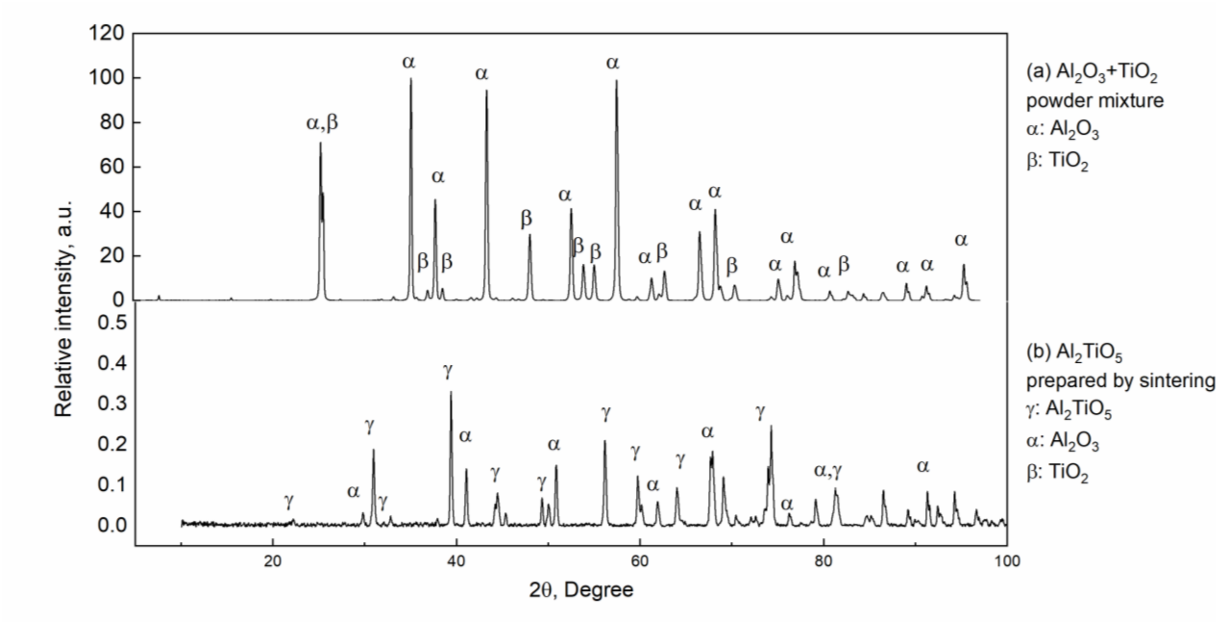

Figure 3-6 XRD pattern from (a) powder mixture of TiO_2 and Al_2O_3 and (b) Al_2TiO_5 prepared by sintering at 1600 °C for 24h in air twice

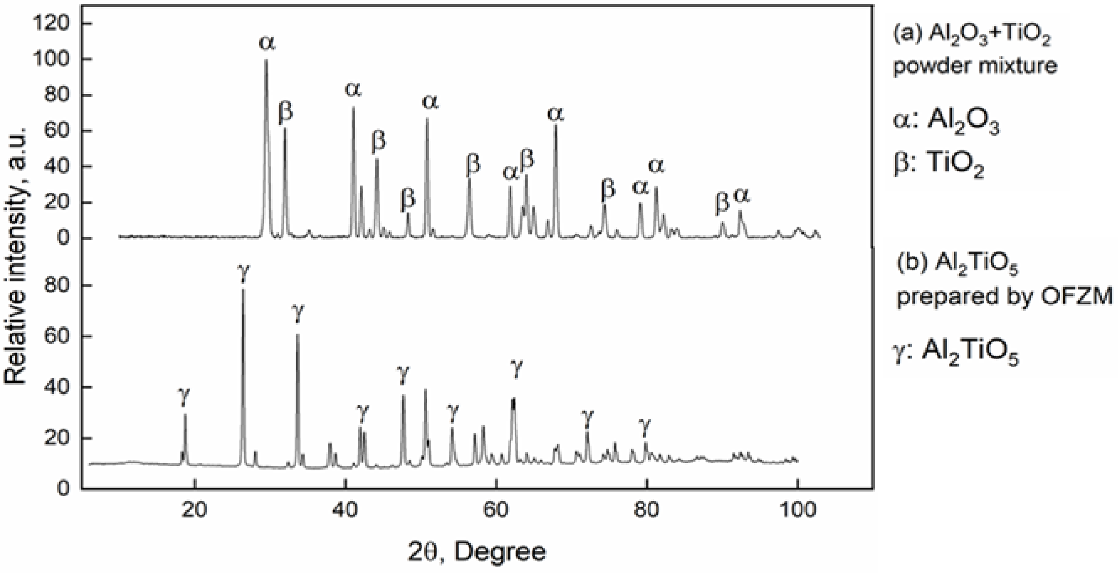

Figure 3-7 Comparison of XRD patterns for (a) powder mixture of TiO_2 and Al_2O_3 (b) Al_2TiO_5 prepared by the OFZM

The density of sintered particles was measured using a pycnometer at room temperature and equals 2890 ± 80 kg/m^3. The density reported in literature is 3702 kg/m^3 [54]. The density value measured for particles produced by OFZM was 3810±30 kg/m^3. A comparison between these values suggests that our sintered particles have 32 vol. % porosity. The particle density was corrected for expansion at experimental temperatures using Equation 3-1 [54]. The linear thermal expansion coefficient of Al_2TiO_5 is available for temperatures up to 1000 °C [54]. The expansion coefficient was extrapolated to 1430 °C assuming a linear increase with temperature from 20 °C to 1430 °C. This is a reasonable assumption because it is reported that the densities of TiO_2 and Al_2O_3 expand linearly with temperature from 25 °C to 1600 °C [60]. The mean Al_2TiO_5 linear thermal expansion coefficient αL, equals 8.7 x10-7 °C-1 [60].

$$\rho = \frac{\rho_0}{1 + 3\alpha_L \Delta T} \tag{3-1}$$

where ρ_0 and α_L denote density in kg/m^3 at room temperature and linear thermal expansion coefficient in °C-1 respectively, and ΔT denotes the temperature difference in °C. Assuming isotropic behavior and applying the linear thermal expansion coefficient [54], Al_2TiO_5 density was calculated and equals approximately 3806 kg/m^3 at experimental temperatures.

Sintering processing time is approximately 73 hours including mixing powders and sintering itself while the processing time for OFZM is approximately 27 hours. The processing time for sintering is higher because the process is repeated to ensure homogeneity of the product and the maximum heating rate of the vertical tube furnace is limited to 10 °C/min.

3.3.2 Morphology of Al_2TiO_5 particles

Typical microstructure and corresponding elemental analyses were carried out through a scanning electron microscope energy-dispersive spectroscope (SEM-EDS). Figure 3-8 shows the mapped images of a single Al_2TiO_5 particle produced using OFZM. This analysis provides a quantitative characterization of the additions before the experiment. It is found that Al, Ti and O are present uniformly throughout the structure of the particle and there is no porosity observed in the particle structure. SEM image and elemental mapping of sintered Al_2TiO_5 particles is shown in Figure 3-9. Al, Ti and O are also present uniformly throughout this particle, however the particle is significantly more porous than the particle produced by OFZM.

In summary, the particles produced by OFZM are suitable for dissolution experiments due to their high purity and density. The porous nature of the sintered particles where gas generation is aggravated due to increased contact with slag, is likely to limit the observation of dissolution experiments. Rapid gas formation and bursting of those bubbles pushes the particle away in random directions. Therefore, the reactivity test was conducted using particles produced by OFZM.

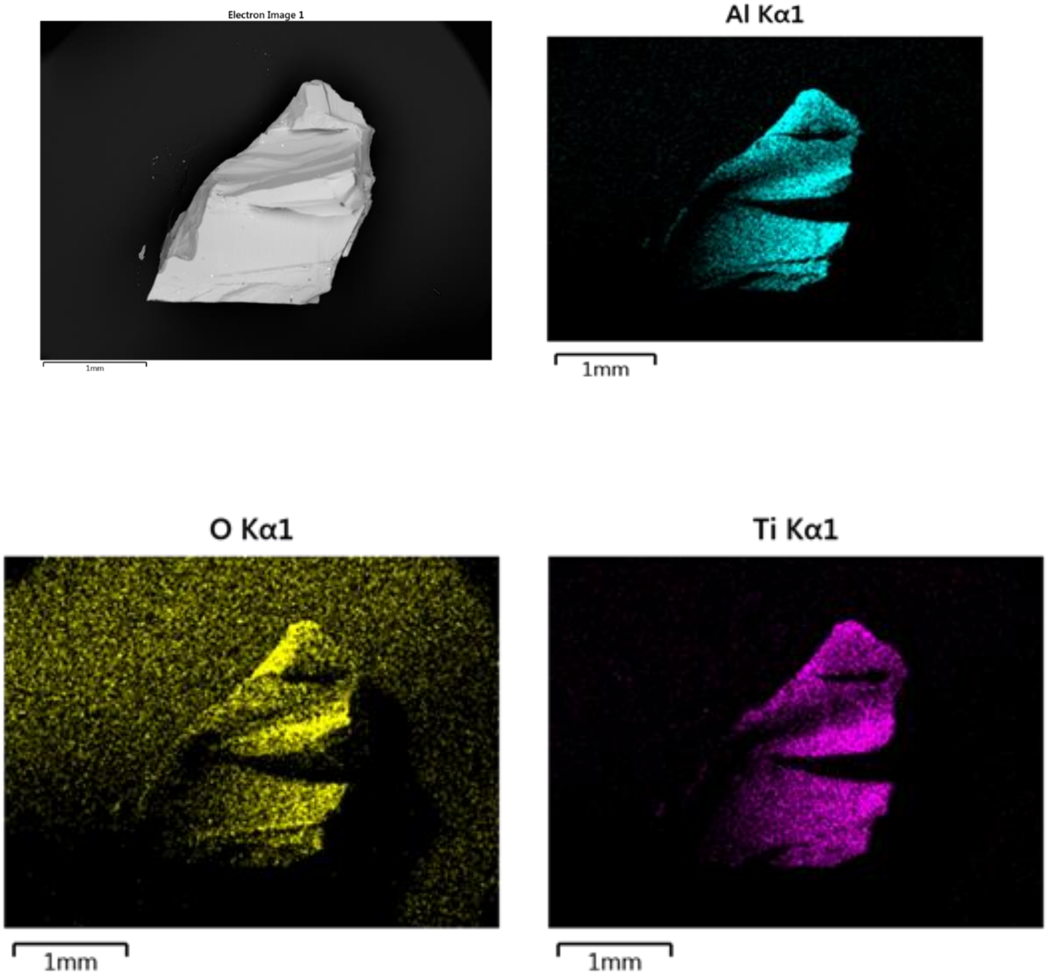

Figure 3-8 Elemental map of Al_2TiO_5 particle prepared by the OFZM showing uniform distribution of Al, Ti and O in the particle

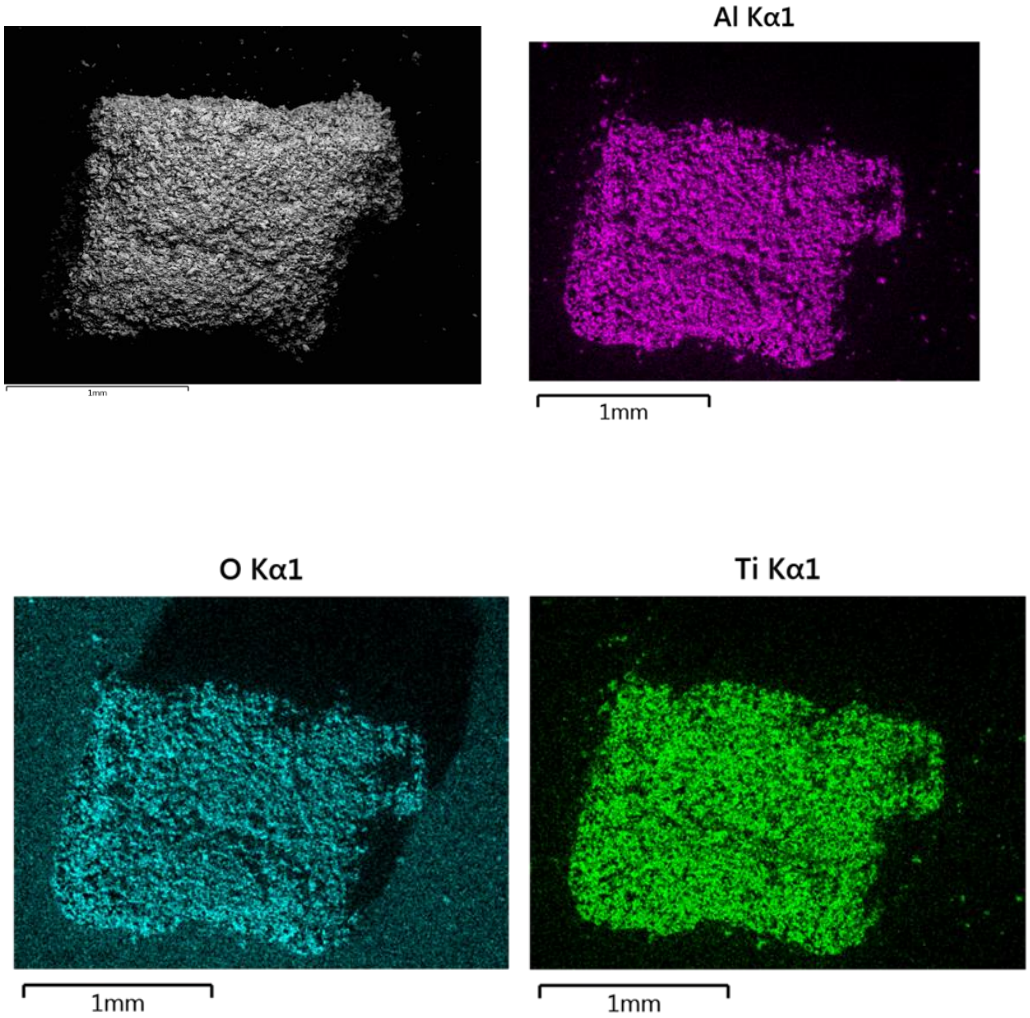

Figure 3-9 SEM images and elemental map of Al, Ti and O in the Al_2TiO_5 particle prepared by sintering technique

3.3.3 Reactivity of particles during dissolution

The reactivity of the particles with slag was assessed with respect to its behavior during dissolution in slag using the CSLM at 1430 °C by applying the heating cycle shown in Figure 3-4. A single TiO_2/Al_2TiO_5 particle was placed on top of the slag and the dissolution process is recorded with the help of a charge couple device (CCD) camera situated above the gold coated infrared image furnace (IIF). The videos captured by CSLM were saved and converted into pictures using Virtual Dub open-source software developed by Lee [61]. The oxide particle is distinguished from the slag based on contrast in each frame. The weight of the particle used in each experiment was less than 1 wt % of the slag.

Figure 3-10 and Figure 3-11 show representative series of images from the dissolution of TiO_2 and Al_2TiO_5 in slag at 1430 °C, respectively. Time zero is chosen when the set temperature reaches the experimental temperature and the particle is completely covered by the bulk slag. The dark gray region represents the particle while light gray region represents the slag. The yellow outline in Figure 3-10 and Figure 3-11 is a manually drawn border around the particle to distinguish the interface between particle and slag. It is seen from the figures that the particle prepared by the OFZM does not dissolve to a large extent before reaching the desired experimental temperature and maintain the physical integrity at the particle boundary during dissolution. The dissolution takes place gradually with no erratic erosion at any specific site of the particle and is accompanied by less severe gas generation and bursting. This indicates that reproducibility of the experiments can be achievable by using particles produced by OFZM.

The TiO_2 particles rotates slowly as it dissolves in the slag. The TiO_2 particle breaks into smaller pieces as they dissolve, and the broken pieces present a different appearance than the original particle, see Figure 3-10 (a) and (c) for comparison. The change in hue of the TiO_2 particle as it dissolves in the slag might be due to a change in valence of Ti^{+3} to Ti^{+4} at high temperature [62,63]. For Al_2TiO_5 particles shown in Figure 3-11 (b) and (c), there is also a difference in hue of the particle, being dark at the center and relatively lighter at the periphery of the particle.

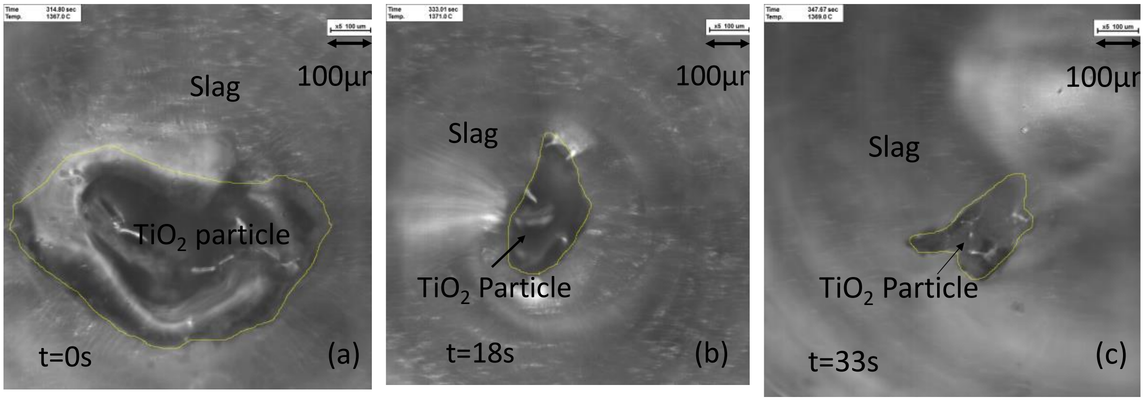

Figure 3-10 Dissolution process of TiO_2 particle prepared by the OFZM in slag

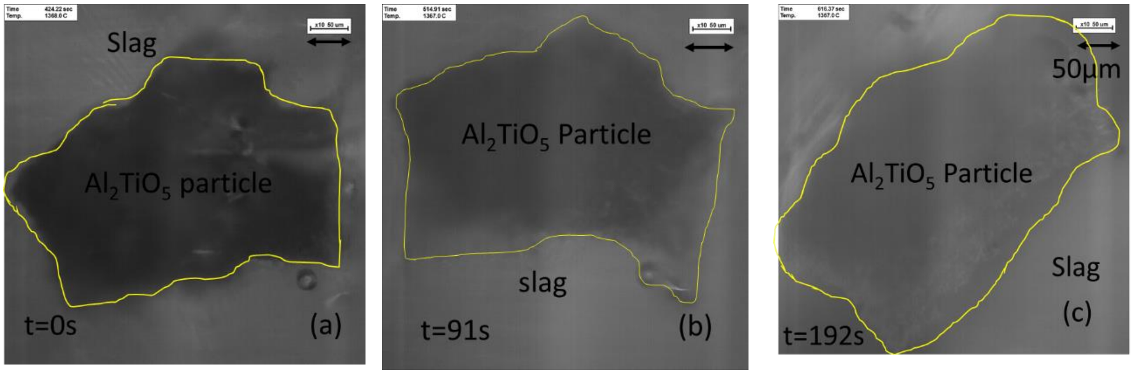

Figure 3-11 Dissolution process of Al_2TiO_5 particle prepared by the OFZM in slag

Dissolution was measured in terms of changes in particle area with time. It can be seen from both figures that the actual shape of the particles is irregular. Although, the sintering and OFZM provide freedom with respect to particle preparation, certain restrictions still exist. It should be noted that there is no control on the particle shape and size prepared by both techniques. In this study, it was assumed that the particle had spherical shape for simplicity to determine the dissolution mechanism using shrinking core models (SCM).

The equivalent radius of a circle was calculated from the measured particle area which is shown by yellow lines. The images were further analyzed using ImageJ ^{TM}, a public-domain image processing program. Figure 3-12 shows representative data from the change in equivalent circular radius with time for TiO_2 and Al_2TiO_5 particles in slag at 1430 °C. There is a gradual decrease in TiO_2 particle size with time. The size of Al_2TiO_5 particle remains virtually unchanged for approximately 4000 seconds. In the figure, only data points until 60s is shown to present a comparison with TiO_2 particles. This finding was confirmed from in-situ images shown in Figure 3-11.

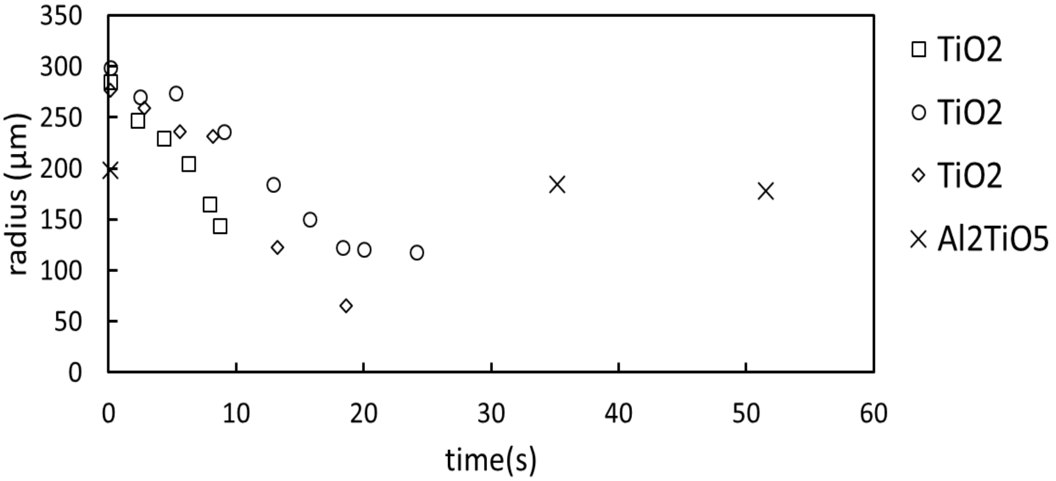

.

Figure 3-12 Change in particle size with time for TiO_2 and Al_2TiO_5 particle

According to phase diagram shown in Figure 3-5, $CaO.6Al_2O_3$ might form during dissolution at the interface of Al_2TiO_5 particle and slag which prevents further dissolution of Al_2TiO_5. Another explanation can be based on the decomposition of Al_2TiO_5 at high temperature under 99.999% argon atmosphere. Seifert and Aldinger [64] show that under high vacuum as 10^{-9} atm, Al_2TiO_5 decomposes to non-stoichiometric aluminium titanate, alumina and oxygen.

3.4 Rate controlling mechanism

The shrinking core model and the diffusion into a stagnant fluid model have both been applied to determine the dissolution mechanism of inclusions in steelmaking slags [30, 31, 42]. Their development and applications can be found elsewhere [31]. The diffusion into a stagnant fluid control model was based on the Fick's first and second laws of diffusion. Feichtinger et al. [31] applied a fitting parameter that controls the shape of the dissolution curve and it is strongly related to the slag viscosity. This model only considers mass transfer in the slag as a rate controlling step. In this study, the shrinking core models for spherical particle with shrinking size was applied to understand the rate controlling mechanism for a TiO_2 particle in the bulk slag [65]. The authors considered SCM in this study since chemical reactions at the interface can be a potential rate controlling step for the dissolution process. The model suggests (a) linear relationship of radius with time for chemical reaction control as shown by equation 3-2 and (b) parabolic relation of radius with time as shown by equation 3-3 for mass transfer control in Stoke's regime.

$$\frac{R_c}{R_0} - 1 = \frac{bK_R\Delta C}{\rho_{particle} R_0} t \qquad (3\text{-}2)$$

$$\left(\frac{R_c}{R_0}\right)^2 - 1 = \frac{2b\Delta CD}{\rho_{particle} R_0^2} t \tag{3-3}$$

Where R_c and R_0 are instantaneous and initial radii (in m), t is the instantaneous time (in s), $\rho_{particle}$ is the particle density (in kg/m^3), b is the stoichiometric constant equal to 1, ΔC is the difference in concentration of the rate-controlling species in bulk slag and slag at saturation (in kg/m^3), K_R is the first-order rate constant for the surface reaction in (m/s), and D is the diffusivity of the species under consideration (in m^2/s).

To elucidate on the rate-controlling mechanism, for dissolution of TiO_2, the chemical reaction control and mass transfer control curves using SCM are compared to the dissolution data and analyzed by regression analysis. The degree of fit parameter, R^2, is used to identify the rate-controlling step. The method was adapted from a study by Monaghan and Chen [28]. This method was used in a previous publication by the authors to analyze Al_2O_3 and Al_2TiO_5 dissolution in similar slag composition [56, 66]. Figure 3-13 shows that the R^2 values for dissolution experiments for chemical reaction control are 0.97, 0.96 and 0.93. Figure 3-14 shows that the R^2 values for dissolution experiments for mass transfer control are 0.98, 0.94 and 0.96. Although the values for chemical reaction control mechanism are higher than those for mass transfer, it is difficult to discern between the two aforesaid rate-controlling mechanisms based on regression analysis. It is important to note that the assumption of spherical particle shape will introduce an error into data analysis and further complication to the decision on the rate-controlling step. Particularly, mass transfer controlled dissolution is more sensitive to the shape of the particle. As yet there is no better methodology proposed in the literature. The effect of particle shape on the dissolution rate and mechanism is an important topic and worth of future research for the current authors.

Based on the thermodynamic analysis shown in Figure 3-5 (a), $CaTiO_3$ might be an intermediate product during dissolution. This phase was detected in the study of Ren et al. [58] during the dissolution of TiO_2 substrate in a slag of same composition in the temperature range of 1370-1430 °C. The presence of $CaTiO_3$ at the particle/slag interface might indicate towards a chemical reaction control. Further, the reaction constant, k_R is calculated using equation 3-2 and is listed for three experiments in Table 3-1. For the calculation, ΔC TiO_2 equals 283 kg/m^3 at the interface of slag-TiO_2 particle obtained from the phase diagram. The density of TiO_2 is equal to 4090 kg/m^3 at 1430 °C which is obtained from literature and extrapolated to high temperature using coefficient of expansion [60]. The average value of k_R is 1.65×10^{-4} m/s. To the best knowledge of the authors, there is no measured chemical reaction rate constant value at 1430 °C available in literature. From studies on alumina dissolution by Monaghan and Chen [28], the values reported for chemical reaction rate constant in slag of similar composition are comparable to order of magnitude with those reported in our study. Croker et al. [67] reported k_R values for in situ crystallization of $CaTiO_3$ at 250 °C. The obtained rate constant value from their study [67] is extrapolated to 1430 °C following Arrhenius relationship. The rate constant value thus obtained is 6.3×10^4 s^{-1}. The discrepancy with respect to the value shown in Table 3-1 may be related to the difference in experimental conditions for the formation of $CaTiO_3$ in the two cases. In the work of Croker et al.[67] $CaCO_3$ was reacted with TiO_2 in sodium aluminate solution to produce $CaTiO_3$ whereas in the current work Ca^{2+} and O^{2-} from ionic slag reacts with TiO_2 to form $CaTiO_3$. Also, anatase was used in their work while rutile is used in the current study. In a different study by De Pretis et al. [90] the rate constant for formation of $CaTiO_3$ by sintering of $CaCO_3$ and TiO_2 to be 7.0 at 1430 °C. This value is very different from values obtained by extrapolating values reported by Croker et al.[67]. To summarize, the rate constant values reported in literature for the formation of $CaTiO_3$ are few and far between and no reasonable comparison can be made with values obtained from the SCM found in the current work. Thus, further SEM analysis is required to characterize the TiO_2 particle/slag interface to confirm if a chemical reaction is controlling the dissolution rate, this remains as future work for this research.

The mass transfer control in Stoke's regime model for shrinking particles is applied to calculate the diffusivity of Ti^{4+} ion in the slag as shown in equation 3-3. The value of the diffusivity obtained from each experiment is in the order of 10^{-8} m^2/s as listed in Table 3-2. This value is in reasonable agreement with the values reported in a previous study by the authors [56]. The diffusivity of Ti^{4+} was in the order of 10^{-7} m^2/s at 1550 °C. This value was calculated using the same methodology under the assumption of mass transfer control in the slag. However, this value is higher than the diffusivity of Ti^{4+} reported in literature which is in the order of 10^{-12} m^2/s [51]. Ren et al. [58] estimated the diffusivity of TiO_2 as 4.5×10^{-12} m^2/s in a slag of same composition as that used in the current work at 1430 °C. In their study, they used a TiO_2 disc of 10 mm O.D. x 5 mm height and 4g of slag. The interface of disc and slag was studied with SEM/EDX and the obtained concentration profile is compared with profile obtained from solution of Fick's second law. The authors suggest that the difference in results is related to two factors (1) the particle size and (2) the role of convection in mass transfer. The scale from bulk materials to inclusions could significantly affect the observed dissolution kinetics. Secondly, strong convection is observed during the dissolution of TiO_2 but the phenomenon is not incorporated in the SCM with mass transfer control in Stoke's regime. The mass transfer model assumes a Sherwood number of 2, which is valid for a small particle with very small Reynold's number. Yan et al. [69] found that the diffusivity values are affected by an order of magnitude for the mass transfer coefficient when effect of fluid flow is not incorporated while estimating the diffusivity values from CSLM data for Al_2O_3 and MgO dissolution. A more rigorous multicomponent diffusion kinetic model is needed to properly illustrate the dissolution mechanism.

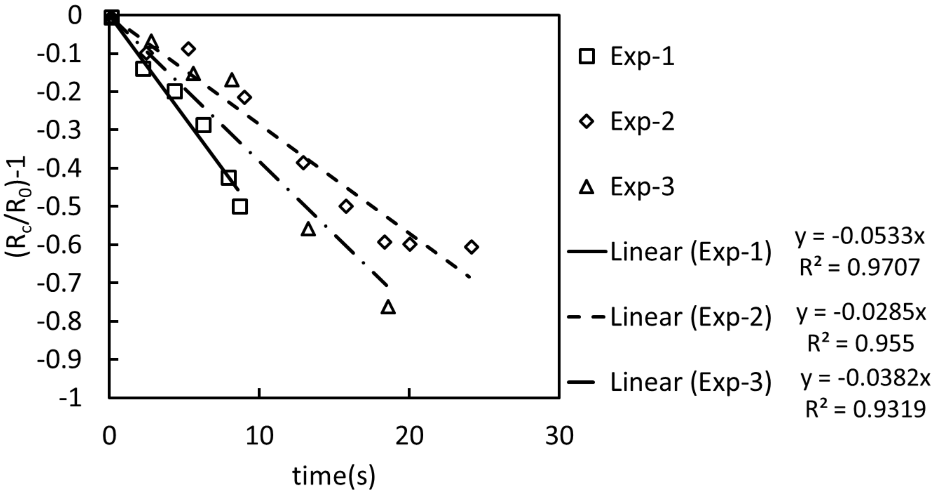

Figure 3-13 Comparison of TiO_2 dissolution data in slag with SCM, assuming chemical reaction control, hollow markers indicate data points and solid line indicates regression fit to data

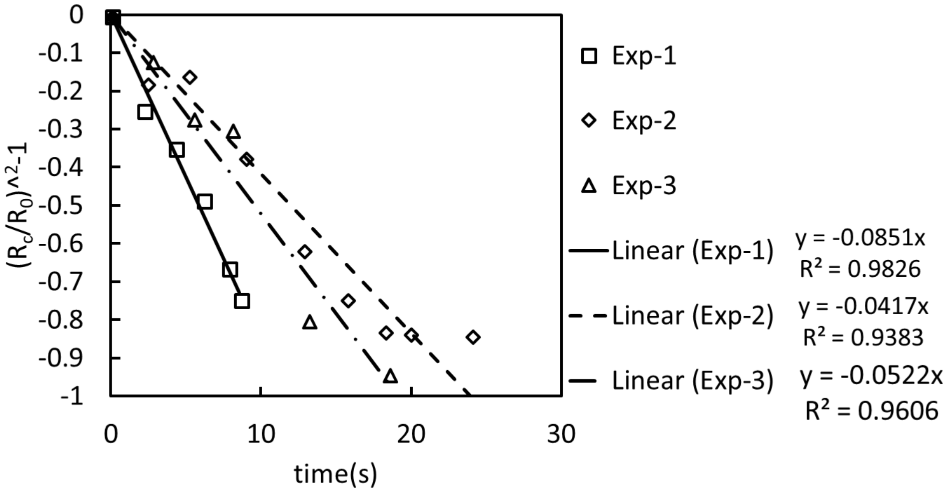

Figure 3-14 Comparison of TiO_2 dissolution data in slag with SCM, assuming mass transfer control in Stoke's regime, hollow markers indicate data points and solid line indicates regression fit to data

Table 3-1 Estimated chemical reaction rate obtained from chemical reaction control model

Experiment	Degree of fit, R^2	Slope of (R/R_0)-1 vs t	R_0, µm	K_R TiO_2, m/s
Experiment 1	0.97	-0.0533	287	2.2E-04
Experiment 2	0.96	-0.0285	301	1.2E-04
Experiment 3	0.93	-0.0382	278	1.5E-04

Table 3-2 Estimated diffusivity values obtained from mass transfer control model

Experiment	Degree of fit, R^2	Slope of (R/R_0) ^2-1 vs t	R_0, μm	D TiO_2, m^2/s
Experiment 1	0.98	-0.0851	287	5.1E-08
Experiment 2	0.94	-0.0417	301	2.7E-08
Experiment 3	0.96	-0.0522	278	2.9E-08

3.5 Conclusions

The focus of this work is on the method of production of non-metallic particles in laboratory environment. While most researchers obtain the particles from reagent suppliers, there exist different options to prepare these particles such as the sintering and the OFZM. These techniques provide independence to researchers in terms of production time and freedom of choice of the desired inclusion types. To obtain accurate and consistent kinetic data, the particles to be used for dissolution experiments in CSLM should be consistent in properties such as density and porosity. The importance of particle preparation is enhanced by the fact that only one particle is used in every CSLM experiment and the data thus obtained is used to represent dissolution kinetics of that inclusion type. Although, the sintering and OFZM provide freedom with respect to particle preparation, certain restrictions still exist. The particles prepared are not spherical in shape while the SCM used to explain the dissolution mechanism assumes a spherical shape. This oversimplification might affect the decision on the rate controlling step.

The following conclusions can be made:

(a) OFZM is proven to be a better production technique of micro-particles for studying in situ dissolution using CSLM in comparison to the sintering technique with respect to high purity and less porosity of the particles. Pores are present in sintered Al_2TiO_5 particles while they are absent in the particles prepared by the OFZM as observed in SEM. The particle obtained from the OFZM dissolved with less gas generation throughout the reaction surface. The interface between particle and slag was observed clearly during dissolution experiments using CSLM when particles prepared by OFZM are used.

(b) At 1430 °C, the Al_2TiO_5 particles didn’t dissolve at all whereas TiO_2 particles completely dissolved in 200 seconds. Preliminary kinetic analysis with TiO_2 dissolution data from CSLM is unable to distinguish between mass transfer control and chemical reaction control. Further SEM characterization of interface between particle and slag is required to determine the possible phases formed at the interface. The determination of dissolution mechanism of TiO_2 remains as future work for the authors. A more rigorous multicomponent diffusion kinetic model is needed to properly illustrate the dissolution mechanism.

3.6 Acknowledgements

The authors would like to thank the Natural Sciences and Engineering Research Council (Project No. 20000514) and Canada Foundation for Innovation John Evans Leaders Fund (CFI JELF, Project No. 32826). We would also like to thank Professor Bruce D. Gaulin, director of the Brockhouse Institute for Materials Research at McMaster University for allowing us to use this optical floating zone furnace.

3.7 References

[1] S. Basu, S.K. Choudhary, N.U. Girase,ISIJ Int. 2004, 44, 1653 .

[2] P. Kaushik, R. Lule, G. Castillo, J.C. Delgado, F. Lopez, C. Perim, G. Pigatti, B. Henriques, F. Barbosa, A. Nascimento,Iron Steel Technol. 2016, 13, 168 .

[3] P. Kaushik, J. Lehmann, M. Nadif,Metall. Mater. Trans. B Process Metall. Mater. Process. Sci. 2012, 43, 710 .

[4] Y. Gao, K. Sorimachi,ISIJ Int. 1993, 33, 291 .

[5] D. Park, I. Jung, P. Rhee, H. Lee,ISIJ Int. 2004, 44, 1669 .

[6] K. Mukai, L. Zhong, M. Zeze,ISIJ Int. 2006, 46, 1810 .

[7] P. Kaushik, D. Kruse, M. Ozgu,Rev. Métallurgie 2008, 105, 92 .

[8] A. Karasangabo, C. Bernhard,J. Adhes. Sci. Technol. 2012, 26, 1141 .

[9] H. Cui, Y.P. Bao, M. Wang, W.S. Wu,Int. J. Miner. Metall. Mater. 2010, 17, 154 .

[10] Y. Gao, K. Sorimachi,ISIJ Int. 1993, 33, 291 .

[11] P. Kaushik, R. Lule, G. Castillo, J.C. Delgado, F. Lopez, C. Perim, G. Pigatti, B. Henriques, F. Barbosa, A. Nascimento,in Iron and Steel Technology, vol. 13, 2016, 168.

[12] S.-R. Story, G.-E. Goldsmith, G.-L. Klepzig,Rev. Métallurgie 2008, 105, 272 .

[13] C. Lyons, P. Kaushik,Steel Res. Int. 2011, 82, 1394 .

[14] R.C. Nunnington, N. Sutcliffe,in 2001 Electric Furnace Conference Proceedings, 2001, 1.

[15] D. Wang, J. Liu, M. Jiang, F. Tsukihashi, H. Matsuura,Int. J. Miner. Metall. Mater. 2011, 18, 646 .

[16] B.J. Monaghan, S.A. Nightingale, L. Chen, G.A. Brooks,in International Conference on Molten Slags Fluxes and Salts, South Africa, 2004, 585.

[17] K.H. SANDHAGE, G.J. YUREK,J. Am. Ceram. Soc. 1988, 71, 478 .

[18] Samaddar, B.N., W.D. Kingery, Cooper Jr.A.R.,J. Am. Ceram. Soc. 1964, 47, 249 .

[19] A.R. COOPER, W.D. KINGERY,J. Am. Ceram. Soc. 1964, 47, 37 .

[20] S.A. Nightingale, G.A. Brooks, B.J. Monaghan,Metall. Mater. Trans. B 2005, 36, 453 .

[21] K. Sandhage, G. Yurek,J. Am. Ceram. Soc. 1990, 73, 3643 .

[22] K.H. Sandhage, G.J. Yurek,J. Am. Ceram. Soc. 1990, 73, 3633 .

[23] X. Yu, R.J. Pomfret, K.S. Coley,Metall. Mater. Trans. B Process Metall. Mater. Process. Sci. 1997, 28, 275 .

[24] S. Taira, K. Nakashima, K. Mori,ISIJ Int. 1993, 33, 116 .

[25] H. Yin, H. Shibata, T. Emi, M. Suzuki,ISIJ Int. 1997, 37, 946 .

[26] J. Wikström, K. Nakajima, H. Shibata, A. Tilliander, P. Jönsson,Ironmak. Steelmak. 2008, 35, 589 .

[27] W. Mu, N. Dogan, K.S. Coley,in Scanmet V, vol. 3.

[28] B.J. Monaghan, L. Chen,Ironmak. Steelmak. 2006, 33, 323 .

[29] D. Roy,J. Phys. Chem. Solids 2007, 68, 2321 .

[30] S. Michelic, J. Goriupp, S. Feichtinger, Y.B. Kang, C. Bernhard, J. Schenk,Steel Res. Int. 2016, 87, 57 .

[31] S. Feichtinger, S.K. Michelic, Y.B. Kang, C. Bernhard,J. Am. Ceram. Soc. 2014, 97, 316 .

[32] J. Liu, M. Guo, P.T. Jones, F. Verhaeghe, B. Blanpain, P. Wollants,J. Eur. Ceram. Soc. 2007, 27, 1961 .

[33] M. Valdez, K. Prapakorn, A.W. Cramb, S. Sridhar,Ironnmaking Steelmak. 2002, 29, 47 .

[34] K.W. Yi, C. Tse, J.H. Park, M. Valdez, A.W. Cramb, S. Sridhar,Scand. J. Metall. 2003, 32, 177 .

[35] B.J. Monaghan, L. Chen,Steel Res. Int. 2005, 76, 346 .

[36] B.J. Monaghan, L. Chen, J. Sorbe,Ironmak. Steelmak. 2005, 32, 258 .

[37] F. Verhaeghe, J. Liu, M. Guo, S. Arnout, B. Blanpain, P. Wollants,Appl. Phys. Lett. 2007, 91, 124104 .

[38] X. Guo, M. Guo, Z. Sun, J. Van Dyck, B. Blanpain, P. Wollants,in Materials Science and Technology Conference, 2010, 1739.

[39] S. Sridhar, A.W. Cramb,Metall. Mater. Trans. B 2000, 31, 406 .

[40] S.H. Lee, C. Tse, K.W. Yi, P. Misra, V. Chevrier, C. Orrling, S. Sridhar, A.W. Cramb,J. Non. Cryst. Solids 2001, 282, 41 .

[41] B.J. Monaghan, L. Chen,J. Non. Cryst. Solids 2004, 347, 254 .

[42] J. Liu, F. Verhaeghe, M. Guo, B. Blanpain, P. Wollants,J. Am. Ceram. Soc. 2007, 90, 3818 .

[43] A.B. Fox, M.E. Valdez, J. Gisby, R.C. Atwood, P.D. Lee, S. Sridhar,ISIJ Int. 2004, 44, 836 .

[44] Ryosuke Maki, Yoshikazu Suzuki,J. Ceram. Soc. Japan 2013, 1217, 568 .

[45] B. Freudenberg, A. Mocellin,J. Am. Ceram. Soc. 1987, 70, 33 .

[46] I.J. Kim,J. Ceram. Process. Res. 2010, 11, 411 .

[47] M. Sobhani, H.R. Rezaie, R. Naghizadeh,J. Mater. Process. Technol. 2008, 206, 282 .

[48] T. Woignier, P. Lespade, J. Phalippou, R. Rogier,J. Non Cryst. Solids 1988, 100, 325 .

[49] S.J. Kalita, V. Somani,Mater. Res. Bull. 2010, 45, 1803 .

[50] B.M. Mohamed, J.H. Sharp,J. Mater. Chem. 1997, 7, 1595 .

[51] M. Tanaka, M. Haniu, K.T. Yasunobu, T.R. Norton,Amino Acid Sequence of the Anthopleura Xanthogrammica Heart Stimulant, Anthopleurin A, vol. 16, Verlag Stahleisen mbH, 1977.

[52] H.A. Dabkowska, A.B. Dabkowski,in Springer Handbook of Crystal Growth, Springer, Berlin, 2010, 367.

[53] H.A. Dabkowska, B.D. Gaulin,in International school on crystal growth of technologically important electronic materials, 2003, 341.

[54] I.B. De Arenas,in Sintering of Ceramics - New Emerging Techniques, D.A. Lakshmanan, ed., 1st Ed., InTech, 2012, 503.

[55] H.A.Dabkowska, A.B.Dabkowska,in In bulk crystal growth: basic techniques, Elsevier, ed., 2015, 283.

[56] M. Sharma, W. Mu, N. Dogan,Jom 2018, 70, 1220 .

[57] K. Miao, A. Haas, M. Sharma, W. Mu, N. Dogan,Metall. Mater. Trans. B Process Metall. Mater. Process. Sci. 2018, 49, 1612 .

[58] Z.S. Ren, X.J. Hu, X.M. Hou, X.X. Xue, K.C. Chou,Int. J. Miner. Metall. Mater. 2014, 21, 345 .

[59] B. Morosin, R.W. Lynch,Acta Crystallogr. Sect. B Struct. Crystallogr. Cryst. Chem. 1972, 28, 1040 .

[60] T.N. Roman, C. New,Materials Science and Engineering Materials Science and Engineering, vol. 232, 3rd edn., CRC Press, 2010.

[61] VirtualDub, version 1.10.4, developed by A. Lee and available on theinternet at IR http://www.virtualdub.org/, accessed: May2018.

[62] K. Hatta, M. Higuchi, J. Takahashi, K. Kodaira,J. Cryst. Growth 1996, 163, 279 .

[63] C. Ariyo, P. Gonzalez, L. Holappa,Steel Res. Int. 2005, 4, 284 .

[64] H. jurgen Seifert, F. Aldinger,Zeitschrift für Met. 1996, 87, 841 .

[65] D.W.T. Rippin,Chemical Reaction Engineering, vol. 19, Third., John Wiley and Sons, 1964.

[66] M. Sharma, W. Mu, N. Dogan,in AISTech 2018, 2018, 2601.

[67] D. Croker, M. Loan, B.K. Hodnett,Cryst. Growth Des. 2009, 9, 2207 .

[68] A. de Pretis, F. Ricciardiello, O. Sbaizero,J. Mater. Sci. Lett. 1985, 4, 9 .

[69] P. Yan, B.A. Webler, P.C. Pistorius, R.J. Fruehan,Metall. Mater. Trans. B 2015, 46, 2414 .

Chapter 4

In situ observation of dissolution of oxide inclusions in steelmaking slags

Submerged entry nozzles used for casting of automotive-grade steel such as titanium alloyed interstitial free steel and titanium stabilized ultra-low carbon steel often face the challenge of clogging. Alumina, spinel, and Al-Ti-O type inclusions are detected in the clogged mass of these nozzles. While there is some literature on the dissolution kinetics of alumina and spinel inclusions, to the best knowledge of the author, there is no literature on the dissolution kinetics of Al-Ti-O type inclusions. This chapter presents novel results on the dissolution kinetics of Al_2TiO_5 type inclusions in two CaO-SiO_2-Al_2O_3 type slags at 1550 °C. Kinetic data of these particles are compared with those of Al_2O_3 particles. The gas evolution was only observed during in situ dissolution of Al_2TiO_5 particles. Analysis of the CSLM data using the shrinking core model shows that the diffusivity of alumina estimated from the Al_2TiO_5 dissolution data was approximately two orders of magnitude higher than expected diffusivity.

Chapter 4 is the pre-publication version of the article published in *The Journal of The Minerals, Metals & Materials Society (TMS)*. Volume 70: Issue 7. https://doi.org/10.1007/s11837-018-2908-y. The publishers had placed restrictions on the size of the paper. Thus, we had to adjust some information in the form of supplementary material. The figures and tables presented as supplementary data is provided after the reference sections of this chapter.

The dissolution experiments and measurements were carried out by the primary author. The discussions on data analysis were shared between the primary author and Dr. Dogan. Dr. Mu helped the establishment of the experimental technique and reviewed the final version of the manuscript.

In situ observation of dissolution of oxide inclusions in steelmaking slags

Mukesh Sharma[1], Wangzhong Mu[2], Neslihan Dogan[1]

[1]McMaster University,
1280 Main Street West, Ontario, Canada, L8S4L7

[2] KTH Royal Institute of Technology,
Brinellvägen 23, Stockholm, Sweden, SE-10044

Abstract

Better understanding of removal of non-metallic inclusions is of importance in the steelmaking process to control the cleanliness of the steel. In this study, the dissolution rate of Al_2O_3 and Al_2TiO_5 inclusions in a liquid $CaO–SiO_2–Al_2O_3$ slag was measured using high temperature confocal scanning laser microscope (HT-CSLM) at 1550°C. The dissolution rate of inclusions is expressed as a function of the rate of decrease of the radius of solid particles with time. It is found that Al_2O_3 inclusions have a slower dissolution rate than that of Al_2TiO_5 inclusions at 1550°C. The rate controlling steps are investigated in terms of a shrinking core model. It is shown that the rate controlling step for dissolution of both inclusion types is mass transfer in the slag at 1550°C.

4.1 Introduction

Titanium addition is crucial during secondary steelmaking, especially for producing automotive grade titanium stabilized ultra-low carbon steel (Ti-SULC) and interstitial free (IF) steel. The presence of titanium improves the mechanical property of steels [1], however it also leads to the formation of complex Al-Ti-O inclusions [2]. These inclusions are often reported in the clog deposits collected from the submerged entry nozzle, thus the frequency of nozzle clogging affects the productivity of the steelmaking process significantly [2–4]. Basu et al. [2] reported an extensive melt freezing inside the nozzle deposits in the case of Ti alloyed IF steel in comparison to Ti free IF steel. This is most likely related to the fact that the wettability of Al-Ti-O inclusions is higher than that of Al2O3 inclusions by Fe-C melts [5]. The removal of these inclusions by dissolving them into slag during steel refining or at the tundish and mold can improve the process efficiency.

The removal of inclusions by dissolution in slag is experimentally studied by either the dip test or the high temperature confocal scanning laser microscope (HT-CSLM). In the dip test, a centimeter-size refractory rod is immersed in a slag for a period of time, removed and then analyzed for slag corrosion and/or penetration. Wang et al. [6] studied the dissolution of Al_2TiO_5 rod into a 15%Al_2O_3-35%CaO-50%SiO_2 slag at 1550°C using dip test. After dipping rod into the slag for 0, 10, 30 and 60 s, the rod samples were prepared to study the chemical composition of the interface between the rod and the slag using scanning electron microscope with energy dispersive X-ray spectrometry (SEM-EDXS). They observed that the width of dissolution boundary changed with reaction time and reported that Al_2TiO_5 dissolution and slag penetration take place simultaneously. The dissolution rate of Al_2TiO_5 is initially faster than the rate of diffusion of liquid product towards the bulk slag, and the two rates become equal later. However, the study does not report the dissolution kinetics of Al_2TiO_5 or dissolution path from the beginning to the end of its dissolution process. Ren et al. [7] studied the dissolution mechanism of TiO_2 in three slag compositions with basicity of 0.8-1.2 at temperatures of 1370 °C, 1400 °C and 1430 °C. They observed that the dissolution of TiO_2 occurs in three stages: (i) erosion of TiO_2 towards the bulk slag, (ii) dissolution of the eroded TiO_2 in the bulk slag, where the region of dissolution is termed as dissolution layer, (iii) and the precipitation of $CaTiO_3$ in the dissolution region due to high local concentration of TiO_2, and diffusion of Ti^{4+} ion from the dissolution region towards the bulk slag. The region in third stage from where diffusion of Ti^{4+} occurs is referred as a diffusion layer. They reported that the dissolution-diffusion layer width first increases and then decreases as basicity increases from 0.8 to 1 to 1.2.

The HT-CSLM technique allows for the continuous in-situ observation of micron-size particles behavior in real time. Several researchers [8–12] have applied this technique to study the dissolution behavior of a single oxide particle in slag. Majority of these studies [8, 10, 12–17] used the inclusion types that are available for purchase. The unavailability of certain inclusion types limits the assessment and testing of key inclusion groups important in steelmaking. Thus, a key knowledge gap exists in the understanding of dissolution of Ti-containing oxides into steelmaking slags.

The present work focusses on the in-situ observation for dissolution of Al_2TiO_5 and Al_2O_3 particles in slag relevant to steelmaking conditions. The dissolution experiments were carried out using the HT-CSLM at 1550°C. The Al_2TiO_5 particles were prepared by the optical floating zone method (OFZM) [18]. This technique was applied to produce dense and pure oxide particles for observation of inclusion dissolution. The kinetic study focusing on dissolution rate of Al_2O_3 and Al_2TiO_5 particles is discussed in this work.

4.2 Experimental methodology

A. Inclusion particle preparation

The reagent grade (99.5%) mixture of TiO_2 and Al_2O_3 was purchased from Alfa Aesar, USA. The powder mixture was first compressed to a rod. The rod was further pressed under a pressure of 1 atm for 5 minutes and dried at 900°C. This rod was fed as seed and feed rods in the floating zone furnace. These rods were met and melt at elevated temperatures to produce a poly-crystal of Al2TiO5. Before and after melting, the samples were analyzed by X-ray diffraction (XRD) technique and the Al_2TiO_5 content in the crystal is approximately 100%. The rod of Al_2TiO_5 was crushed into the particles of about 200-500 μm for dissolution experiments. The reagent grade (99.99%) Al_2O_3 particles (sapphire) were purchased from Noah Technologies Corporation, USA; and these particles were directly used for dissolution experiments.

B. Slag preparation

To prepare the slag, the high purity laboratory grade $CaCO_3$, SiO_2 and Al_2O_3 purchased from Sigma Aldrich were used. The selected slag composition is 23.2 Al_2O_3, 30.5 CaO and 46.3 SiO_2, all in wt%. The constituent powders in appropriate stoichiometry proportions were initially mixed and then heated to a temperature, 50°C higher than the slag liquidus temperature, to fully melt in a platinum crucible. After homogenization of molten slag, slags were quenched and crushed. The slag composition was confirmed by the inductively coupled plasma optical emission spectroscopy (ICP-OES). The slag liquidus temperature is estimated using FactSage 7.1^{TM} Equilib program and equals 1442°C. The slag viscosity is 62 poise as determined using Urbain's model [19]. The density of slag is 2705 kg/m^3 as calculated from model provided in Slag Atlas [19]. The density of Al_2TiO_5 particle is measured using a 2ml capacity pycnometer at room temperature and then extrapolated to higher temperature values using the coefficient of expansion obtained from literature [20]. The measured densities of Al_2O_3 and Al_2TiO_5 particles are 3810 and 3804 kg/m^3, respectively.

C. Dissolution experiments and observations

The experiments for the dissolution of Al_2TiO_5 and Al_2O_3 particles in slag are conducted using a Lasertec VL2000DX-SVF17SP unit which consists of a HT-CSLM mounted on top of a gold coated infrared image furnace (IIF). The position of the particle and slag inside the IIF is shown in supplementary Figure 4-4(a). A single Al_2TiO_5 or Al_2O_3 particle is placed on top of the slag. The slag was pre-melted in a platinum crucible which was placed inside an alumina crucible.

The particle and slag, sample holder and crucible were heated to the experimental temperature under 99.999% argon atmosphere at a flowrate of 200 ml/min. See, supplementary Figure 4-4(b) for the predetermined heating and cooling schedule used for current work. The system was initially heated from 150°C to 1450°C at a rate of 1000°C/min followed by heating at 1550°C at the rate of 100°C/min. It was held at 1550°C during the dissolution process and cooled to room temperature. A relative faster heating rate of 1000°C/min was used to minimize any dissolution of particle which might happen before reaching 1550°C.

4.3 Results and discussion

4.3.1 In situ observations of particle dissolution

For the kinetic measurements, time zero is chosen when the set temperature reaches the experimental temperature and the particle is completely covered by the slag. The phase boundary between the particle and slag is manually drawn and illustrated by a yelow line, see supplementary Figure 4-5 and Figure 4-6. Interestingly, the hue of the Al_2TiO_5 particle changes from opaque to transparent gradually as the dissolution proceeds. It is well known that the presence of Ti^{3+} is the origin in coloring of rutile crystals [21] Therefore, the change in color of Al_2TiO_5 might indicate a change in the amount of Ti^{3+} in the particle due to dissociation of stoichiometric Al_2TiO_5 to a reduced form of aluminum titanate, alumina and oxygen as shown by reaction 4-1 [22]. This however must be confirmed and at this point of time remains as future work for this research. It is important to note that there was no significant rotation of the Al_2TiO_5 particle observed during each experiment. This phenomenon is not observed during the dissolution of Al_2O_3 particle (see supplementary Figure 4-6).

$$(3-2z)[(Al^{+3})_2(Ti^{+4})_1(O^{-2})_5] = \left(Al_z{}^{+3}Ti_{1-z}\right)_2(Ti^{+4})_1(O^{-2})_5 + 3(1-z)Al_2O_3 + \frac{1}{2}(1-z)O_2 \tag{4-1}$$

4.3.2 Dissolution rate

The videos captured by HT-CSLM are saved and converted into pictures using open source software, VirtualDub developed by Avery Lee [23]. These pictures are further analyzed using a public domain image processing program ImageJ^{TM}. The dissolution is measured in terms of changes in particle area with time. In this study, it is assumed that the particle has a spherical shape. Therefore, the equivalent radius of a circle can be calculated from the measured particle area. Figure 4-1 compares the results for dissolution of Al_2O_3 and Al_2TiO_5 particles into the same molten slag. Total dissolution time of an Al_2TiO_5 particle is approximately 30 seconds for an equivalent circular diameter of 400 µm while it is 500 seconds for an Al_2O_3 particle with a diameter of 320 µm. Even though initial particle size is different, it can be concluded that the dissolution of an Al_2TiO_5 particle is faster than that of Al_2O_3 particles in the slag studied. It is also found that the radius of the particles decreases almost linearly in the early stage of the dissolution process and significantly increases towards the end of the dissolution.

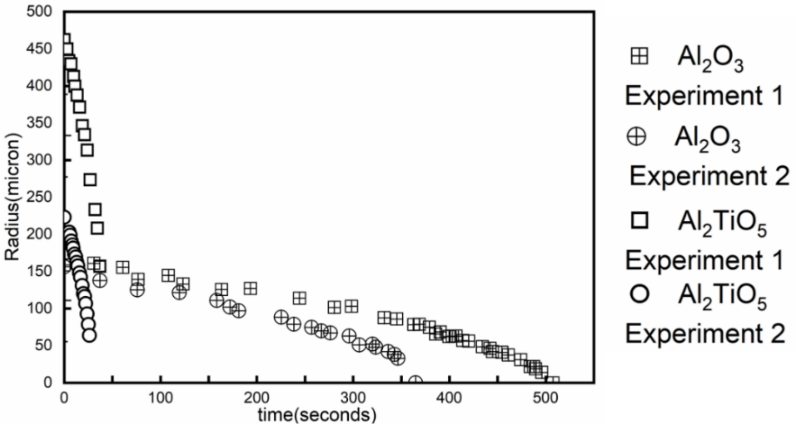

Figure 4-1 Change in Al_2O_3 and Al_2TiO_5 particle size with time, hollow markers represent equivalent circular radius measured from frames obtained from CSLM video at different time steps during dissolution.

4.3.3 Rate controlling mechanism

To identify the process variables that affect the dissolution rate of Al_2O_3 and Al_2TiO_5 particles in the slag, the shrinking core model (SCM) for spherical particle with shrinking size are used [24]. If steady state diffusion prevails, this might suggest towards a chemical reaction control, represented by equation 4-2 or mass transfer in Stoke's regime, represented by equation 4-3.

$$\frac{R_C}{R_0} - 1 = \frac{bK_R\Delta C}{\rho_{particle}R_0}t \tag{4-2}$$

$$\left(\frac{R_C}{R_0}\right)^2 - 1 = \frac{2b\Delta CD}{\rho_{particle}R_0^2}t \tag{4-3}$$

where R_c and R_0 are the initial and instantaneous radius, respectively, in meter, t is instantaneous time in s, $\rho_{particle}$ is the density of particle in kg/m^3, b is the stoichiometric constant and equals to 1. ΔC is the difference in concentration of the rate controlling species in bulk slag and slag at saturation in kg/m^3, $K_R$is the first order rate constant for the surface reaction in m/s, and D is the diffusivity of the species in consideration in m^2/s.

For a comparison of the Al_2O_3 and Al_2TiO_5 dissolution data with the SCM for chemical reaction control and mass transfer control in Stoke's regime, see supplementary Figure 4-8. Dissolution curves for both particles are generally in good agreement with the mass transfer control model. Only one curve lies in between the chemical reaction control and mass transfer control in Stoke's regime.

For dissolution of Al_2O_3 and Al_2TiO_5 particles, the chemical reaction control and mass transfer control curves are further analyzed with respect to the regression values obtained by fitting curves from the SCM. This approach is adapted from the study by Monaghan and Chen [25]. Following equation 4-2, if a straight line passing through the origin is drawn with $\frac{R_C}{R_0} - 1$ on Y axis and t on X axis, the slope can be used to estimate the rate constant KR. Similarly, following equation 4-3, a straight line passing through the origin is drawn with $\left(\frac{R_C}{R_0}\right)^2 - 1$ on Y axis and t on X axis, the slope can be used to estimate the diffusivity D of the particle. A regression fit is made against the experimental data to obtain the degree of fit parameter, R^2 for the corresponding experiments for Al_2O_3 and Al_2TiO_5 dissolution.

The experimental data in Figure 4-1 is replotted in Figure 4-2 and Figure 4-3 for chemical reaction control and mass transfer control for Al_2O_3 and Al_2TiO_5 particles. Figure 4-3 shows that the R^2 values for chemical reaction control for experiment 1 and experiment 2 are 0.93 and 0.95, respectively for Al_2O_3 whereas they are 0.94 and 0.96 for Al_2TiO_5 particles. These values are slightly lower than those for mass transfer control (0.99 and 0.95 for Al_2O_3 particles and 1.0 for Al_2TiO_5 particles). Furthermore, the R^2 values for mass transfer control indicate an excellent fit with the experimental data. These results indicate that mass transfer in slag phase is most likely the rate controlling step for dissolution of Al_2O_3 and Al_2TiO_5 particles in the slag studied.

The R^2 values listed in supplementary Table 4-1 are obtained from the regression fit of the curves to the experimental data for Al_2O_3 and Al_2TiO_5 particles with mass transfer control in Stoke's regime model. To calculate the diffusivity values, the saturated slag composition as well as concentration difference of rate controlling species are predicted using FactSage 7.1^{TM} thermochemical software. In the present study, the rate controlling species is assumed to be aluminum-oxygen complex anion for dissolution of Al_2O_3 particles as suggested by previous studies [25]. For dissolution of Al_2TiO_5 particles, aluminum-oxygen complex anion as well as titanium cation are assumed to be possible rate controlling species.

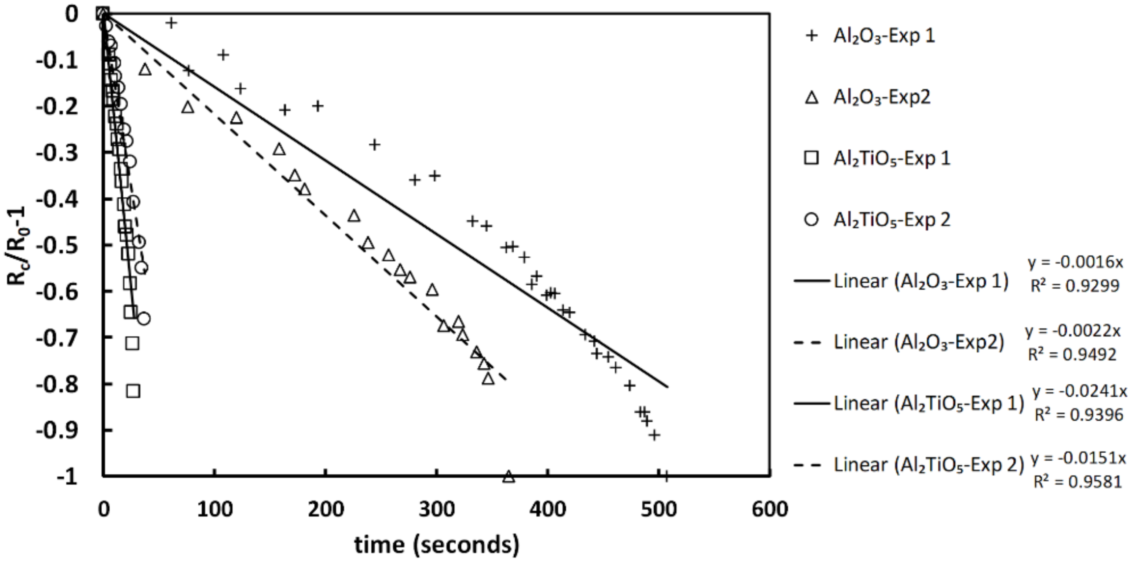

Figure 4-2 Comparison of Al_2O_3 and Al_2TiO_5 dissolution data in slag with SCM assuming chemical reaction control, hollow markers indicate data points and solid lines represent regression fit to data.

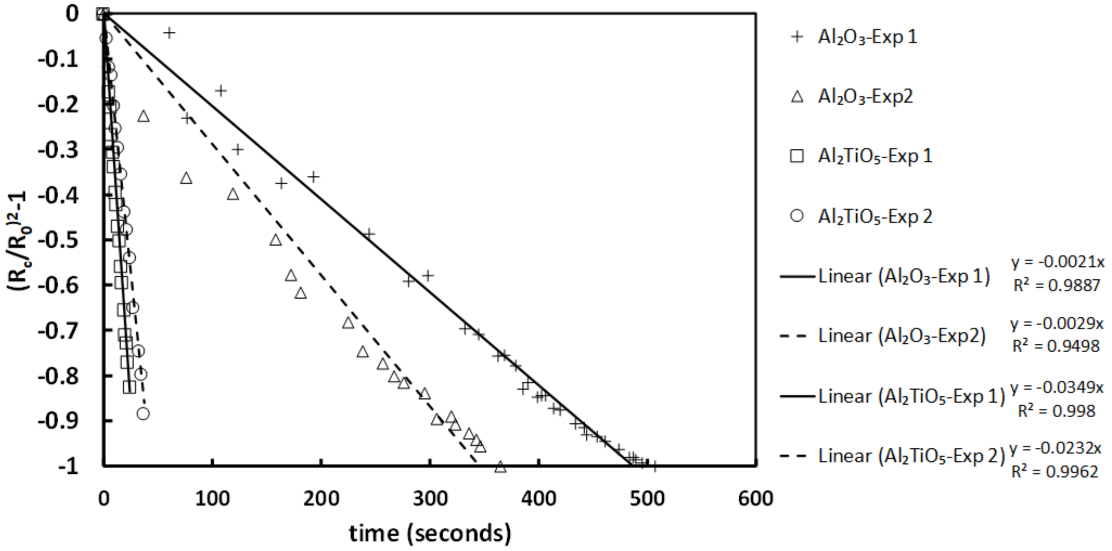

Figure 4-3 Comparison of Al_2O_3 and Al_2TiO_5 dissolution data in slag with SCM assuming mass transfer control in Stoke's regime, hollow markers indicate data points and solid lines represent regression fit to data.

For simplicity, AlO_x^{y-} and Ti^{4+} are referred as Al_2O_3 and TiO_2, respectively in the following text. At the interface of slag and Al_2O_3 particles, ΔC^{Al2O3} equals 593 kg/m3 whereas this value equals 284 kg/m^3 at the interface of slag-Al_2TiO_5 particle. ΔC^{TiO2} equals 265 kg/m3 at the interface of slag-Al_2TiO_5 particle. The diffusivity values of Al_2O_3 and TiO_2 are calculated and summarized in supplementary Table 4-1.

The measured diffusivity value of Al_2O_3 in slag varied from 10^{-10} to 10^{-8} m^2/s at 1550°C. The values obtained for Al_2O_3 particles are in agreement with reported data in the literature [15, 26–28], however the values for Al_2TiO_5 particles are significantly higher than that for Al_2O_3 particles. To the best of authors' knowledge, there is no comparable diffusivity values available for Al_2TiO_5 particle dissolution into slags relevant to steelmaking conditions. One can consider that this difference is likely to be related to the regression analysis made. Moreover, the authors are not able to make a statement of rate controlling species for the system studied. Further analysis and characterization of particle/slag interface will be conducted to confirm the rate controlling species.

4.4 Conclusions

The in-situ dissolution of Al_2O_3 and Al_2TiO_5 particles is studied in the steelmaking type slag at 1550°C using a high temperature confocal scanning laser microscope. The following conclusions can be drawn from the present study:

1. This study offers novel data on dissolution of Al_2TiO_5 inclusions in the steelmaking slags observed in-situ by HT-CSLM, which has not been reported in open literature. The new data generated will have an important bearing on future steel processing and will enable further research.
2. The dissolution rate of Al_2TiO_5 particles is much faster than that of Al_2O_3 particles and the dissolution time is approximately 500 and 30 seconds for Al_2O_3 and Al_2TiO_5 particles with a similar radius of 150 to 200 µm.
3. The in-situ observations of particle dissolution and a comparison of the dissolution data with the shrinking core model shows that mass transfer control in Stoke's regime is likely to be the rate controlling mechanism for both inclusion types at 1550°C. From the kinetic analysis, determination of rate controlling species remains a question at the current stage and further studies are required to establish this.

4.5 Acknowledgment

The authors would like to thank the Natural Sciences and Engineering Research Council (Project No. 20000514) and Canada Foundation for Innovation John Evans Leaders Fund (CFI JELF, Project No. 32826).

4.6 References

1. H. po WANG, L. feng SUN, B. PENG, and M. fa JIANG, J. Iron Steel Res. Int. 20, 70 (2013).

2. S. Basu, S. K. Choudhary, and N. U. Girase, ISIJ Int. 44, 1653 (2004).

3. P. Kaushik, R. Lule, G. Castillo, F. Lopez, C. Perim, G. Pigatti, B. Henriques, F.

Barbosa, A. Nascimento, E. Chicago, A. L. Cardenas, L. Cardenas, A. Tubarao, and J. Limoeiro, in Aistech (2015), pp. 3279–3295.

4. P. Kaushik, J. Lehmann, and M. Nadif, Metall. Mater. Trans. B Process Metall. Mater. Process. Sci. 43, 710 (2012).

5. A. Karasangabo and C. Bernhard, J. Adhes. Sci. Technol. 26, 1141 (2012).

6. D. Wang, J. Liu, M. Jiang, F. Tsukihashi, and H. Matsuura, Int. J. Miner. Metall. Mater. 18, 646 (2011).

7. Z. Ren, X. Hu, X. Hou, X. Xue, and K. Chou, Int. J. Miner. Metall. Mater. 21, 345 (2014).

8. S. Feichtinger, S. K. Michelic, Y.-B. Kang, and C. Bernhard, J. Am. Ceram. Soc. 97, 316 (2014).

9. A. B. Fox, M. E. Valdez, J. Gisby, R. C. Atwood, P. D. Lee, and S. Sridhar, ISIJ Int. 44, 836 (2004).

10. S. Sridhar and A. W. Cramb, Metall. Mater. Trans. B 31, 406 (2000).

11. J. H. Park, J. G. Park, D. J. Min, Y. E. Lee, and Y. B. Kang, J. Eur. Ceram. Soc. 30, 3181 (2010).

12. X. Guo, M. Guo, Z. Sun, J. Van Dyck, B. Blanpain, and P. Wollants, in Mater. Sci. Technol. Conf. (2010), pp. 1739–1750.

13. S. A. Nightingale, G. A. Brooks, and B. J. Monaghan, Metall. Mater. Trans. B 36,

453 (2005).

14. S. H. Lee, C. Tse, K. W. Yi, P. Misra, V. Chevrier, C. Orrling, S. Sridhar, and a. W. Cramb, J. Non. Cryst. Solids 282, 41 (2001).

15. J. Liu, F. Verhaeghe, M. Guo, B. Blanpain, and P. Wollants, J. Am. Ceram. Soc. 90, 3818 (2007).

16. J.-H. Park, I.-H. Jung, and H.-G. Lee, ISIJ Int. 46, 1 (2006).

17. S. Michelic, J. Goriupp, S. Feichtinger, Y.-B. Kang, C. Bernhard, and J. Schenk, Steel Res. Int. 86, 1 (2015).

18. H. A. Dabkowska and A. B. Dabkowski, in Springer Handb. Cryst. Growth, edited by G. Dhanaraj, K. Byrappa, V. Prasad, and M. Dudley (Springer Berlin Heidelberg, Berlin, Heidelberg, 2010), pp. 367–391.

19. B. J. Keene, K. C. Mills, and M. Susa, Slag Atlas (Verlag Stahleisen mbH, 1995).

20. J. F. Shackelford and W. Alexander, Materials Science and Engineering Handbook (2001).

21. K. Hatta, M. Higuchi, J. Takahashi, and K. Kodaira, J. Cryst. Growth 163, 279 (1996).

22. H. jurgen Seifert and F. Aldinger, Zeitschrift Für Met. 87, 841 (1996).

23. Virtual Dub, version 1.10.4, developed by A. Lee and available on the internet at IR http://www.virtualdub.org/, accessed: May2018

24. O. Levenspiel, Chemical Reaction Engineering, Third (John Wiley and Sons, 1999).

25. B. J. Monaghan and L. Chen, Ironmaking Steelmaking. 33, 323 (2006).

26. C. Orrling, S. Sridhar, and A. W. Cramb, ISIJ Int. 40, 877 (2000).

27. M. Valdez, K. Prapakorn, A. W. Cramb, and S. Sridhar, Ironmaking Steelmaking. 29, 47 (2002).

28. B. J. Monaghan and L. Chen, Steel Res. Int. 76, 346 (2005).

Supplementary Material for Chapter 4

In Situ Observation of Dissolution of Oxide Inclusions in Steelmaking Slags

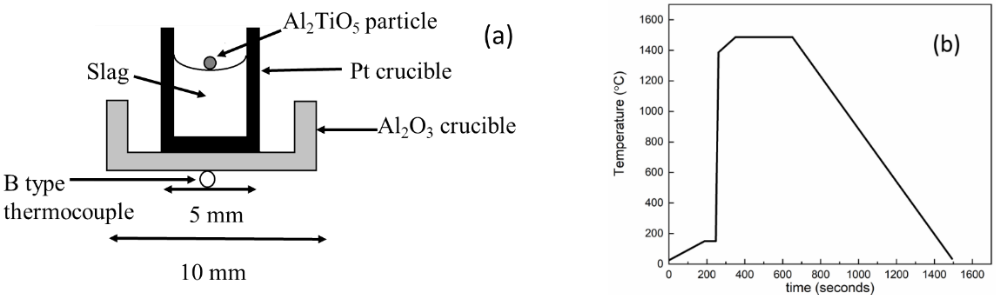

Figure 4-4 A schematic of (a) placement of particle and slag inside the infrared image furnace in a HT-CSLM and (b) heating and cooling profile used for inclusion dissolution experiments

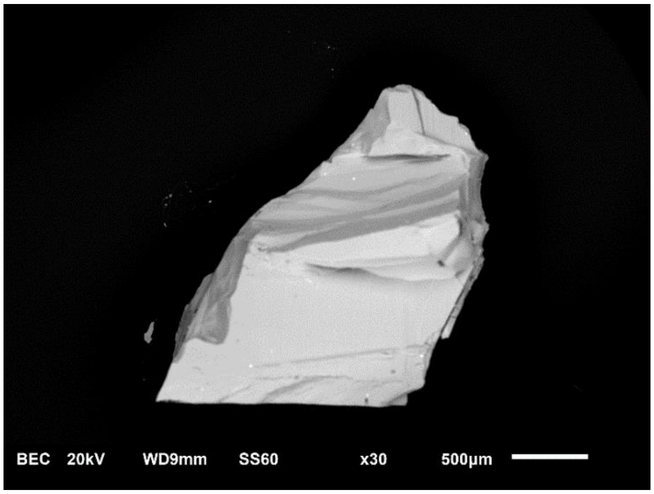

Figure 4-5 Back scattered electron image of an Al_2TiO_5 particle before experiment

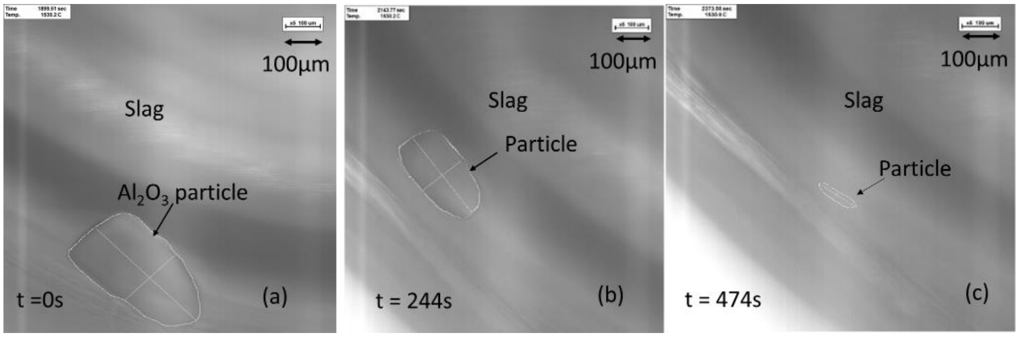

Figure 4-6 Dissolution of Al_2O_3 in slag (a) at time zero, (b) after 244 seconds and, (c) towards the end of dissolution

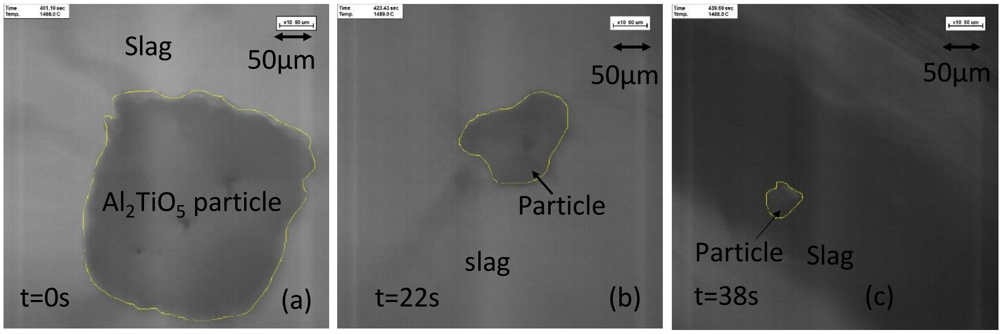

Figure 4-7 Dissolution of Al_2TiO_5 in slag (a) at time zero, (b) after 22 seconds and (c) towards the end of dissolution

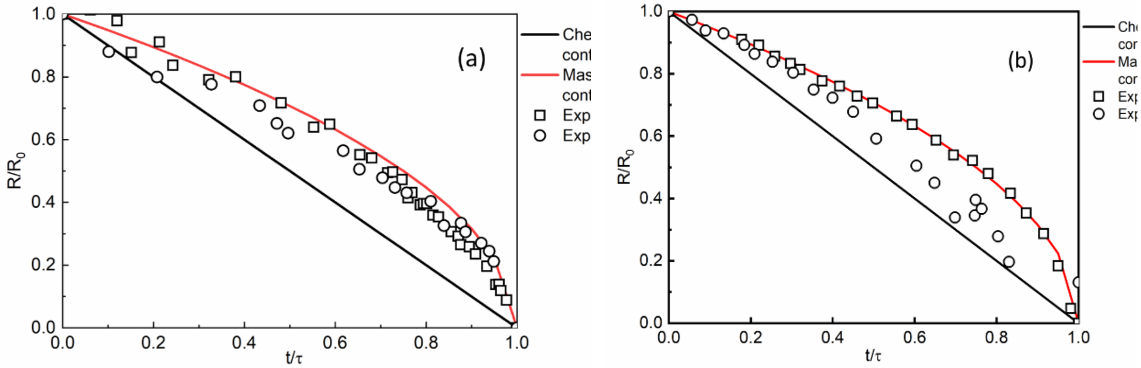

Figure 4-8 Comparison of HT-CSLM data for (a) Al_2O_3 and (b) Al_2TiO_5 dissolution with shrinking core models

Table 4-1 Estimated diffusivity values considering Al_2O_3 and TiO_2 as transported species in comparison with mass transfer control model

Slag/condition	**Slope of $(R/R_0)^2-1$ vs t, s^{-1}**	**R^2**	**D^{Al2O3} (m^2/s)**	**D^{TiO2} (m^2/s)**
Al_2O_3	-2.05×10^{-3}	1.0	1.7×10^{-10}	--
Al_2O_3	-2.89×10^{-3}	0.99	2.3×10^{-10}	--
Al_2TiO_5	-35.0×10^{-3}	1.0	95×10^{-10}	110×10^{-10}
Al_2TiO_5	-23.2×10^{-3}	1.0	270×10^{-10}	310×10^{-10}

Chapter 5

Dissolution behavior of aluminum titanate inclusions in slag

This chapter presents novel data on the investigation of the particle-slag interface at different stages of dissolution of an aluminum titanate particle to determine the mechanism and path of dissolution of such inclusion types. To study this phenomenon, a single particle of aluminum titanate is dissolved in slag at 1500 °C. The particle-slag system is rapidly quenched using helium at different stages of dissolution. The quenched samples are examined for distribution of the constituent elements; Al, Ti, Ca, and Si using the scanning electron microscope (SEM). Phases such as alumina, titanium-rich slag, and calcium titanate are detected at the particle slag interface.

It was found that there was no gradient in the bulk slag or within the particle. This absence of gradient rules out the theory of mass transfer in bulk slag or diffusion control within the particle. A gradient was always observed at the interface, which presents evidence for mass transfer at the boundary layer to be rate-controlling step. Other than that, alumina and calcium titanate phases are always detected at the interface. The calcium titanate is present in the form of dendrites and thus appears to be a solidification product. The dissolution path of Al_2TiO_5 particle in slag is proposed. The Al_2TiO_5 dissociates into alumina and titanium oxide. The alumina and titanium oxide dissolve in the bulk slag while oxygen is evolved as seen during in situ dissolution. The oxygen evolved during dissolution enhances the mass transfer coefficient of Al_2TiO_5, thus showing higher diffusivity than the anticipated value.

The experimental kinetic data was collected by the primary author. Analysis of the data was shared between the primary author and Dr. Dogan. The manuscript was drafted by the primary author and reviewed the final version by Dr. Dogan**.** This chapter was submitted to the Metallurgical and Materials Transactions B for publication on 4th May 2019 and currently under revision.

Dissolution behavior of aluminum titanate inclusions in steelmaking slags

Mukesh Sharma, Neslihan Dogan

Department of Materials Science and Engineering, Faculty of Engineering, McMaster University, 1280 Main Street West, Hamilton, ON L8S4L7, Canada.

Abstract

The current work investigates the dissolution path and mechanism of aluminum titanate inclusions in steelmaking slags using a high-temperature confocal scanning laser microscope (CSLM). To study this phenomenon, a single particle of aluminum titanate is dissolved in slag at 1773 K. During the dissolution process; gas bubbles are evolved. Further, the particle-slag system is rapidly quenched using helium at different stages of dissolution. The quenched samples are examined for distribution of the constituent elements; Al, Ti, Ca, and Si using the scanning electron microscope (SEM). Phases such as alumina, titanium-rich slag, and calcium titanate are detected at the particle slag interface. The dissolution path of aluminum titanate is proposed in the following steps. First, aluminum titanate dissociates into alumina, titanium oxide and oxygen while slag penetrates through the particle. In the next step, the alumina and titanium oxide dissolves in slag, and the oxygen leaves the system. The existence of gas bubbles enhances the overall rate of Al_2TiO_5 dissolution. The dissolution of Al_2TiO_5 appears to be controlled by mass transfer in the slag. Evidence in support of this finding is the particle-slag interface characterization by line scan analysis and calculated diffusivity values being inversely proportional to the viscosity of slag.

5.1 Introduction

Titanium is added to ultra-low carbon steel to improve the fracture toughness. Titanium (Ti) reacts with carbon and nitrogen to form TiC, TiN, and Ti (C, N) which are present at the grain boundaries. These carbides prevent the motion of the grains during steel processing [1,2]. Although Ti is beneficial in providing enhanced thermomechanical properties, its addition to liquid steel causes upstream processing problems [3–12]. Ti bearing molten steel flows from the tundish to the mold through a submerged entry nozzle (SEN). The inconsistent flow of molten steel through the SEN may occur because of clog building up near the exit ports [10] and the upper tundish nozzle [13].

Kaushik et al. [14] and Basu et al. [10] investigated casting productivity problems and suggested solutions to improve the castability of TiSULC (titanium stabilized ultra-low carbon steel) and IF (interstitial free) grade steels, respectively. Analyses of cross-sections of clogged nozzles used for producing IF and TiSULC steel grades show the presence of Al_2O_3 and Al-Ti-O type inclusions [10,14,15]. Basu et al. [10] found that aluminum titanate type inclusions are typically reoxidation products. These inclusions are formed when Ti containing molten steel comes in contact with reducible oxides such as SiO_2, present in various refractory materials, ladle slag or tundish slag, expressed in reaction 5-1[10].

$$\frac{6+x}{2}(\mathrm{SiO_2}) + 4\underline{\mathrm{Al}} + \underline{\mathrm{Ti}} \rightarrow \frac{6+x}{2}\underline{\mathrm{Si}} + (\mathrm{Al_2O_3})_{\mathrm{precipitate}} + (\mathrm{TiO_x} - \mathrm{Al_2O_3})_{\mathrm{precipitate}} \tag{5-1}$$

The species in a round bracket in the equation represent species in slag while species with an underline represent those dissolved in steel. From reaction 5-1, the dissolved Ti in the steel reacts with oxygen supplied by SiO_2 to form the TiO_x-Al_2O_3 complex.

Al_2O_3 inclusions are generally formed during the deoxidation of steel. These alumina inclusions adhere to the wall of the ceramic nozzles and agglomerate to form clusters. The TiO_x-Al_2O_3 type inclusions formed by reoxidation are present alongside Al_2O_3 inclusions in the clusters. It is challenging to separate liquid steel from TiO_x-Al_2O_3 inclusions because of the high wetting of such inclusion types by steel [16]. The presence of such inclusion types in steel aggravates melt freezing in clogs. An industrial study by Basu et al. shows that the casting of steel with Ti displayed aggravated clogging of ceramic nozzles in comparison to the casting of Ti free steel [10]. To reduce the clogging problem, Al-Ti-O type inclusions should be prevented from sticking to the wall by using nozzle well packing material or internal lining of submerged entry nozzle [10]. Alternatively, they can be modified by forming a liquid phase [17][9] or removed by dissolution in top slag [14].

Limited studies exist regarding the dissolution of Ti containing inclusions such as titanium oxide and aluminum titanate type inclusions in slag [17,18]. Ren et al. [18] reported the dissolution mechanism of TiO_2 in three slag compositions with basicity of 0.8-1.2 at temperatures of 1643 K, 1643 K, 1673 K, and 1703 K. From the study, they found that the dissolution of TiO_2 proceeds in three distinct steps: (1) dissolution of Ti^{4+} ions into the bulk slag, (2) accumulation of Ti^{4+} ions in a boundary layer adjacent to the TiO_2 substrate and (3) the precipitation of $CaTiO_3$ at the boundary layer due to high local concentration of TiO_2. The formation of $CaTiO_3$ in the third step slows down the diffusion of Ti^{4+} ion to the bulk slag. Thus, the diffusion of Ti^{4+} ions from the boundary layer to bulk slag was assessed as the rate-controlling step. However, other possible rate-controlling steps such as boundary layer diffusion or rate of $CaTiO_3$ formation were not investigated.

Wang et al. [17] studied the dissolution of Al_2TiO_5 substrate in a 35 pct CaO-50 pct SiO_2- 15 pct Al_2O_3 slag at 1823 K using dip test. The Al_2TiO_5 rod was submerged into the slag and quenched under argon atmosphere after 0, 10, 30 and 60 seconds of dissolution. The interface of the quenched rod-slag system was polished and studied using SEM. They found that Al_2TiO_5 dissolution and slag penetration occurred simultaneously at the substrate/slag interface. They proposed the following mechanism for Al_2TiO_5 dissolution: (1) a liquid product appears on the surface of the Al_2TiO_5 substrate and (2) the liquid product diffuses towards the bulk slag. The work by Wang et al. [17] provided insight into understanding the dissolution mechanism of Al_2TiO_5. However, in their work, the Al_2TiO_5 rod they prepared by sintering was 90 pct pure. Other phases such as unreacted Al_2O_3, TiO_2 might interfere with the SEM/EDX results. Even though the line scan at the Al_2TiO_5 rod/slag interface from SEM results formed the primary basis of identifying the mechanism, the study does not provide a discussion on the rate-controlling step.

In a previous work by the authors [19], the dissolution kinetics of aluminum titanate inclusion in the slag was reported. The authors studied the in -situ dissolution of a single Al_2TiO_5 particle in slag at 1550 °C using a high-temperature confocal scanning laser microscope (CSLM). A comparison of the CSLM data with the shrinking core model (SCM) showed that it is difficult to differentiate between mass transfer control and chemical reaction control in order to determine the dissolution mechanism. The in-situ observation of gas bubble generation on the surface of the particle during dissolution needed further investigation. The bursting of gas bubbles during dissolution enhanced localized mass transport. However, this phenomenon was not incorporated into the mass transfer control model, which was used to analyze the CSLM data.

The current work presents novel data on the dissolution kinetics of Al_2TiO_5 inclusions in steelmaking slag at 1773 K. This study aims at finding the dissolution rate and establishing the dissolution mechanism of Al_2TiO_5 particles in CaO-SiO_2-Al_2O_3 type slag at steelmaking temperatures. Two methods are employed to study the dissolution mechanism. The first method investigates the composition profile of constituent elements at the slag particle interface at different stages of dissolution using SEM/EDX. The second method is to compare the CSLM data with the SCM. Regression analysis is performed to differentiate between the chemical reaction control and mass transfer control. Besides, the mystery of the gas bubble evolving, and bursting observed during in – situ dissolution of Al_2TiO_5 particle is addressed.

5.2 Experimental Methodology

To avoid the problem with substrate purity, the authors prepared pure and dense Al_2TiO_5 particles by the optical floating zone technique. The details of the inclusion preparation technique by the optical floating zone method and slag preparation are published in a separate study [20] by the authors. The chemical composition, density, and viscosity of the prepared slag and particle are summarized in Table 5-1. The chemical composition of the slag was determined by the inductively coupled plasma (ICP) analysis. The slag liquidus temperature was obtained from FactSage 7.2^{TM} using the Equilib module and the FToxid database. The density of the slag was estimated using the slag density model presented in the Slag Atlas [21]. The viscosity of the slag was calculated using the Urbain model [22]. The density of the Al_2TiO_5 particle was measured using a pycnometer at room temperature and then linearly extrapolated to higher temperatures [23].

Table 5-1 Physical properties of slag and Al_2TiO_5 particles at 1773 K used for dissolution studies

Component	Al_2O_3 (wt pct)	CaO (wt pct)	SiO_2 (wt pct)	Liquidus temperature (K)	Density (kg/m^3)	Viscosity (Pa.s)
Slag 1	20±0.7	40±0.4	40±0.5	1595±3	2651±80	3.5±0.9
Slag 2	23.2±1.2	30.5±0.7	46.3±1.2	1715±3	2640±79	9.5±2.4
Al_2TiO_5	--	--	--	2133	3804±114	-

The particle-slag configuration in CSLM is discussed in detail in a previous publication [19] wherein a single Al_2TiO_5 particle is placed on the surface of the pre-molten slag in a platinum crucible. During the experiment, it is ensured that the mass of the particle is less than one pct of the mass of the slag. The particle, sample holder, and crucible were heated to the experimental temperature under an argon atmosphere at 0.2 l/min. The temperature in CSLM is measured using a B type thermocouple located at the bottom of the crucible holder. The temperature of the slag surface is different than the temperature at the bottom of the crucible, where the thermocouple is attached. Thus, the temperature at the thermocouple must be calibrated so that the temperature at the reaction site is precisely achieved. The thermocouple is calibrated using melting point of 99.5 pct pure iron disc purchased from Alfa Aesar USA. The temperature reading from the thermocouple at the melting point of the iron disc was compared with the theoretical melting point of pure iron at 1812 K. The temperature reading by the CSLM includes two types of errors; (1) temperature calibration error due to difference in spatial position of reaction site and thermocouple position and (2) standard error associated with thermocouple. In this study, a B type thermocouple was used, which is known to have about ±0.5pct of the temperature error (±8 K) at 1873 K [24]. It was found that the surface temperature of the sample is 63 K higher than that of thermocouple temperature when pure iron was melted.

The heating schedule used for inclusion dissolution work for a target temperature of 1773 K is shown in Figure 5-1. The CSLM chamber was heated from 423 K to 1673 K at the rate of 1000 K/min. A fast heating rate of 1000 K/min is used while studying the dissolution of Al_2TiO_5 because the particle dissolves very quickly, as observed in preliminary experiments by the authors. After reaching 1673 K, the temperature is raised to 1773 K at a rate of 100 K/min. At 1773 K, the particle-slag system is held for different dissolution time. For studying the dissolution rate, the system temperature is held constant until the particle is completely dissolved at the experimental temperature. For studying the dissolution mechanism, the particle-slag system is quenched at different stages of dissolution to characterize the phases formed within the system as the dissolution proceeds. The quenching is done by purging helium at 4.05×10^5 Pa pressure at the rate of 0.2 l/min. For the dissolution and the quench experiments, time zero is the moment designated when the experimental temperature is reached.

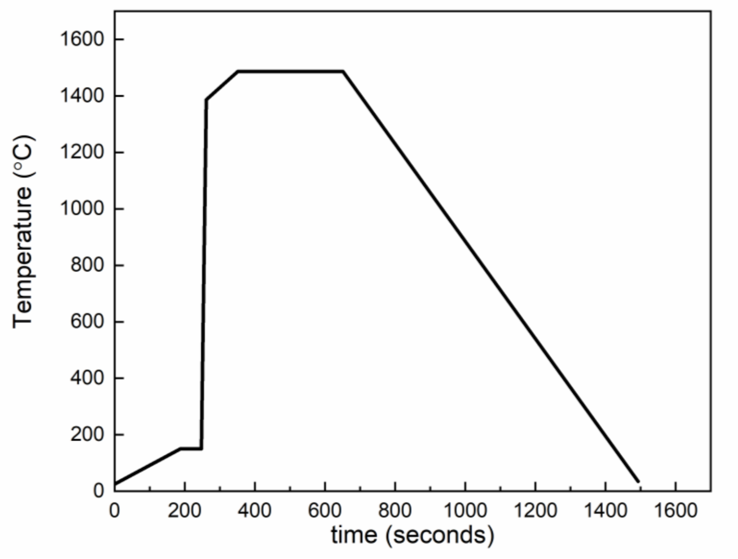

Figure 5-1 Heating schedule for Al_2TiO_5 dissolution experiment

Different stages of dissolution are defined as $(R_0-R)/R_0*100$ where R is the equivalent circular radius at quenching and R_0 is the radius at time zero. For slag 1, the particle-slag interface was analyzed at 0 pct, 33 pct, and 55 pct dissolution. For slag 2, the particle-slag interface is studied at 0 pct, 28 pct, and 52 pct dissolution. Due to the fast dissolution rate, it was difficult to obtain more samples towards the end of the dissolution. For slag 1, the samples analyzed under the SEM for 0 pct and 33 pct dissolution needed no preparation. This is because the particle for these cases remained close to the top surface in both cases and on quenching the slag cracked at the particle-slag junction. For the quenched sample after 55 pct dissolution , the particle sank to the bottom of the crucible, and the slag needed grinding from one of the sides to reveal the particle-slag surface. Thus, images from the quenched sample after 55 pct dissolution are relatively smoother than the 0 pct and 33 pct sample. For slag 2, the samples analyzed for 0 pct, 28 pct, and 52 pct dissolution needed no sample preparation. The analysis of the as-quenched sample without any polishing avoids disturbance of the natural state of the particle slag system and any impurities. Also, from the experience of the authors, it is very easy to lose the particles from slag during mechanical operations such as mounting, grinding, or polishing of the sample. The quenched particle-slag cross-section is studied with a JEOL 6610 SEM for elemental analysis by EDX line scan analysis. Area mapping and point analysis around each particle are also performed. The SEM/EDX analysis in conjunction with the thermodynamic phase stability diagrams serves as a mean for identification of phases appearing at the particle-slag interface.

5.3 Results

5.3.1 Thermodynamics of inclusions dissolution

In the current work, the phase diagrams are produced using FactSage 7.2 ^{TM} using the FACT-Oxid database. The phase diagrams for the slag-Al_2TiO_5 particle system is presented in the form of an isopleth shown in Figure 5-2 and Figure 5-3. The X-axis in the two figures represents the ratio of the mass of the particle to the mass of the slag. At the current temperature of interest, 1773 K and above, solid Al_2O_3 and liquid slag are the stable phases for both slag 1 and slag 2 systems.

The composition of the liquid slag can be approximated from the phase diagram. It can be assumed that under local equilibrium at the particle-slag boundary, the slag in the boundary layer will be saturated with Al_2TiO_5. The composition of the saturated slag is estimated by assuming a straight dissolution path. Table 5-2 shows the composition of the saturated slag and possible phases present at the particle slag boundary. The composition is presented in the form of weight pct of elements since the elemental composition can be later used to compare with line scan data obtained from EDX analysis. In addition to bulk slag, Al_2TiO_5 saturated slag and Al_2O_3, the composition of $CaTiO_3$ is presented. $CaTiO_3$ can form by local saturation of TiO_2 in a 20 pct Al_2O_3- - 40 pct CaO - 40 pct SiO_2 slag at 1703 K [18]. From Table 5-2, the concentration of Al and Ti increased while the concentration of Ca and Si decreased in the Al_2TiO_5 saturated slag in comparison to the bulk slag. The concentration of Al follows the order: Al_2O_3 > Al_2TiO_5 particle > Al_2TiO_5 saturated slag > bulk slag. The concentration of Ti follows the order: $CaTiO_3$ > Al_2TiO_5 particle > Al_2TiO_5 saturated slag > bulk slag.

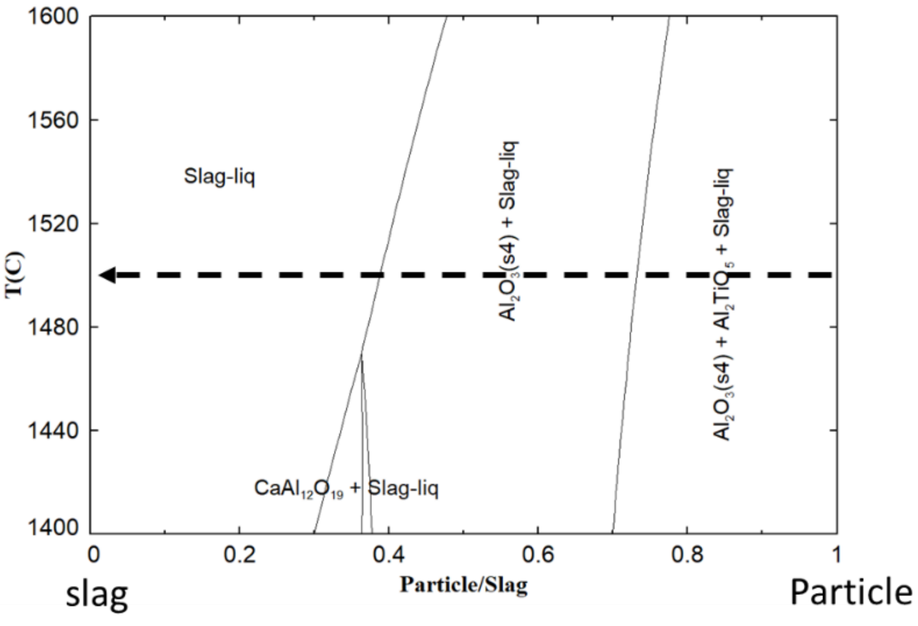

Figure 5-2 Isopleth section for Al_2TiO_5 particle and slag 1 system

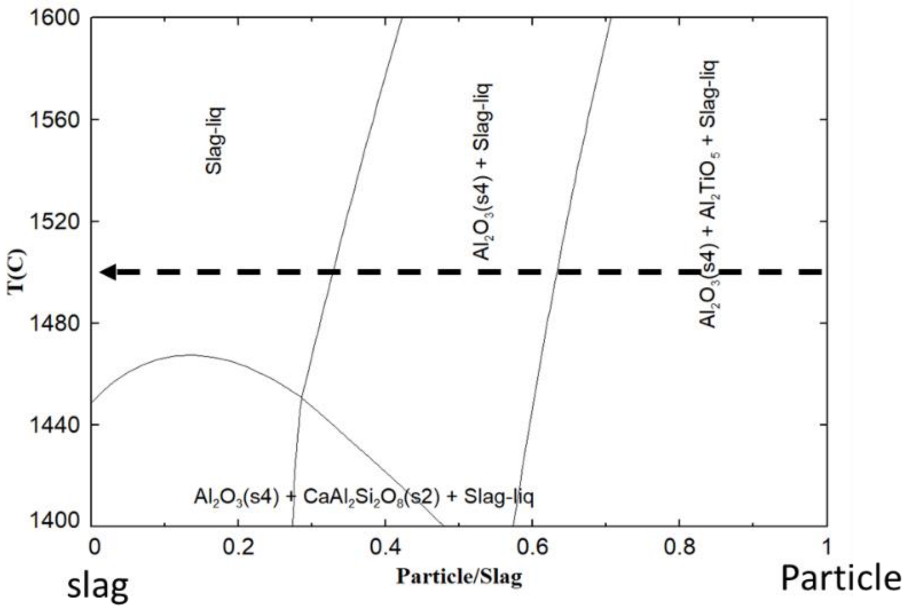

Figure 5-3 Isopleth section of Al_2TiO_5 particle and slag 2 system

Table 5-2 List of the elemental composition of bulk and saturated slags, Al_2TiO_5, Al_2O_3 and $CaTiO_3$ at 1773K (wt pct)

Slag/ constituents	Al	Ca	Si	Ti	O
Slag 1 bulk	11	29	19	0	42
Slag 1 saturation	19	19	12	7	43
Slag 2 bulk	12	22	21	0	44
Slag 2 saturation	19	16	15	6	44
Al_2TiO_5 particle	30	0	0	26	44
Al_2O_3	53	0	0	0	47
$CaTiO_3$	0	29	0	35	35

5.3.2 In situ dissolution in slag 1 and slag 2

In the CSLM, the microscope is located above the high-temperature furnace. The phenomena observed through the microscope is captured by a charge-coupled device (CCD) camera. Therefore, it is only possible to capture the projection of the dissolving particle on a horizontal plane. The oxide particle and the slag on this plane are distinguished based on a difference in contrast. The contrast in each picture frame is adjusted by the operator during the experiment to obtain a sharp image with a clear boundary between the particle and slag. Figure 5-4 and Figure 5-5 show CSLM video images from the in situ dissolutions of Al_2TiO_5 particles in slag 1 and slag 2 at 1773 K, respectively. During the dissolution process, the Al_2TiO_5 particles were covered by the slag and suspended close to the surface of the slag. No significant rotation of particles was observed except at the very end of the dissolution process. The slag in the vicinity to the particle acquired a darker hue in comparison to the initial bulk slag for both slags right from the beginning of dissolution and continued till the end. From Figure 5-6, it is seen that during the dissolution process, bubbles of gas evolved and burst at different sites on the particle. It is known from experience that these bubbles are not the ones trapped in slag during melting. These bubbles continuously grew and burst during the dissolution process. It is important to note that bubbles evolved for experiments whose data are shown in Figure 5-4 and Figure 5-5. The bubbles are not shown in the image to show a clear dissolution process.

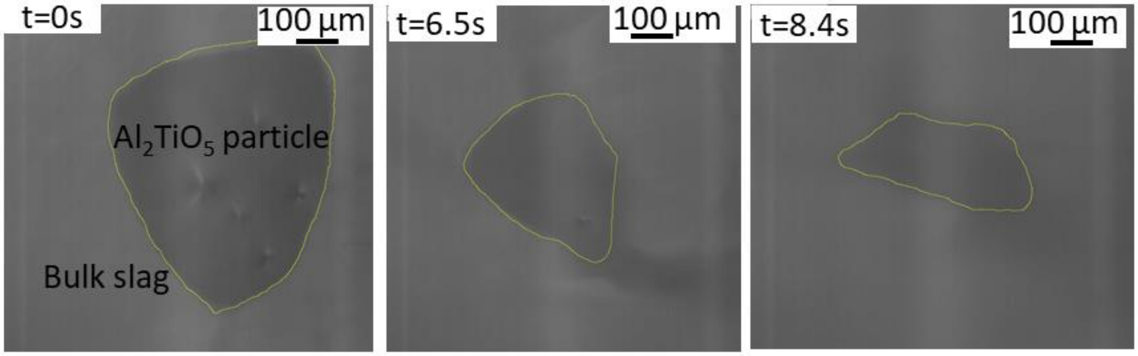

Figure 5-4 CSLM images from the dissolution of a single Al_2TiO_5 particle in slag 1 at 1773 K

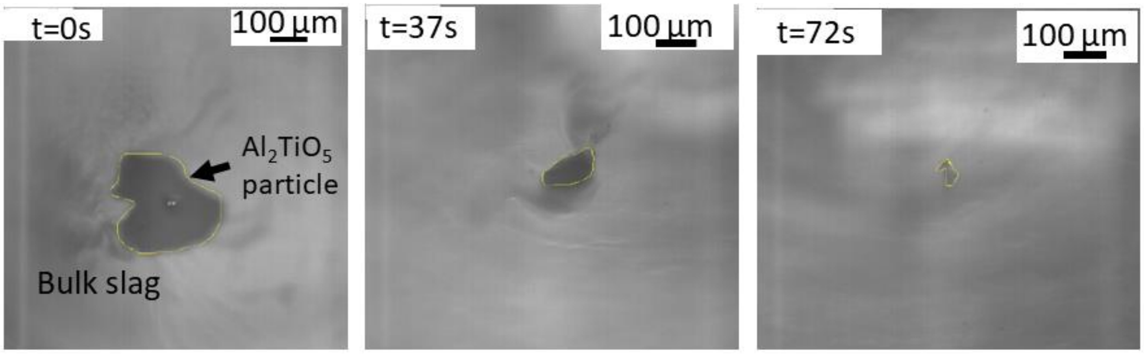

Figure 5-5 CSLM images from the dissolution of a single Al_2TiO_5 particle in slag 2 at 1773 K

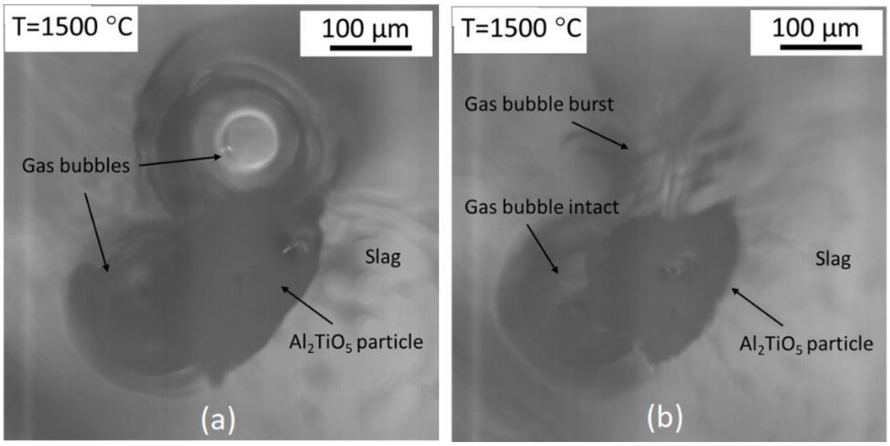

Figure 5-6 CSLM images of gas bubbles (a) evolving and (b) bursting during the dissolution of Al_2TiO_5 particle in slag

5.3.3 Assessment of particle-slag interface

To better understand the dissolution mechanism of Al_2TiO_5 particles, the particle-slag interface is studied using SEM-EDX line scan analysis. The concentration profile of Al, Ti, Ca, and Si would help understand the change in local composition at the particle-slag interface with the progress of dissolution. The raw data for all experiments were converted to concentration distribution. Due to the rough particle-slag interface and formation of cracks during quenching, it was difficult to obtain reproducible results. However, a combination of point analysis and elemental map provided a better understanding of the distribution of constituent elements from anticipated phases, as shown in Figure 5-2 and Figure 5-3. The anticipated phases are defined with respect to Table 5-2 in the rest of the chapter, as shown in the following. Any region in the particle-slag system, which shows the presence of Al, Ca, Si and does not show Ti is termed bulk slag. Regions where Al, Ca, Si, and Ti are simultaneously present are referred to Ti-rich slag. Regions where Al concentration shows a peak but Ca, Si and Ti are absent or redundant are referred as Al_2O_3. Regions where Ca and Ti concentration peaks appear simultaneously but Al and Si are absent or low in concentration are assumed to be $CaTiO_3$. In this study, the thickness of the particle-slag interface is defined as the distance between bulk slag and the unreacted Al_2TiO_5 particle. Since TiO_2 is not present in the bulk slag, its concentration change can be used for identifying the particle-slag interface. For the line analysis shown in Figure 5-7 and Figure 5-8, the line starts at the bulk slag, crosses the interface, and ends in the particle. The details of the particle-slag interface for each quenched sample are described below.

5.3.3.1 Dissolution in slag 1

Figure 5-7 (a) shows a back-scattered electron image of the particle-slag system and line scan to study the interface and the line scan data of Al, Ti, Ca and Si for the quenched sample after 0 pct dissolution. Following the definition stated in section 3.3 to identify different regions in the line scan, the sequence and width of phases are as follows. Bulk slag – 58 µm of Ti-rich slag – 13 µm of Al_2O_3 – 5 µm of Ti-rich slag – 6 µm of Al_2O_3 – 8 µm of Ti-rich slag – unreacted Al_2TiO_5 particle. The width of the interface is 90 µm.

Figure 5-7 (b) shows the region analyzed by line scan for the quenched sample after 33 pct dissolution. Using a similar methodology, the phases appear in the following sequence. Bulk slag - 14 µm of Ti-rich slag – 4 µm of $CaTiO_3$ – 4 µm of Ti-rich slag – 2 µm of $CaTiO_3$ – 2 µm of Ti-rich slag – 2 µm of $CaTiO_3$ – 8 µm of Al_2O_3 – 5 µm of $CaTiO_3$ – 15 µm of Al_2O_3 – 16 µm of Ti-rich slag – unreacted Al_2TiO_5 particle. The width of the interface is 72 µm.

Figure 5-7 (c) shows the region scanned by line scan for the quenched sample after 55 pct dissolution. The type of phases and width of the phases at the particle slag interface is reported. Bulk slag- 12 µm of Ti-rich slag – 5 µm of $CaTiO_3$ – 5 µm of Al_2O_3 – 24 µm of Ti-rich slag –unreacted Al_2TiO_5 particle. The width of the interface is 46 µm.

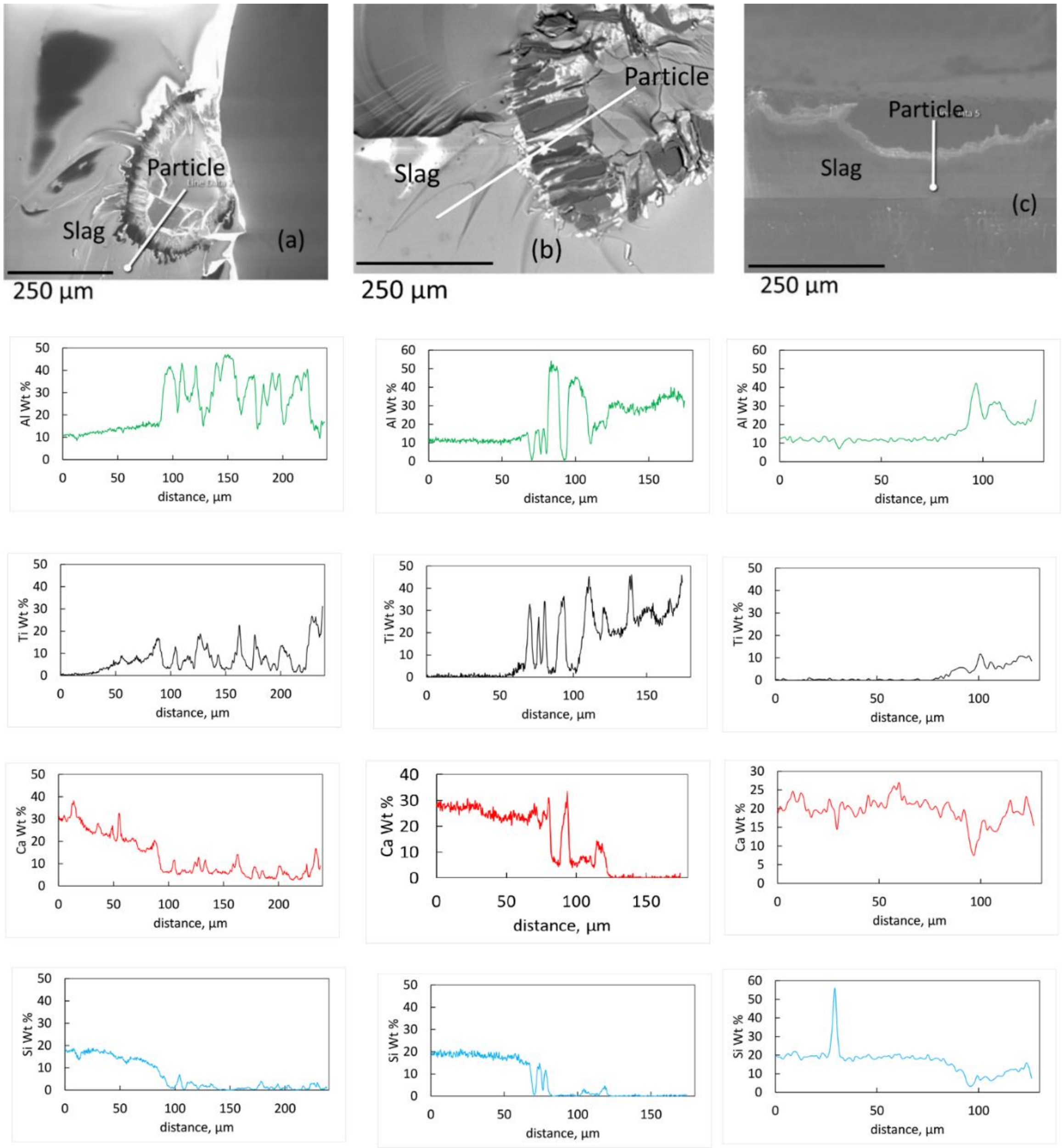

Figure 5-7 SEM backscattered electron image and EDS line analysis of the particle-slag 1 interface for the quenched sample after (a) 0 pct Dissolution (b) 33 pct Dissolution (c) 55 pct Dissolution

5.3.3.2 Dissolution in slag 2

Figure 5-8 (a) shows a back-scattered electron image of particle-slag 2 system and line scan to study the interface and the line scan data for Al, Ti, Ca, and Si for the quenched sample after 0 pct dissolution. Following the key for phase identification established in section 3.3, the following phases are identified. Bulk slag – 12 µm of Ti-rich slag – 6 µm of Al_2O_3 – 2 µm of $CaTiO_3$ – 12 µm of Ti-rich slag – 4 µm of $CaTiO_3$ – 14 µm of Al_2O_3 and $CaTiO_3$ – 10 µm of Ti-rich slag – unreacted Al_2TiO_5 particle. The width of the interface is 60 µm.

Figure 5-8 (b) represents a line scan forthe quenched sample after 28 pct dissolution in slag 2. The type of phases and width of respective phases are stated as follows. Bulk slag - 26 µm of Ti-rich slag – 16 µm of Al_2O_3 – 6 µm of $CaTiO_3$– 6 µm of Ti-rich slag– unreacted Al_2TiO_5 particle. The width of the interface is 54 µm.

Figure 5-8 (c) represents the distribution of Al, Ti, Ca, and Si for the quenched sample after 52 pct dissolution. The following phases are identified at the particle-slag interface. Bulk slag – 16 µm of Ti-rich slag – 16 µm of Al_2O_3 – 2 µm of $CaTiO_3$ – 35 µm of Ti-rich slag– unreacted Al_2TiO_5 particle. The width of the dissolution boundary is 69 µm.

From the observations made in section 5.5.1 and 5.5.2, these results indicate that the multi-layer structure of reaction/dissolution products is observed at the particle-slag interface in each sample. With the aid of Factsage software, it is found that solid alumin phase and liquid aluminum titanate saturated slag phases co-exist at the particle-slag interface. No particular order of these phases is observed. The thickness of these phases decreases with the progress of dissolution.

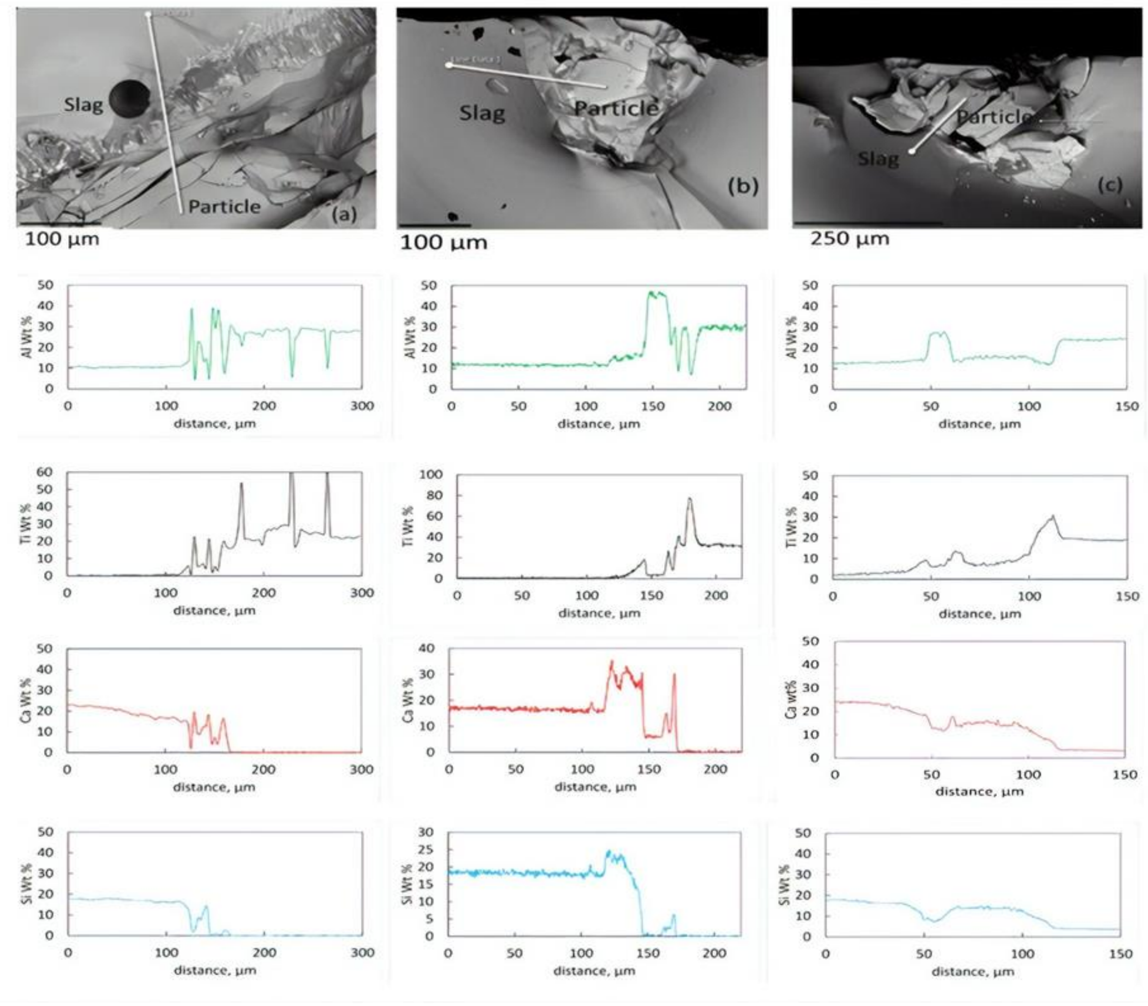

Figure 5-8 SEM backscattered electron image and EDS line analysis of the particle-slag 1 interface for the quenched sample after (a) 0 pct Dissolution (b) 28 pct Dissolution (c) 52 pct Dissolution

5.3.4 Dissolution rate

The dissolution rate of Al_2TiO_5 particles into the slag is expressed as the rate of decrease of the radius of solid particles. Figure 5-9 shows the changes in the equivalent radius of the particle with time in slag 1 and slag 2 at 1773 K. In slag 1, the dissolution time for Al_2TiO_5 particle of a radius of 131 µm is 29 s whereas, in slag 2, the dissolution time for Al_2TiO_5 particle of the equivalent circular radius of 151 µm is 75s. The dissolution rate of Al_2TiO_5 particle is faster in slag 1 than that in slag 2. Further, the dissolution rate is slightly faster in the early part of the process in slag 1 whereas it is slower in the early part of the process (<50 pct. of total dissolution time of slag 2) in slag 2. The dissolution time is the time taken for the particle to reach an R/R_0 ratio of 0.2 in slag 1 and slag 2.

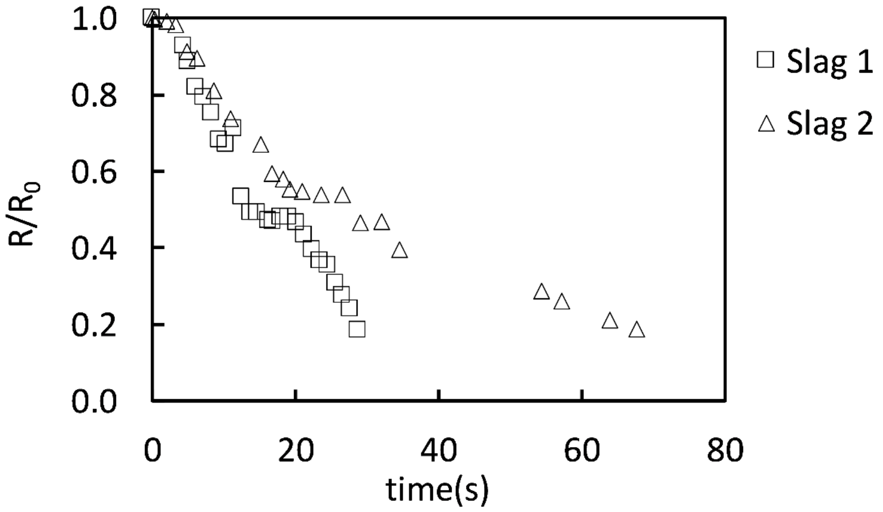

Figure 5-9 Change in the normalized radius of Al_2TiO_5 particles with time in slag 1 and slag 2 at 1773 K

5.4 Discussion

5.4.1 In situ dissolution of Al_2TiO_5

During the dissolution of Al_2TiO_5 particles, some dark fluid flow leaving the particle was observed as seen in Figure 5-4 and Figure 5-5. Since Ti is the only transition element in the particle-slag system under observation, the darker hue of the slag indicates the presence of Ti in the dark fluid. This observation was also supported with SEM line scan in Figure 5-7 and Figure 5-8, where a Ti-rich slag was observed at the interface. However, it is also to be noted that the darker hue can also be present due to a gap between the particle and slag. The contrast is by virtue of the very nature of confocal imaging.

5.4.2 Dissolution path of Al_2TiO_5

The particle-slag system initially consisted of Al_2TiO_5 particle and Al_2O_3-CaO-SiO_2 slag before the start of dissolution. The observation from SEM analysis of quenched samples shown in both Figure 5-7 and Figure 5-8 in both slags shows that the multi-layer structure of the particle-slag interface exists during the progress of the dissolution process. This indicates that particle dissolution and slag penetration proceed simultaneously. This finding is consistent with the literature [17]. In this study, the CaO/SiO_2 ratios of slags at the particle-slag interface is greater than that in bulk slag. This indicates that the diffusion rate of CaO is higher than that of SiO_2. Similar results were reported by Oishi et al. [25] and Park et al. [26] for the dissolution of Al_2O_3 in CaO-SiO_2-Al_2O_3 slags.

Al_2O_3 is detected at the particle-slag interface in all the quenched samples, as shown in Figure 5-7 and Figure 5-8. This is most likely due to the dissociation of Al_2TiO_5 under the studied experimental conditions. It is known from the literature that Al_2TiO_5 is unstable under a reduced partial pressure of oxygen [27]. The decomposition reaction can be written as shown in equation 5-2 [27].

$$(3-2z)[(Al^{+3})_2(Ti^{+4})_1(O^{-2})_5] = \left(Al_z{}^{+3}Ti_{1-z}\right)_2(Ti^{+4})_1(O^{-2})_5 + 3(1-z)Al_2O_3 + \frac{1}{2}(1-z)O_2 \tag{5-2}$$

where z is the oxygen partial pressure. It is well known that the partial pressure of oxygen directly affects the stability of TiO_2[28] and Al_2TiO_5[29]. Seifert and Aldinger [27] used the thermodynamic calculations followed by experimental verification at 1973 K to investigate the stability of Al_2TiO_5 by the effect of P_{O_2}. In reaction 2, for z close to 0, the equation can be written as Al_2TiO_5 decomposes to Ti_3O_5, Al_2O_3, and O_2. Further Al_2O_3 phase is a stable phase as illustrated in Figure 5-2 and Figure 5-3, so the existence of this phase at the interface is expected. The gas evolved during the dissolution process is most likely to be oxygen, although it was not possible to directly analyze the chemical composition of the off-gas with the current CSLM setup. The effect of P_{O_2} on the stability of aluminum titanate will be reported in a future publication.

Ti_3O_5 and non-stoichiometric aluminum titanate should dissolve in the slag penetrated and form Ti-rich slag. $CaTiO_3$ phase is detected continuously at the particle-slag interface for both slag systems, as illustrated in Figure 5-7 and Figure 5-8. Figure 5-10 shows the backscattered electron image of the particle-slag 2 interface at time zero. It can be seen that the $CaTiO_3$ phase is in the form of dendrites. Since this phase was not one of the stable phases (see Figures 5-2 and 5-3), this finding confirms that it is precipitated out from the Ti-rich slag phase. A similar result was observed by Ren et al. [18]. The alumina layer detected at the interface is bulky, irregular, and discontinuous. Similar morphologies are observed for other quenched particle - slag samples. $CaTiO_3$ phase likely nucleates randomly on particle surface whereas Al_2O_3 most likely nucleate spontaneously on the entire particle surface. In chapter 3, it was argued that $CaTiO_3$ can be a reaction product. However, characterization of the particle-slag interface studied by SEM (as shown in Figure 5-10) confirmed that it is a solification product, not a chemical reaction product.

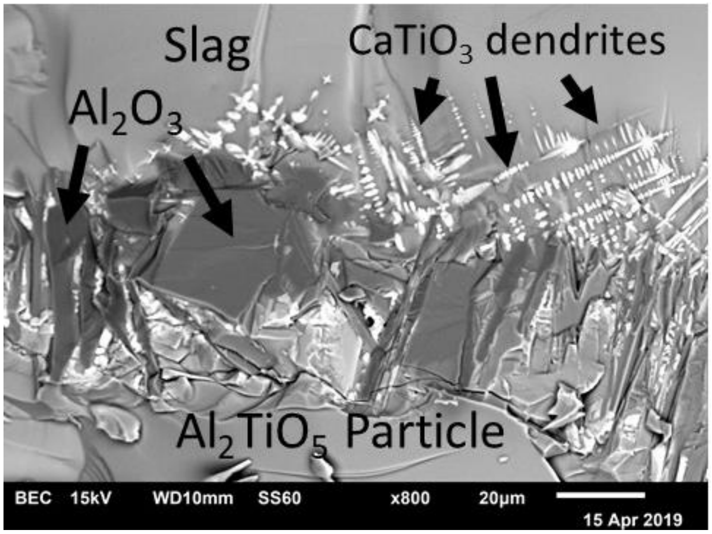

Figure 5-10 Backscattered electron image of Al_2TiO_5 particle-slag 2 interface at time-zero showing bulky Al_2O_3 and $CaTiO_3$ dendrites

The interfacial layer thickness has the highest value at time=zero and decreases as time progresses. This result is slightly different than what is expected. This is due to the definition of time zero, in this case, the time zero is when the experimental temperature reaches 1773 K. The slag becomes liquid before reaching experimental temperature approximately around 1595 K for slag 1 and 1703 K for slag 2. The system requires a minimum of 35 s to raise 1773 K, and this time is sufficient for initial reactions between particle and slag to occur. Concerning the discussed reaction and observations, the dissolution mechanism is proposed as shown schematically in Figure 5-11.

In step 1 as slag become liquid, the particle is immersed in the slag. In step 2, particle dissociates to Al_2O_3, Ti_3O_5, and O_2 bubbles while slag penetrates through the particle. This is most likely the reason why patches of Ti-rich slag and Al_2O_3 are observed surrounding the particle in Figure 5-7 and Figure 5-8. As the dissolution proceeds, these patches dissolve into the bulk slag, which is seen in the form of the fluid flow observed during dissolution. As dissociation proceeds, the particle shrinks in size and Ti_3O_5 and Al_2O_3 are continuously formed as seen in step 3. Finally, the particle dissolves into the slag completely.

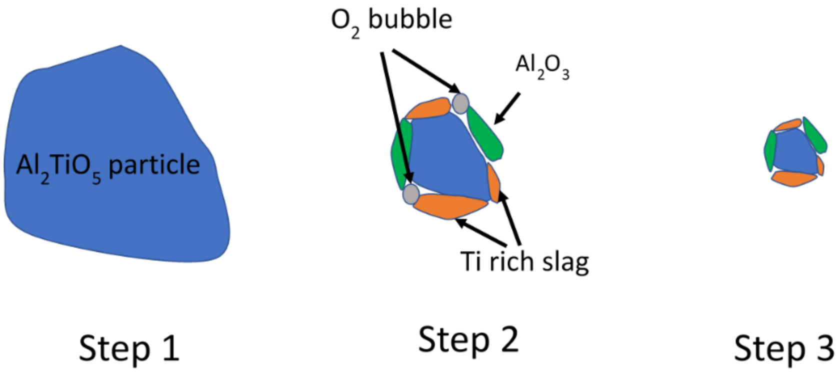

Figure 5-11 Schematic diagram of Al_2TiO_5 inclusion dissolution mechanism

5.4.3 Rate controlling mechanism

A comparison of the experimental data points with the theoretical models can provide insight into the rate-controlling step. The authors compared their previous experimental results with the shrinking core model (SCM) [19,20,30,31]. For consistency, the same model is applied in this work. There are two rate-controlling steps considered namely, chemical reaction control and mass transfer control. The model suggests (a) linear relationship of the radius with time for chemical reaction control as shown by equation 5-3 and (b) parabolic relation of the radius with time as shown by equation 5-4 for mass transfer control (with diffusion through a boundary layer) in Stoke's regime [32].

$$\frac{\mathrm{R_c}}{\mathrm{R_0}} - 1 = \frac{\mathrm{bK_R \Delta C}}{\rho_{\mathrm{particle}} \mathrm{R_0}} \mathrm{t} \tag{5-3}$$

$$\left(\frac{\mathrm{R_c}}{\mathrm{R_0}}\right)^2 - 1 = \frac{\mathrm{2b\Delta CD}}{\rho_{\mathrm{particle}} \mathrm{R_0^2}} \mathrm{t} \tag{5-4}$$

where Rc and R_0 are instantaneous and initial radii (in m), t is the instantaneous time (in s), $\rho_{particle}$ is the particle density (in kg/m^3), b is the stoichiometric constant and equal to 1, ΔC is the difference in concentration of the rate-controlling species in bulk slag and slag at saturation (in kg/m^3), K_R is the first-order rate constant for the surface reaction in (m/s), and D is the diffusivity of the species under consideration (in m^2/s).

The degree of a fit parameter is used to differentiate between the two rate-controlling steps. This method is adopted from the work of Monaghan and Chen [33]. The experimental data in Figure 5-9 are replotted in Figure 5-12 and Figure 5-13 for slag 1 and slag 2, respectively. The regression line for slag 1 is in reasonable agreement with the experimental data under the assumption of chemical reaction control in comparison to mass transfer control. In the case of slag 2, there is a significant discrepancy between regression lines and experimental data regardless of the rate-controlling step selected. It is important to note that the mass transfer control model is an oversimplification of the dissolution phenomenon. It is applicable for small particles with laminar flow in slag [34]. In the current study, the authors observe gas bubbles formation, growth, and bursting, which is not considered in equation 5-4. The gas bubbles influence fluid flow behavior. Under the defined conditions, it is impossible to control this phenomenon. The gas bubble enhances the mass transport of species to the bulk slag by promoting local convection.

Further, the degree of a fit parameter, R^2 values for chemical reaction control are 0.95 and 0.83 for experiments with slag 1 and slag 2, respectively whereas the R^2 values for mass transfer control are 0.81 and 0.53 for experiments with slag 1 and slag 2, respectively. Even though the R^2 values are higher for chemical reaction control, the values are generally lower than 0.95. The results indicate that this test is insufficient to determine the rate-controlling step.

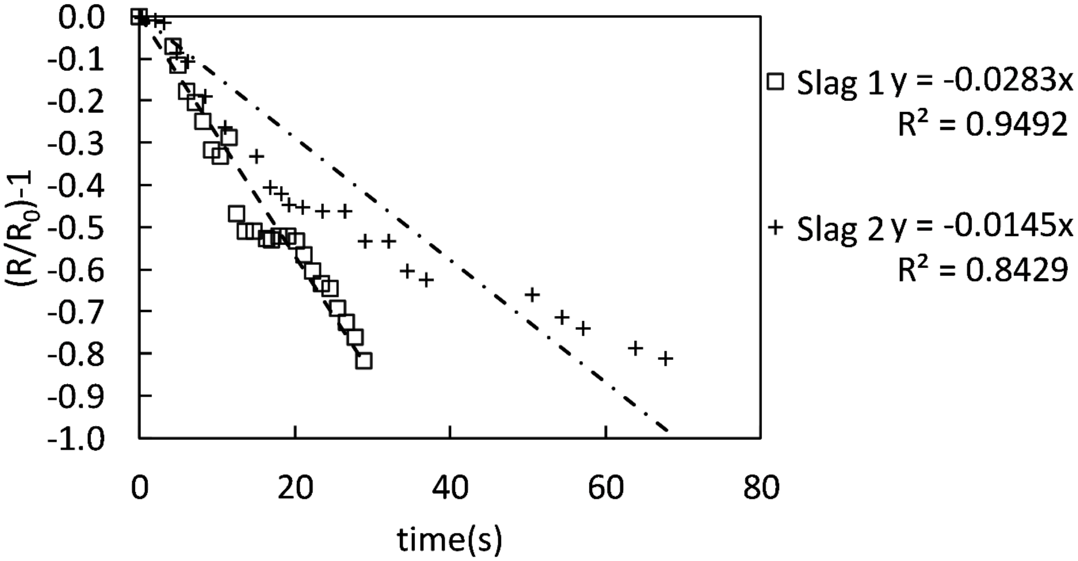

Figure 5-12 Comparison of Al_2TiO_5 dissolution data for slag 1 and slag 2 with SCM assuming chemical reaction control

The particle-slag interface characterization indicates that there is an enriched Ti phase at the interface on the slag side of the interface for both slags studied. Since the dissolution times are relatively fast, the slag composition away from the interface is unchanged. The composition of the Ti-rich phase at the interface was similar to saturated slag composition as shown in Table 5-2. This indicates that the chemical reactions at the interface are relatively rapid than the transport of species. Further, the existence of concentration gradients is consistent with diffusion of species through a boundary layer being the rate-controlling step.

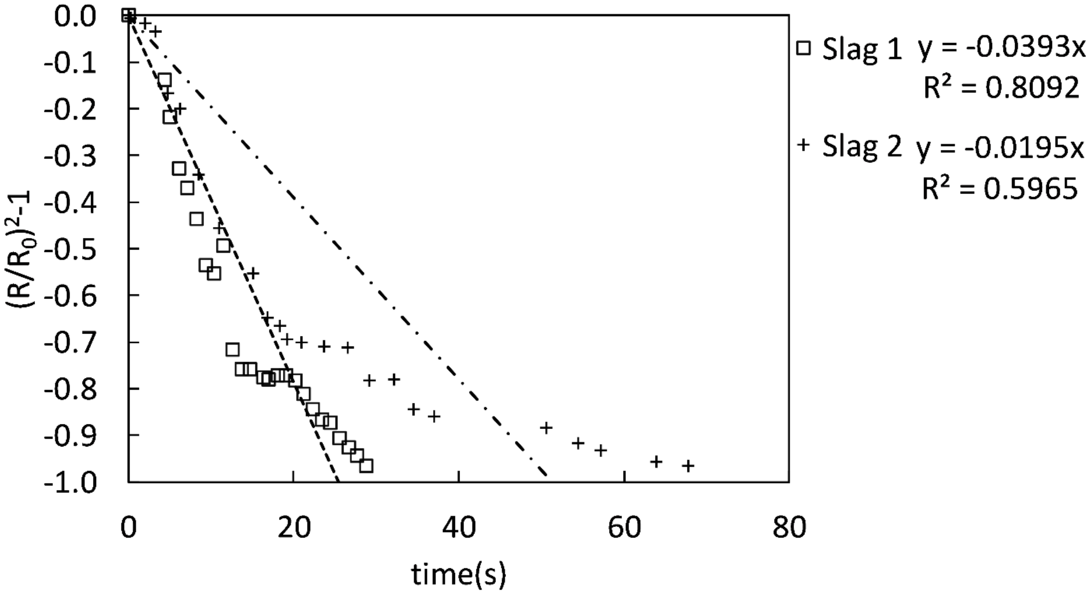

Figure 5-13 Comparison of Al_2TiO_5 dissolution data for slag 1 and slag 2 with SCM assuming mass transfer control

If diffusion is rate-controlling step, the diffusivity of dissolving species is inversely proportional to the viscosity of slag according to Stoke - Einstein equation [35]. In this study, aluminum–oxygen complex anion, as well as titanium cation, are assumed to be possible rate-limiting species. For simplicity, AlO_x and Ti^{4+} are referred to as Al_2O_3 and TiO_2, respectively, in the following text. Even though the R^2 values for mass transfer control show a wide range of values in Figure 5-13, Equation 5-4 is employed to estimate the diffusivity of Al_2O_3 and TiO_2 from the slope of the best fit lines and diffusivity values are summarized in Table 5-3. These values are relatively higher than those reported in the literature [18,36,37]. This is expected due to the stirring effects of bubbles, thereby promoting local convection. Following Table 5-1, the viscosity of slag 1 is lower than that in slag 2; thus, the diffusivity in slag 1 is expected to be higher in slag 2. This is in agreement with the measurements made from CSLM data. Similar results were found using diffusivity values for TiO_2.

Table 5-3 Estimated diffusivity values obtained from the mass transfer control model

Diffusivity	Slag 1	Slag 2
D Al_2O_3, m^2/s	2.8×10^{-9}	1.8×10^{-9}
D TiO_2, m^2/s	3.8×10^{-9}	5.5×10^{-9}

5.5 Conclusions

The dissolution mechanism of Al_2TiO_5 particles in CaO- SiO_2-Al_2O_3 slag systems was studied at 1773 K using CSLM technique. From the in-situ observations and SEM/EDX analysis, the following conclusions are made:

1. SEM line scan detected phases such as (1) Al_2O_3, and (2) Ti-rich slag at the particle-slag interface at different stages of dissolution in both slags studied. This is following the thermodynamic predictions. The presence of Al_2O_3 at the particle - slag boundary does not affect the overall dissolution kinetics. This is most likely because the Al_2O_3

formed at the interface is discontinuous. In quenched samples, $CaTiO_3$ is also detected, which can be a precipitation product from local saturation of the slag with TiOx.

2. The dissolution path of Al_2TiO_5 is suggested as follows: The Al_2TiO_5 dissociates to form Al_2O_3, TiO_x, and O_2 gas. The Al_2O_3 and TiO_x dissolve in the bulk slag by simultaneously creating a Ti-rich slag. The existence of gas bubbles enhances the overall rate of Al_2TiO_5 dissolution.
3. The dissolution of Al_2TiO_5 appears to be controlled by mass transfer in the slag. Evidence in support of this finding is the particle-slag interface characterization by line scan analysis and calculated diffusivity values being inversely proportional to the viscosity of slag. The diffusivity values are relatively higher compared to those reported in the literature due to the stirring by the gas bubbles.

5.6 Acknowledgement

The authors would like to acknowledge the support of the Natural Sciences and Engineering Research Council of Canada (NSERC, Project No. 20000514) for funding this research. This research used a high-temperature confocal laser scanning microscope - SVF17SP funded by Canada Foundation for Innovation John Evans Leaders Fund (CFI JELF, Project Number: 32826) and a scanning electron microscope - JEOL 6610 located at the Canadian Centre for Electron Microscopy at McMaster University.

5.7 **Reference**s

1 T. Liu, L. Chen, H. Bi, and X. Che: *Acta Metall. Sin. (English Lett.*, 2014, vol. 27, pp. 452–6.

2 M. Vedani and A. Mannucci: *ISIJ Int.*, 2008, vol. 42, pp. 1520–6.

3 M.B. Assar and J. Singleton: in *AISTech*, vol. II, 2005, pp. 39–48.

4 Y. Zhang and M.S. Dudzic: *J. Process Control*, 2006, vol. 16, pp. 819–29.

5 S. Ogibayashi: *Taikabutsu Overseas*, 1994, vol. 15, pp. 3–14.

6 J. Burja, F. Tehovnik, J. Lamut, and M. Knap: *Mater. Tehnol.*, 2013, vol. 47, pp. 217–22.

7 F. Tehovnik, J. Burja, B. Arh, and M. Knap: *Metalurgija*, 2015, vol. 54, pp. 371–4.

8 J.D. Smith and K.D. Peaslee: *Development of Submerged Entry Nozzles That Resist Clogging*, 2002.

9 S. Abdelaziz, G. Megahed, I. El-Mahallawi, and H. Ahmed: *Ironmak. Steelmak.*, 2009, vol. 36, pp. 432–41.

10 S. Basu, S.K. Choudhary, and N.U. Girase: *ISIJ Int.*, 2004, vol. 44, pp. 1653–60.

11 O. Araromi, B.G. Thomas, and E. Conzemius: *Mater. Sci. Technol. Conf.*, 2009, pp. 1–10.

12 J.W. Farrell and D.C. Hilty: in *28th Electric Furnace Proceedings*, 1971, pp. 31–46.

13 B.G. Thomas and H. Bai: *Iron Steel Soc.*, 2001, vol. 18, pp. 895–912.

14 P. Kaushik, R. Lule, G. Castillo, J.C. Delgado, F. Lopez, C. Perim, G. Pigatti, B. Henriques, F. Barbosa, and A. Nascimento: *Iron Steel Technol.*, 2016, vol. 13, pp. 168–85.

15 H. Cui, Y.P. Bao, M. Wang, and W.S. Wu: *Int. J. Miner. Metall. Mater.*, 2010, vol. 17, pp. 154–8.

16 A. Karasangabo and C. Bernhard: *J. Adhes. Sci. Technol.*, 2012, vol. 26, pp. 1141–56.

17 D. Wang, J. Liu, M. Jiang, F. Tsukihashi, and H. Matsuura: *Int. J. Miner. Metall. Mater.*, 2011, vol. 18, pp. 646–51.

18 Z.S. Ren, X.J. Hu, X.M. Hou, X.X. Xue, and K.C. Chou: *Int. J. Miner. Metall. Mater.*, 2014, vol. 21, pp. 345–52.

19 M. Sharma, W. Mu, and N. Dogan: in *AISTech 2018*, 2018, pp. 2601–8.

20 M. Sharma, H.A. Dabkowska, and N. Dogan: *Steel Res. Int.*, 2018, pp. 1–24.

21 M. Allibert, H. Gaye, J. Geisler, D. Janke, B.J. Keene, D. Kirner, M. Kowalski, J. Lehmann, K.C. Mills, D. Neuschutz, R. Parra, C. Saint Jours, P.J. Spencer, M. Susa, M. Tmar, and E. Woermann: in *Slag Atlas*, V.D.E. (VDEh), ed., 2nd edn., Dusseldorf, 1995, pp. 345–7.

22 K C Mills: in *slag atlas*, Verlag Stahleisen, 1995, p. 353.

23 J.F. Shackleford and W. Alexander: *Materials Science and Engineering*, 3rd edn., CRC Press, 2001.

24 Microlink Measurement & Control: Technical Notes on Thermocouple Accuracy, http://www.microlink.co.uk/tctable.html.

25 Y. OISHI, A. R. COOPER JR., and W.D. KINGERY: *J. Am. Ceram. Soc.*, 1965, vol. 48, pp. 88–95.

26 J.H. Park, I. Jung, and H. Lee: *ISIJ Int.*, 2006, vol. 46, pp. 1626–34.

27 H. jurgen Seifert and F. Aldinger: *Zeitschrift für Met.*, 1996, vol. 87, pp. 841–53.

28 M. Serratos and A. Bronson: *Wear*, 1996, vol. 198, pp. 267–70.

29 I.B. De Arenas: in *Sintering of Ceramics - New Emerging Techniques*, D.A. Lakshmanan, ed., 1st Ed., InTech, 2012, p. 503.

30 M. Sharma, W. Mu, and N. Dogan: *JOM*, 2018, vol. 70, pp. 1220–4.

31 M. Sharma and N. Dogan: in *Advanced Real Time Imaging II Cutting Edge Techniques in Materials Science Studies*, Jinichiro Nakano, P.C. Pistorious, C. Tamerler, H. Yasuda, Z. Zhang, N. Dogan, W. Wang, N. Saito, and B. Webler, eds., Springer, 2019, pp. 119–27.

32 O. Levenspiel: *Chemical Reaction Engineering*, vol. 19, Third., John Wiley and Sons, New york, 1999.

33 B.J. Monaghan and L. Chen: *Ironmak. Steelmak.*, 2006, vol. 33, pp. 323–30.

34 O. Levenspiel: *Chemical Reaction Engineering*, 2nd Ed., John Wiley & Sons, New York, 1999, pp.575.

35 M. Allibert, H. Gaye, J. Geisler, D. Janke, B.J. Keene, D. Kirner, M. Kowalski, J. Lehmann, K.C. Mills, D. Neuschutz, R. Parra, C. Saint Jours, P.J. Spencer, M. Susa, M. Tmar, and E. Woermann: in *Slag Atlas*, 2nd edn., Dusseldorf, 1995, p. 48.

36 B.J. Monaghan and L. Chen: *J. Non. Cryst. Solids*, 2004, vol. 347, pp. 254–61.

37 B.J. Monaghan, S.A. Nightingale, L. Chen, and G.A. Brooks: in *International*

Conference on Molten Slags Fluxes and Salts, South Africa, 2004, pp. 585–94.

Chapter 6
Effect of slag composition on the dissolution behavior of aluminum titanate inclusions

In chapters 3 and 4, the dissolution mechanism of Al_2TiO_5 particles was discussed using the shrinking core model. No differentiation can be made whether the dissolution mechanism is boundary layer diffusion controlled or chemical reaction controlled. In chapter 5, the particle-slag interface was further investigated. No composition gradient was found in either the bulk slag or the particle while a gradient was found to exist at the interface. Thus, there was an indication that the dissolution might be controlled by boundary layer diffusion. To confirm the inference from chapter 5, it was decided to examine the rate of dissolution of Al_2TiO_5 in different slag compositions at a constant temperature. Chapter 6 discusses the effect of slag composition on the dissolution behavior of aluminum titanate inclusions in three different slag compositions in 1500 °C. The rate of dissolution increased with an increase in slag basicity and viscosity. Because the mass transfer coefficient of aluminum titanate changed with the slag composition at a constant temperature, it is confirmed that overall dissolution is controlled by boundary layer diffusion control in slag.

The experimental kinetic data was collected by the primary author. Analysis of the data was shared between the primary author and Dr. Dogan. The manuscript was drafted by the primary author and reviewed to the final version by Dr. Dogan.

Effect of slag composition on the dissolution behavior of aluminum titanate inclusions

Abstract

The current work investigates the effect of slag composition on the dissolution behavior of aluminum titanate inclusions in three slag types at 1773 K. The dissolution is observed using a high-temperature confocal scanning laser microscope. In situ observation during inclusion, dissolution shows that gas bubbles evolve and burst at the inclusion surface. These bubbles provide stirring effect during dissolution, thus providing local convection which enhances mass transfer in slag. The effect of diffusion and convection is evaluated by estimating the mass transfer coefficient. It is found that the mass transfer coefficient increases with an increase in slag basicity.

6.1 Introduction

Titanium is an essential alloying element in automotive body steel. When added to the liquid steel, it combines with interstitial elements such as carbon and nitrogen to form simple and complex titanium carbides, nitrides and carbonitrides. These compounds precipitate at the grain boundaries to provide high strength and formability. Although titanium is beneficial in enhancing the mechanical properties of steel, its presence causes problems during the upstream processing. Basu et al. [1] studied the nozzle clogging behavior of titanium added and titanium free steel in a plant environment. They found that when titanium is added to steel, the ceramic nozzles clog more aggressively in comparison to the processing of titanium free steel. The cross-section of a clogged nozzle in a titanium alloyed steel shows that the clogged mass consists of three features; powdery alumina and spinel inclusions, fine-sized titanium bearing Al-Ti-O type inclusions and frozen steel skull. Basu et al. [1] concluded that the aggravated clogging is due to increased wetting of Al-Ti-O type inclusions by liquid steel. Karasangabo et al. [2] studied the wetting behavior of alumina substrates by Fe-Ti alloys at steelmaking temperatures using the sessile drop technique. They found that steel without titanium did not wet the alumina substrate much, and the wetting angle was measured at 130 degrees. When titanium is present in low concentrations at 0.1 wt pct, the wetting angle decreases to less than 90 degrees due to the formation of a layer of $FeAl_2O_4$ at the liquid steel/solid alumina interface. At high concentrations, the titanium reacts with alumina to form the Fe-Ti/TiOx interface. The wetting angle of titanium oxide by liquid iron lies in between 80 to 84 degrees. Thus, the presence of titanium in steel enhances the contact of steel and alumina, thereby aggravating the clogging.

Lee et al. [3] proposed a stepwise mechanism to delineate the mechanism of growth of clog in SEN from titanium alloyed ultra-low carbon steel. The mechanism for clog growth is as follows: (1) The increasing temperature inside the SEN refractory leads to a carbothermic reduction of refractory oxides such as Al_2O_3 and SiO_2. (2) The CO formed by carbothermic reduction reacts with Al, Ti, and Fe in the liquid steel simultaneously to form liquid Fe_tO-Al_2O_3-TiO_x and solid Al_2O_3 at the steel-refractory interface. (3) The liquid Fe_tO-Al_2O_3-TiO_x alters the wettability of alumina by steel. (4) The Fe_tO-Al_2O_3-TiO_x is reduced by Al and Ti in the steel with time to form Al_2O_3-TiOx complex phase. The proposed mechanism by Lee et al. [41] explains why a small amount of Ti addition to steel affects the clogging by a significant amount. However, the primary cause of clogging is suspected as adhesion of non-metallic inclusions to the refractory walls and can happen by the attachment of inclusions to the walls of the nozzle [41].

In another work, Rackers and Thomas [4] suggested that in general, a clogged nozzle contains 16 % of the oxide inclusions that flow through the nozzle. They reported that the steel in the clog freezes due to heat loss through the nozzle wall. The freezing can happen either due to low preheat of the nozzle or wide freezing temperature range of the liquid steel. The first clog layer forms by accruing and sintering small oxide particles. The inclusion network and the solidified steel grow into the molten steel and propagate the clog.

As stated above, different theories exist on the formation of a clog in the SEN and the presence of Al-Ti-O type inclusions in the clogs. These inclusions remain suspended in the steel as it is processed in the ladle, tundish and the mold. When the steel is held in the tundish, the different types of inclusions in the steel have an opportunity to interact with the slag. One way to reduce the amount of these inclusions is to ensure that these inclusions dissolve into the slag phase. The dissolution of inclusions in slag is conventionally studied by the dip test [5–14]. To the best knowledge of the authors, there are very few studies on the dissolution of titanium-containing inclusions in the slag phase [6,15]. Further, the ratio of the size of the substrate to the volume of the slag in the dip test is relatively larger in comparison to the industrial condition.

Application of the high-temperature confocal scanning laser microscope (CSLM) presents a significant advance in studying the “in-situ” dissolution behavior of inclusions in slag at high temperatures relevant to the steelmaking process. Non-metallic inclusions essential to steelmaking process have been studied using the CSLM [16–34]. The authors have reported the first dissolution kinetics data of Ti containing inclusions using CSLM [35–38]. The analysis shows that the rate-controlling step is boundary layer diffusion control. To further investigate the rate-controlling mechanism, the dissolution of aluminum titanate particle is studied by changing the slag composition. The current work reports the effect of slag composition on the dissolution rate of Al_2TiO_5 particles at steelmaking temperature.

6.2 Experimental Methodology

The dissolution rate of aluminum titanate inclusions in slag is measured at steelmaking temperature using a CSLM. The aluminum titanate particle is prepared using the optical floating zone method. The preparation of particles and slag for dissolution experiments is discussed in earlier publications [36, 38]. Table 6-1 shows the physical and chemical properties of the slag and particle used for the current work. The composition of the slag is measured by the inductively coupled plasma technique. The calculation of slag liquidus is performed using the FactSage 7.2^{TM} Equilib module. The density of the slag at 1773 K is calculated from a model based on slag structure [39]. Urbain model is used to determine the viscosity of the slag at 1773 K [39]. A pycnometer of 2 ml volume is used to determine the density of Al_2TiO_5 particle at room temperature. The density is then linearly extrapolated to 1773 K [40].

Table 6-1 Physical properties of slags and particles used for dissolution studies

Component	Al_2O_3 (wt pct)	CaO (wt pct)	SiO_2 (wt pct)	Liquidus/melting point (K)	Density (kg/m^3)	Viscosity (poise)
Slag 1	20	40	40	1613	2755	32
Slag 2	23.2	30.5	46.3	1703	2718	90
Slag 3	14.9	47.6	37.5	1651	2678	19
Al_2TiO_5	--	--	--	2133	3804	-

The slag is prefused in a platinum crucible of 5 mm height and 5 mm inner diameter. The crucible rests on a holder. This holder is spot welded to the thermocouple wires, the other end of the thermocouple is attached to the temperature controller. The mass of the particle is less than 1 wt pct of the mass of the slag in the crucible. A B type thermocouple is used to measure the temperature in the infra-red imaging furnace of the CSLM. This thermocouple is located at the bottom portion of the crucible holder. The temperature of the slag surface is different than the temperature at the bottom of the crucible, where the thermocouple is attached. It is important to note that during the dissolution reaction, the temperature is measured at the bottom of the crucible holder. However, the observation is made from a location which is anywhere between 1-3 mm above the bottom of the crucible holder. Therefore, it is required that the temperature at the crucible bottom should be calibrated to accommodate for the temperature difference of the two spatial locations. This calibration is done by using 99.5 pct assay iron discs. Three experiments are performed by measuring the difference between the melting point recorded by the CSLM and the melting point of pure iron at 1812 K. After the calibration is done, dissolution experiments are performed. For the dissolution experiments, time zero is chosen as the moment when CSLM temperature reaches the experimental temperature. A pre-determined heating schedule is used for the dissolution experiments. The system is heated rapidly from 423 K to 1673 K at the rate of 1000 K/min. From 1673 K to 1773 K, the system is heated at the rate of 100 K /min. After reaching 1773 K, the slag-particle system is held at this temperature until dissolution is complete. The dissolution process is recorded in the form of a video. To analyze the video, frames are carefully extracted using an open-source software called Virtual Dub Mod^{TM}. The extracted frames are analyzed manually by drawing a border around the particle to differentiate the particle from the slag using an open source software called ImageJ ^{TM}. An image of the dissolving particle in slag 3 at time zero is shown in Figure 6-1. The area within the boundary is measured. The area is assumed to be that of a sphere for simplification. The area is then converted to find the equivalent circular radius. The radius time data is used to analyze the dissolution kinetics further.

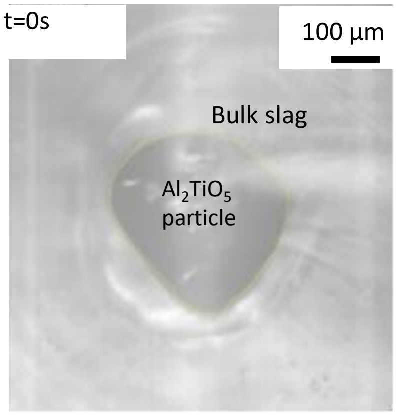

Figure 6-1 Representative image from the dissolution of a single Al_2TiO_5 particle in slag 3 at 1773 K

6.3 Thermodynamic modeling of the system

Construction of a phase diagram for the particle slag system gives an idea of the stable phases present in the system. An isothermal ternary phase diagram is constructed for the Al_2O_3-CaO-SiO_2-Al_2TiO_5 system using the FactSage 7.2 ™ with the application of the FACT-Oxid database. It is found that Al_2O_3 is the only stable phase for slag 1 and slag 2 while CaO.6Al_2O_3 and Al_2O_3 are the stable phases for slag 3. The composition of the interface can be estimated from the liquid slag saturated with aluminum titanate. The saturation composition of the slag at the interface is calculated from phase diagrams. Table 6-2 summarizes the bulk concentration, saturation concentration, and density of slags. The concentration of Al_2O_3 and TiO_2 in slag at saturation with aluminum titanate is higher than the concentration of alumina in the bulk slag. Based on the concentration gradient, Al_2O_3 and TiO_2 will diffuse from particle to the slag for all slag compositions.

Table 6-2 Bulk composition, saturation composition and density of slag 1, slag 2 and slag 3 at 1773 K

Slag/ constituents	Al_2O_3 (wt pct)	CaO (wt pct)	SiO_2 (wt pct)	TiO_2 (wt pct)	Density (kg/m^3)
Slag 1 bulk	20	40	40	0.0	2755
Slag 1 saturation	35.1	26.7	26.3	11.9	2526

Slag 2 bulk	23.2	30.5	46.3	0	2718
Slag 2 saturation	35.2	33.2	22.1	9.5	2594
Slag 3 bulk	14.9	47.6	37.5	0	2758
Slag 3 saturation	34.5	28.1	21.9	15.5	2449

6.4 Results and discussions

6.4.1 Dissolution rate

The dissolution rate of Al_2TiO_5 particles into the slag is expressed as the rate of decrease of the equivalent circular radius of solid particles with time. It is assumed that the particle has a spherical geometry. Figure 6-2 shows the changes in particle diameter with time in slags at 1773 K. In slag 1, the dissolution time for a particle of size 162 µm is 22 s. In slag 2, the dissolution time for a particle of radius 355 µm is 125 s. In slag 3, the dissolution time for Al_2TiO_5 particle of radius 311 µm is 10 s. The slope of the normalized radius versus time graph shows the rate of dissolution of the particle. The intercept is fixed at 1 so that a comparison of dissolution rate can be drawn for the three slags. The limitation with CSLM technique and the errors arising from measurement of particle size using CSLM is discussed in Appendix A2 and A3. From Figure 6-2, the slope for slag 1 is 0.0285 s^{-1}, that of slag 2 is 0.0084 $s^{-1,}$ and that of slag 3 is 0.0766 s^{-1}. From the calculated slopes, it is seen that the rate of dissolution of aluminum titanate follows the order: slag 3 > slag 1 > slag 2.

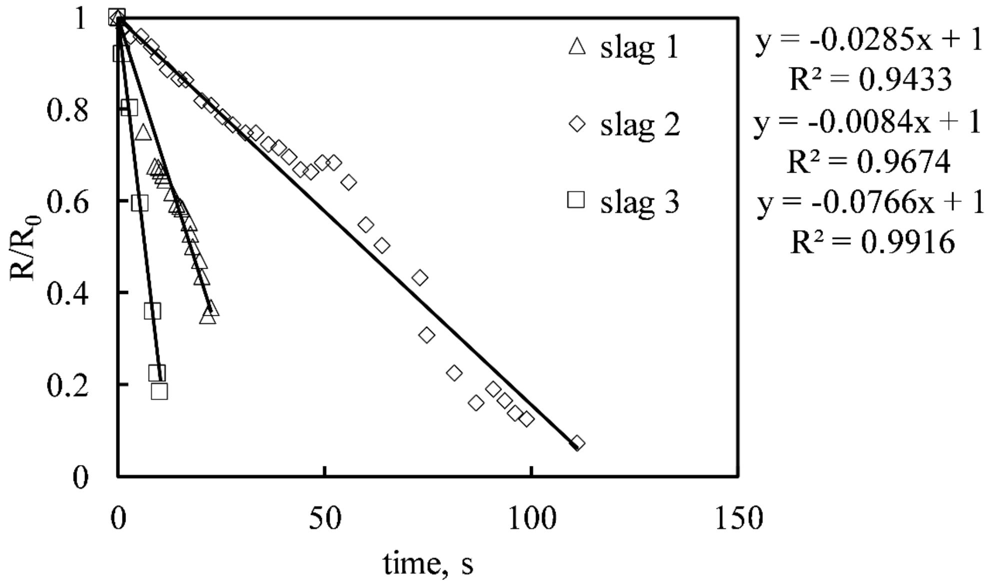

Figure 6-2 Dissolution rate of aluminum titanate particle in slag 1, slag 2 and slag 3

6.4.2 Determining mass transfer coefficient

In an earlier work by the authors [26, 35, 36], the SCM [41] was used to identify the rate-controlling mechanism for Al_2TiO_5 particle dissolution in slags. Using the boundary layer diffusion control model, diffusivity values of Al_2O_3 were calculated. The values were higher than those reported in the literature. The authors proposed that this disagreement is related to the model assumption for smaller particles in the Stoke's regime. Due to gas bubble generation and bursting during the in-situ dissolution, a stirring effect was provided by the gas bubbles and created local convection. Therefore, it is more relevant to calculate the mass transfer coefficient instead of converting the mass transfer coefficient to diffusivity. Yan et al. [42] calculated the mass transfer coefficient to incorporate the effect of particle rotation during dissolution. Their methodology enabled the authors to account for local convection; however, it cannot be applied in this work since there is no rotation observed.

For the current work, the mass transfer in the boundary layer can be written in equations 6-1 and 6-2.

$$\mathrm{j} = -(\mathrm{Km})\Delta\mathrm{C} \tag{6-1}$$

$$1 - \frac{\mathrm{R_C}}{\mathrm{R_0}} = \frac{(\mathrm{Km})\Delta\mathrm{C}}{\rho\mathrm{R_0}}\mathrm{t} \tag{6-2}$$

where j is the flux of aluminum titanate, Km is the mass transfer coefficient, ΔC denotes the concentration difference of the rate-limiting species (alumina) in bulk slag and a slag saturated with Al_2TiO_5. The ΔC value for Al_2O_3 is 336 kg/m^3 in slag 1, 288 kg/m^3 in slag 2 and 433 kg/m^3 in slag 3. R_c and R_0 are instantaneous and initial radii (m), t is the instantaneous time (s), $\rho_{particle}$ is the particle density (kg/m^3). Using the experimental CSLM, the radius of the particle is measured during dissolution. The slope of r/r0-1 versus t can be used to estimate the value of the mass transfer coefficient. Substituting the value of variables in equation 6-2, the mass transfer coefficient is calculated. Table 6-3 shows the value of the mass transfer coefficient estimated for the three slag compositions. The mass transfer coefficient for slag 2 is less than that of slag 1. The mass transfer coefficient is highest for slag 3. Monaghan and Chen [29] reported the dissolution of alumina particles in a 23.7 wt pct Al_2O_3 - 28.0 wt pct CaO - 48.3 wt pct SiO_2 slag at 1777 K. The slag composition used is similar in composition to the slag 2 used in the current work. This value is in reasonable agreement with the mass transfer coefficient calculated for slag 2 in the current work.

Table 6-3 Calculation of the mass transfer coefficient in slag 1, slag 2 and slag 3

	Slope	R_0, µm	ΔC-Al_2O_3, kg/m^3	Mass transfer coefficient, K_mx10^5 m/s
Slag 1	0.0283	131	336	4.2
Slag 2	0.0074	355	288	3.5
Slag 3	0.1147	311	430	31.4

6.4.3 Effect of slag basicity and viscosity

Figure 6-3 shows the effect of slag basicity on the mass transfer coefficient. The mass transfer coefficient increases with an increase in slag basicity. The basicity of a slag, defined as the ratio of calcium oxide to silicon oxide, is an indication of the structure of slag. Low basicity indicates that the silica chains in slag have more closed tetrahedron and less open space for movement of any species [39]. This indicates that species will have lower diffusivities and mass transfer coefficients.

Eyring relationship shows that the diffusivity in slag is inversely proportional to the viscosity of slag. Figure 6-4 shows the effect of slag viscosity on the dissolution rate in the three slags at 1773K. The rate of dissolution is found to increase with a decrease in slag viscosity. Therefore, the current results in an agreement with Eyring relationship and support that mass transfer in the boundary layer is the rate-determining step for dissolution of Al_2TiO_5 particles in the slags studied.

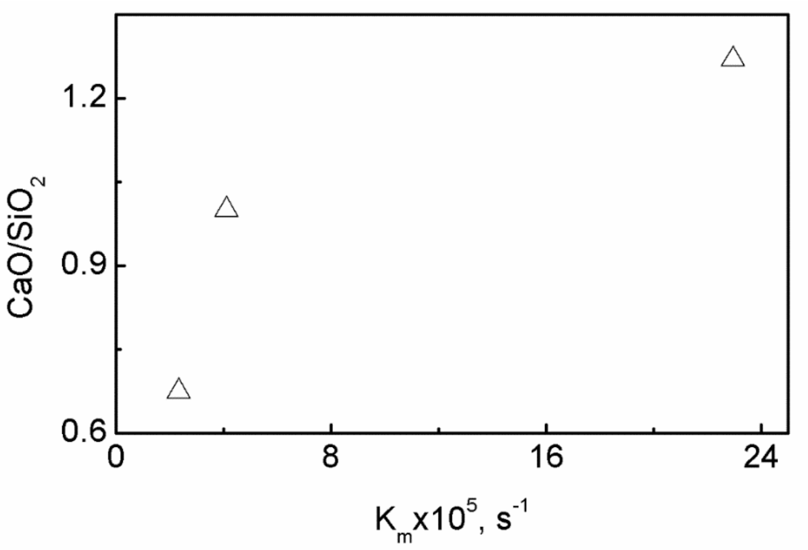

Figure 6-3 Effect of slag basicity on the mass transfer coefficient in slag 1, slag 2 and slag 3

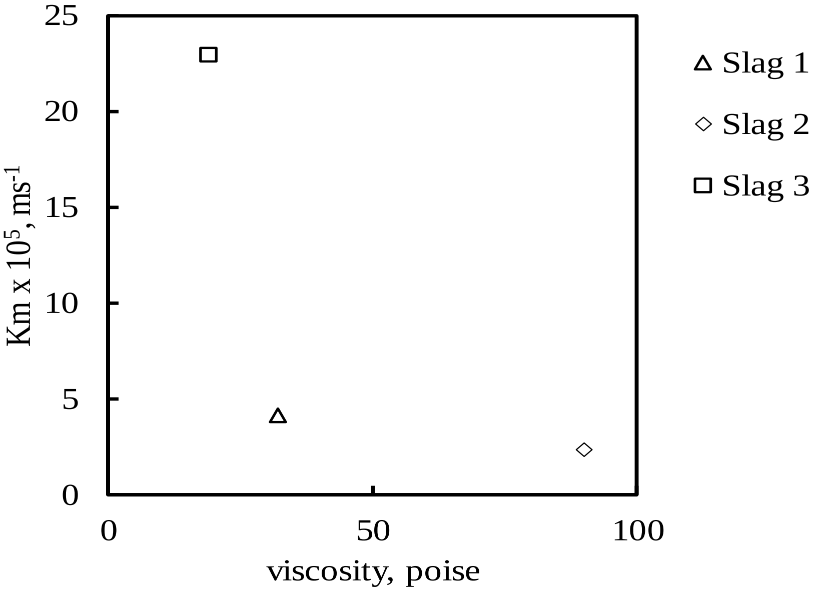

Figure 6-4 Effect of slag viscosity on the mass transfer coefficient of alumina in slags 1, 2 and 3

6.5 Conclusion

The in-situ dissolution of aluminum titanate inclusion is measured using a confocal scanning laser microscope. The effect of slag composition is studied by varying the slag composition at 20 wt pct alumina, 23.2 wt pct alumina and 14.9 wt pct alumina. The rate of dissolution increases with a decrease in slag viscosity. The mass transfer coefficient is approximately 10^{-5} ms^{-1} for slag1 and slag 2 while the mass transfer coefficient in slag 3 is one order of magnitude higher.

6.6 References

1. S. Basu, S. K. Choudhary, and N. U. Girase, ISIJ Int. **44**, 1653 (2004).

2. A. Karasangabo and C. Bernhard, J. Adhes. Sci. Technol. **26**, 1141 (2012).

3. J. Lee, S. Kim, M. Kang, and Y. Kang, in *AISTech 2019 — Proc. Iron Steel Technol. Conf.* (2019), pp. 2147–2154.

4. K. G. Rackers and B. G. Thomas, in *78th Steelmak. Conf. Proc.* (Nashville, 1995), pp. 723–734.

5. R. Wei, X. Lv, Z. Yue, and S. Xiang, Metall. Mater. Trans. B **48**, 733 (2017).

6. D. Wang, J. Liu, M. Jiang, F. Tsukihashi, and H. Matsuura, Int. J. Miner. Metall. Mater. **18**, 646 (2011).

7. K. H. SANDHAGE and G. J. YUREK, J. Am. Ceram. Soc. **71**, 478 (1988).

8. K. H. Sandhage and G. J. Yurek, J. Am. Ceram. Soc. **73**, 3633 (1990).

9. A. R. COOPER and W. D. KINGERY, J. Am. Ceram. Soc. **47**, 37 (1964).

10. S. Taira, K. Nakashima, and K. Mori, ISIJ Int. **33**, 116 (1993).

11. X. Yu, R. J. Pomfret, and K. S. Coley, Metall. Mater. Trans. B Process Metall. Mater. Process. Sci. **28**, 275 (1997).

12. Samaddar, B.N., W. D. Kingery, and Cooper Jr.A.R., J. Am. Ceram. Soc. **47**, 249 (1964).

13. H. Um, K. Lee, J. Choi, and Y. Chung, ISIJ Int. **52**, 62 (2012).

14. K. Sandhage and G. Yurek, J. Am. Ceram. Soc. **73**, 3643 (1990).

15. Z. S. Ren, X. J. Hu, X. M. Hou, X. X. Xue, and K. C. Chou, Int. J. Miner. Metall. Mater. **21**, 345 (2014).

16. S. Sridhar and A. W. Cramb, Metall. Mater. Trans. B **31**, 406 (2000).

17. S. H. Lee, C. Tse, K. W. Yi, P. Misra, V. Chevrier, C. Orrling, S. Sridhar, and A. W. Cramb, J. Non. Cryst. Solids **282**, 41 (2001).

18. J. H. Park, I. Jung, and H. Lee, ISIJ Int. **46**, 1626 (2006).

19. B. J. Monaghan and L. Chen, Ironmak. Steelmak. **33**, 323 (2006).

20. F. Verhaeghe, J. Liu, M. Guo, S. Arnout, B. Blanpain, and P. Wollants, Appl. Phys. Lett. **91**, 124104 (2007).

21. J. Liu, M. Guo, P. T. Jones, F. Verhaeghe, B. Blanpain, and P. Wollants, J. Eur. Ceram. Soc. **27**, 1961 (2007).

22. J. Liu, F. Verhaeghe, M. Guo, B. Blanpain, and P. Wollants, J. Am. Ceram. Soc. **90**, 3818 (2007).

23. X. Guo, M. Guo, Z. Sun, J. Van Dyck, B. Blanpain, and P. Wollants, in *Mater. Sci. Technol. Conf.* (2010), pp. 1739–1750.

24. S. Feichtinger, S. K. Michelic, Y. B. Kang, and C. Bernhard, J. Am. Ceram. Soc. **97**, 316 (2014).

25. S. Michelic, J. Goriupp, S. Feichtinger, Y. B. Kang, C. Bernhard, and J. Schenk, Steel Res. Int. **87**, 57 (2016).

26. M. Sharma, W. Mu, and N. Dogan, in *AISTech 2018* (2018), pp. 2601–2608.

27. M. Valdez, K. Prapakorn, A. W. Cramb, and S. Sridhar, Ironnmaking Steelmak. **29**, 47 (2002).

28. K. W. Yi, C. Tse, J. H. Park, M. Valdez, A. W. Cramb, and S. Sridhar, Scand. J. Metall. **32**, 177 (2003).

29. B. J. Monaghan and L. Chen, J. Non. Cryst. Solids **347**, 254 (2004).

30. A. B. Fox, M. E. Valdez, J. Gisby, R. C. Atwood, P. D. Lee, and S. Sridhar, ISIJ Int. **44**, 836 (2004).

31. B. J. Monaghan, S. A. Nightingale, L. Chen, and G. A. Brooks, in *Int. Conf. Molten Slags Fluxes Salts* (South Africa, 2004), pp. 585–594.

32. B. J. Monaghan and L. Chen, Steel Res. Int. **76**, 346 (2005).

33. B. J. Monaghan, L. Chen, and J. Sorbe, Ironmak. Steelmak. **32**, 258 (2005).

34. M. Sharma, H. A. Dabkowska, and N. Dogan, Steel Res. Int. 1 (2018).

35. M. Sharma, W. Mu, and N. Dogan, in *AISTech* (2018).

36. M. Sharma and N. Dogan, in *Adv. Real Time Imaging II Cut. Edge Tech. Mater. Sci. Stud.*, edited by Jinichiro Nakano, P. C. Pistorious, C. Tamerler, H. Yasuda, Z. Zhang, N. Dogan, W. Wang, N. Saito, and B. Webler (Springer, 2019), pp. 119–127.

37. M. Sharma, W. Mu, and N. Dogan, JOM **70**, 1220 (2018).

38. M. Allibert, H. Gaye, J. Geisler, D. Janke, B. J. Keene, D. Kirner, M. Kowalski, J. Lehmann, K. C. Mills, D. Neuschutz, R. Parra, C. Saint Jours, P. J. Spencer, M. Susa, M. Tmar, and E. Woermann, in *Slag Atlas*, edited by V. D. E. (VDEh), 2nd ed. (Dusseldorf, 1995), pp. 345–347.

39. D. Kim, H. Kim, H. Kim, J. Namkung, I. Kim, and S. Choi, **2**, 154 (2014).

40. O. Levenspiel, *Chemical Reaction Engineering*, Third (John Wiley and Sons, New York, 1999).

41. P. Yan, B. A. Webler, P. C. Pistorius, and R. J. Fruehan, Metall. Mater. Trans. B **46**, 2414 (2015).

Chapter 7
Conclusion

The objective of this project was to establish a fundamental understanding of dissolution behavior of Ti containing inclusions in slags relevant to secondary steelmaking. The variables studied in this project were temperature, the composition of inclusions and slag. The in-situ observations from CSLM were used in conjunction with SEM to identify the reaction mechanism of Ti-containing inclusions. On the basis of this study, it is possible to draw the following conclusions.

1. The optical floating zone method is a promising technique in comparison to the sintering technique concerning high purity and less porosity of the particles for studying in situ dissolution using CSLM. The preparation of complex oxide particle for dissolution study is a novel use of the OFZM. This finding is represented in Chapter 3, achieving the first objective of this thesis.

2. Chapter 3, 4, and 5 achieved the second and third objectives of this study and offered novel kinetic data on the dissolution of Ti-containing inclusions in the steelmaking slags observed in-situ by CSLM. The comparison of kinetic data for Al_2O_3 and Al_2TiO_5 particles shows that the Al_2O_3 particles dissolve slower than the Al_2TiO_5 particles than TiO_2 particles. The dissolution time decreased with an increase in temperature.

3. The dissolution of Al_2O_3 particles has been found to be mass transfer controlled, and this finding is in agreement with previous studies.

4. Chapter 5 achieved the fourth objective of this thesis. The proposed dissolution mechanism of Ti-containing inclusion is as follows: Al_2TiO_5 dissociated to Al_2O_3, Ti_3O_4, and O_2. The Al_2O_3 and Ti_3O_5 dissolved in slag while the O_2 evolved during dissolution. Based on the characterization of the particle-slag interface, the diffusion of Al_2O_3 through the boundary layer is the rate-controlling step.

5. The mass transfer coefficient of aluminum titanate increased with a decrease in slag viscosity. This finding is provided in Chapter 6 and confirms that the rate-controlling step is diffusion through the boundary layer.

Although the dissolution rate and mechanism of Al_2TiO_5 particles were successfully studied in this work, there are certain aspects of the measurement and interpretation of the kinetic data which remain unclear in the present study. The following topics are suggested as future research areas.

1. The OFZM method is a new application for the preparation of microparticles. TiO_2 and Al_2TiO_5 were prepared successfully. It needs to be tested to make other critical particles such as $MgAl_2O_4$, $CaO.2Al_2O_3$, and $CaO.6Al_2O_3$. During this thesis work, it was realized that the effect particle shape is essential in studying the dissolution of microparticles. There is a need to find routes for the preparation of particles with controlled shape and size.
2. The determination of the dissolution mechanism of TiO_2 remains as future work for the authors. The interface of TiO_2 particle and slag needs to be examined to identify the composition gradients in the bulk slag, at the interface, and within the particle.

3. In the current work, it was realized that the shrinking core model is insufficient to model the dissolution kinetics especially for Al_2TiO_5 particle representing complex inclusions. The CSLM data was scattered in comparison to predictions by the shrinking core model; it is difficult to distinguish between chemical reaction control and mass transport control mechanisms. A stirring effect is provided by the gas evolved during dissolution. The effect of stirring needs to be incorporated into the model. A more rigorous multicomponent diffusion kinetic model is needed to illustrate the dissolution mechanism accurately.

4. The effect of MgO as a slag constituent needs to be explored. A small change in MgO content affects the slag properties by a significant amount. This effect needs to be studied by using the confocal scanning laser microscopy.

References

1 D. Wang, J. Liu, M. Jiang, F. Tsukihashi, and H. Matsuura: *Int. J. Miner. Metall. Mater.*, 2011, vol. 18, pp. 646–51.

2 Z.S. Ren, X.J. Hu, X.M. Hou, X.X. Xue, and K.C. Chou: *Int. J. Miner. Metall. Mater.*, 2014, vol. 21, pp. 345–52.

3 M. Vedani and A. Mannucci: *ISIJ Int.*, 2008, vol. 42, pp. 1520–6.

4 W. Choi, H. Matsuura, and F. Tsukihashi: *ISIJ Int.*, 2011, vol. 51, pp. 1951–6.

5 H. Cui, Y. Bao, M. Wang, and W. Wu: *Int. J. Miner. Metall. Mater.*, 2010, vol. 17, pp. 154–8.

6 C. Wang, N.T. Nuhfer, and S. Sridhar: *Metall. Mater. Trans. B Process Metall. Mater. Process. Sci.*, 2010, vol. 41, pp. 1084–94.

7 C. Wang, N. Verma, Y. Kwon, W. Tiekink, N. Kikuchi, and S. Sridhar: *ISIJ Int.*, 2011, vol. 51, pp. 375–81.

8 A. Pardo, M.C. Merino, M. Carboneras, A.E. Coy, F. Viejo, R. Arrabal, and J.A. Munoz: *EUROCORR 2004 - Eur. Corros. Conf. Long Term Predict. Model. Corros.*, 2004, pp. 1–8.

9 H. po WANG, L. feng SUN, B. PENG, and M. fa JIANG: *J. Iron Steel Res. Int.*, 2013, vol. 20, pp. 70–4.

10 J. Burja, F. Tehovnik, J. Lamut, and M. Knap: *Mater. Tehnol.*, 2013, vol. 47, pp. 217–22.

11 R.C. Nunnington and N. Sutcliffe: in *2001 Electric Furnace Conference Proceedings*, 2001, pp. 1–39.

12 F. Tehovnik, J. Burja, B. Arh, and M. Knap: *Metalurgija*, 2015, vol. 54, pp. 371–4.

13 S. Basu, S.K. Choudhary, and N.U. Girase: *ISIJ Int.*, 2004, vol. 44, pp. 1653–60.

14 P. Kaushik, R. Lule, G. Castillo, J.C. Delgado, F. Lopez, C. Perim, G. Pigatti, B. Henriques, F. Barbosa, and A. Nascimento: *Iron Steel Technol.*, 2016, vol. 13, pp. 168–85.

15 D. Wang, M. Jiang, H. Matsuura, and F. Tsukihashi: *Steel Res. Int.*, 2014, vol. 85, pp. 16–25.

16 P. Rocabois, J. Lehmann, C. Gatellier, and J.P. Teres: *Ironmak. Steelmak.*, 2003, vol. 30_ _, pp. 95–9.

17 B. Deo and R. Boom: in *Fundamentals of Steelmaking Metallurgy*, 1993, pp. 216–53.

18 E. Pretorius and H. Oltmann: *EAF Fundamentals*, 2010.

19 B. Deo and R. Boom: in *Fundamentals of Steelmaking Metallurgy*, 1993, pp. 146–60.

20 A. Ghosh: in *Secondary Steelmaking: Principles and Applications*, 1st Ed., CRC Press, London, 2001, p. 1.

21 W. Association: Overview of the steelmaking process, https://steeluniversity.lms.crossknowledge.com/data/content/Final/1284/222D9A74-6437-DDE4-3B95-F0C89DC9DC28/index.html#gotoExercise=1332, (accessed 2 June 2016).

22 R.J. Fruehan and I. and S.S. of AIME.: *Ladle Metallurgy Principles and Practices*, Iron and Steel Society, [Warrendale, PA], 1985.

23 A. Ghosh: *Secondary Steelmaking Principles and Applications*, CRC Press, 2001.

24 A. Ghosh: *Secondary Steelmaking: Principles and Applications*, CRC Press, 2000.

25 T. Emi: in *Casting Volume*, 2003, pp. 1–58.

26 Paul K Trojan: in *ASM Handbook Vloume 15 Casting*, ASM International, 1988, pp. 90–1.

27 H.M. Pielet and D. Bhattacharya: *Metall. Trans. B*, 1984, vol. 15, pp. 547–62.

28 L. Holappa: *Steel Res. Int.*, 2010, vol. 81, pp. 869–74.

29 F. Oeters: in *Metallurgy of steelmaking*, 1994, p. 55.

30 A. Ghosh and A. Chaterjee: *Ironmaking and Steelmaking: Theory and Practice*, PHI Learning, New Delhi, 2011.

31 K. Sasai and Y. Mizukami: *ISIJ Int.*, 2008, vol. 41, pp. 1331–9.

32 D. Park, I. Jung, P. Rhee, and H. Lee: *ISIJ Int.*, 2004, vol. 44, pp. 1669–78.

33 S. Sridhar and H.Y. Sohn: in *Fundamentals of Metallurgy*, S. Seetharaman, ed., Woodhead Publishing, 2005, pp. 270–349.

34 K. Tshilombo: *Int. J. Miner. Metall. Mater.*, 2010, vol. 17, pp. 28–31.

35 M. Lind and L. Holappa: *Metall. Mater. Trans. B Process Metall. Mater. Process. Sci.*, 2010, vol. 41, pp. 359–66.

36 K. Ahlborg, R.J. Fruehan, M.S. Potter, S.R. Badger, and G.S. Casuccio: in *ISSTech*, 2003, pp. 177–94.

37 H. Matsuura, C. Wang, G. Wen, and S. Sridhar: *ISIJ Int.*, 2007, vol. 47, pp. 1265–74.

38 J.H. Schade, R.J.O. Malley, F.L. Kemeny, Y. Sahai, and D.J. Zachariaas: in *Casting Volume*, 2003, pp. 1–70.

39 K.G. Rackers and B.G. Thomas: in *78th Steelmaking Conference Proceedings*, vol. 78, 1995, pp. 723–34.

40 A.W. Cramb and R.L. Maddalena: in *Refractory Materials*, 11th edn., AISE Steel Foundation, Pittsburgh, 2003, pp. 2–5.

41 J. Lee, S. Kim, M. Kang, and Y. Kang: in *AISTech 2019 — Proceedings of the Iron & Steel Technology Conference*, 2019, pp. 2147–54.

42 Y. Gao and K. Sorimachi: *ISIJ Int.*, 1993, vol. 33, pp. 291–7.

43 L. feng ZHANG: *J. Iron Steel Res. Int.*, 2006, vol. 13, pp. 1–8.

44 J. Poirier: *Metall. Res. Technol.*, 2015, vol. 112, p. 410.

45 H. Abdeyazdan, N. Dogan, M.A. Rhamdhani, M.W. Chapman, and B.J. Monaghan: *Metall. Mater. Trans. B*, 2014, vol. 46B, pp. 208–19.

46 B.G. Thomas: *Iron Steel Technol.*, 2006, vol. 3, pp. 847–61.

47 R. Dekkers and K.U. Leuven: 2002.

48 A. Karasangabo and C. Bernhard: *J. Adhes. Sci. Technol.*, 2012, vol. 26, pp. 1141–56.

49 L. Wang, P.C. Hayes, and H. Lee: *ISIJ Int.*, 1996, vol. 36, pp. 7–16.

50 K. Matsumoto, A. Okayama, T. Nakaoka, and S. Taniguchi: in *ICS PRoceedings*, 2005, pp. 609–14.

51 J.-Y. Choi and H.-G. Lee: *ISIJ Int.*, 2003, vol. 43, pp. 1348–55.

52 A. Harada, G. Miyano, N. Maruoka, H. Shibata, and S. Kitamura: *ISIJ Int.*, 2014, vol. 54, pp. 2230–8.

53 V. Stahleisen, M. Allibert, and V.D. Eisenhüttenleute: in *Slag Atlas*, Verlag Stahleisen, 1995, p. 464.

54 S.H. Lee, C. Tse, K.W. Yi, P. Misra, V. Chevrier, C. Orrling, S. Sridhar, and A.W. Cramb: *J. Non. Cryst. Solids*, 2001, vol. 282, pp. 41–8.

55 B.J. Monaghan and L. Chen: *Steel Res. Int.*, 2005, vol. 76, pp. 346–52.

56 B.J. Monaghan and L. Chen: *J. Non. Cryst. Solids*, 2004, vol. 347, pp. 254–61.

57 S. Michelic, J. Goriupp, S. Feichtinger, Y.B. Kang, C. Bernhard, and J. Schenk: *Steel Res. Int.*, 2016, vol. 87, pp. 57–67.

58 M. Valdez, K. Prapakorn, A.W. Cramb, and S. Sridhar: *Ironnmaking Steelmak.*,

2002, vol. 29, pp. 47–52.

59 J. Liu, F. Verhaeghe, M. Guo, B. Blanpain, and P. Wollants: *J. Am. Ceram. Soc.*, 2007, vol. 90, pp. 3818–24.

60 F. Verhaeghe, J. Liu, M. Guo, S. Arnout, B. Blanpain, and P. Wollants: *Appl. Phys. Lett.*, 2007, vol. 91, p. 124104.

61 S. Sridhar and A.W. Cramb: *Metall. Mater. Trans. B*, 2000, vol. 31, pp. 406–10.

62 A.R. COOPER and W.D. KINGERY: *J. Am. Ceram. Soc.*, 1964, vol. 47, pp. 37–43.

63 S.A. Nightingale, G.A. Brooks, and B.J. Monaghan: *Metall. Mater. Trans. B*, 2005, vol. 36, pp. 453–61.

64 H. Um, K. Lee, J. Choi, and Y. Chung: *ISIJ Int.*, 2012, vol. 52, pp. 62–7.

65 Samaddar, B.N., W.D. Kingery, and Cooper Jr.A.R.: *J. Am. Ceram. Soc.*, 1964, vol. 47, pp. 249–54.

66 S. Taira, K. Nakashima, and K. Mori: *ISIJ Int.*, 1993, vol. 33, pp. 116–23.

67 X. Yu, R.J. Pomfret, and K.S. Coley: *Metall. Mater. Trans. B Process Metall. Mater. Process. Sci.*, 1997, vol. 28, pp. 275–9.

68 K.H. Sandhage and G.J. Yurek: *J. Am. Ceram. Soc.*, 1990, vol. 73, pp. 3633–42.

69 B.J. Monaghan, S.A. Nightingale, L. Chen, and G.A. Brooks: in *International Conference on Molten Slags Fluxes and Salts*, South Africa, 2004, pp. 585–94.

70 H. Soll-Morris, C. Sawyer, Z.T. Zhang, G.N. Shannon, J. Nakano, and S. Sridhar: *Fuel*, 2009, vol. 88, pp. 670–82.

71 J. Liu, M. Guo, P.T. Jones, F. Verhaeghe, B. Blanpain, and P. Wollants: *J. Eur. Ceram. Soc.*, 2007, vol. 27, pp. 1961–72.

72 J.H. Park, I. Jung, and H. Lee: *ISIJ Int.*, 2006, vol. 46, pp. 1626–34.

73 K.W. Yi, C. Tse, J.H. Park, M. Valdez, A.W. Cramb, and S. Sridhar: *Scand. J. Metall.*, 2003, vol. 32, pp. 177–84.

74 A.B. Fox, M.E. Valdez, J. Gisby, R.C. Atwood, P.D. Lee, and S. Sridhar: *ISIJ Int.*, 2004, vol. 44, pp. 836–45.

75 B.J. Monaghan, L. Chen, and J. Sorbe: *Ironmak. Steelmak.*, 2005, vol. 32, pp. 258–64.

76 S. Feichtinger, S.K. Michelic, Y.B. Kang, and C. Bernhard: *J. Am. Ceram. Soc.*, 2014, vol. 97, pp. 316–25.

77 J.H. Park, J.G. Park, D.J. Min, Y.E. Lee, and Y.B. Kang: *J. Eur. Ceram. Soc.*,

2010, vol. 30, pp. 3181–6.

78 X. Guo, M. Guo, Z. Sun, J. Van Dyck, B. Blanpain, and P. Wollants: in *Materials Science and Technology Conference*, 2010, pp. 1739–50.

79 Marvin Misnki: Marvin Minsky, https://web.media.mit.edu/~minsky/papers/ConfocalMemoir.html, (accessed 28 March 2015).

80 B.J. Monaghan, L. Chen, and J. Sorbe: *Ironmak. Steelmak.*, 2005, vol. 32, pp. 258–64.

81 M. Tanaka, M. Haniu, K.T. Yasunobu, and T.R. Norton: *Amino Acid Sequence of the Anthopleura Xanthogrammica Heart Stimulant, Anthopleurin A*, vol. 16, Verlag Stahleisen mbH, 1977.

82 B.J. Monaghan and L. Chen: *Ironmak. Steelmak.*, 2006, vol. 33, pp. 323–30.

83 F. Oeters: *Metallurgy of Steelmaking*, 1994.

84 O. Levenspiel: *Chemical Reaction Engineering*, vol. 19, Third., John Wiley and Sons, New york, 1999.

85 J. Liu, F. Verhaeghe, M. Guo, B. Blanpain, and P. Wollants: *J. Am. Ceram. Soc.*, 2007, vol. 90, pp. 3818–24.

86 F. Verhaeghe, B. Blanpain, and P. Wollants: *Model. Simul. Mater. Sci. Eng.*, 2008, vol. 16, pp. 1–18.

87 F. Verhaeghe, S. Arnout, B. Blanpain, and P. Wollants: *Phys. Rev. E - Stat. Nonlinear, Soft Matter Phys.*, 2006, vol. 73, pp. 1–10.

88 P. Yan, B.A. Webler, P.C. Pistorius, and R.J. Fruehan: *Metall. Mater. Trans. B*, 2015, vol. 46, pp. 2414–8.

89 J. Liu, F. Verhaeghe, M. Guo, B. Blanpain, and P. Wollants: *J. Am. Ceram. Soc.*, 2007, vol. 90, pp. 3818–24.

90 A. de Pretis, F. Ricciardiello, and O. Sbaizero: *J. Mater. Sci. Lett.*, 1985, vol. 4, pp. 9–12.

91 B.J. Monaghan, S.A. Nightingale, L. Chen, and G.A. Brooks: 2004, pp. 585–94.

92 S.H. Lee, C. Tse, K.W. Yi, P. Misra, V. Chevrier, C. Orrling, S. Sridhar, and a. W. Cramb: *J. Non. Cryst. Solids*, 2001, vol. 282, pp. 41–8.

Chapter 8
Appendices

8.1 Appendix A1 - Inclusion dissolution literature

The inclusion dissolution literature from CSLM studies is compiled in the form of a table. They provide an idea of the different slag compositions and temperature used for studying the dissolution phenomenon.

Table 8-1 Dissolution data for Al_2O_3 particle in different slag systems using CSLM

Particle Diameter (µm)	Slag Composition (Wt. %)	Viscosity (Poise)	Diffusivity $*10^{-10}$ (m^2/s)	Ref
138 µm in 2112 s at 1430 °C	$33.4CaO-19.5Al_2O_3-39.5SiO_2-7.3MgO$	48	Not provided	[61]
122 µm in 708 s at 1480 °C	$33.4CaO-19.5Al_2O_3-39.5SiO_2-7.3MgO$	32	Not provided	[61]
142 µm in 1200 s at 1480 °C	$33.4CaO-19.5Al_2O_3-39.5SiO_2-7.3MgO$	32	Not provided	[61]
112 µm in 328 s at 1530 °C	$33.4CaO-19.5Al_2O_3-39.5SiO_2-7.3MgO$	22	Not provided	[61]
84 µm in 307 s at 1530 °C	$33.4CaO-19.5Al_2O_3-39.5SiO_2-7.3MgO$	22	Not provided	[61]
96 µm in 203 s at 1550 °C	$33.4CaO-19.5Al_2O_3-39.5SiO_2-7.3MgO$	19	Not provided	[61]
260 µm in 700 s at 1450 °C	$48.4CaO-48.9Al_2O_3-1.5SiO_2-0.5MgO$	12	Not Provided	[54]
260 µm in 380 s at 1470 °C	$48.4CaO-48.9Al_2O_3-1.5SiO_2-0.5MgO$	10	Not Provided	[54]
260 µm in 220 s at 1500 °C	$48.4CaO-48.9Al_2O_3-1.5SiO_2-0.5MgO$	8	Not Provided	[54]

200 µm in 160 s at 1450 °C	$46.3CaO-46.7Al_2O_3--1.3SiO_2-5.6MgO$	10	Not Provided	[54]
200 µm in 70 s at 1470 °C	$46.3CaO-46.7Al_2O_3--1.3SiO_2-5.6MgO$	8	Not Provided	[54]
200 µm in 40 s at 1500 °C	$46.3CaO-46.7Al_2O_3--1.3SiO_2-5.6MgO$	7	Not Provided	[54]
200 µm in 130 s at 1450 °C	51.5CaO-46.6Al2O3-1.3SiO2-0.5MgO	10	Not Provided	[54]
200 µm in 90 s at 1470 °C	51.5CaO-46.6Al2O3-1.3SiO2-0.5MgO	9	Not Provided	[54]
200 µm in 70 s at 1500 °C	51.5CaO-46.6Al2O3-1.3SiO2-0.5MgO	7	Not Provided	[54]
220 µm in 225 s at 1470-1530 °C	$33.4CaO-19.5Al_2O_3-39.5SiO_2-7.3MgO$	30	Not Provided	[58]
220 µm in 225 s at 1470-1530 °C	$36.0CaO-21.0Al_2O_3-42.0SiO_2-0.4MgO$	48	Not Provided	[58]
180 µm in 80 s at 1470-1530 °C	$59.0CaO-36.0Al_2O_3-5.0SiO_2$	6	Not Provided	[58]
500 µm in 3100 s at 1400 °C	$22.4CaO-15.3Al_2O_3-62.4SiO_2$	617	Not Provided	[70]
500 µm in 1400s at 1400 °C	$23.2CaO-14.4Al_2O_3-56.7SiO_2-5.8FeOx$	128		
500 µm in 800 s at 1400 °C	$23.3CaO-13.3Al_2O_3-54.2SiO_2-9.2FeOx$	59		
400 µm in 1700 s at 1600 °C	$28.1CaO-37.4Al_2O_3-28.1SiO_2-6.4MgO$	13	1.45	[57]
400 µm in 80 s at 1600 °C	$37.0CaO-37.0Al_2O_3-18.5SiO_2-7.5MgO$	7	0.04	[57]
400 µm in at 1600 °C	$46.0CaO-27.6Al_2O_3-18.4SiO_2-8.0MgO$	5	14.5	[57]
400 µm in 40 s at 1600 °C	$57.2CaO-19.1Al_2O_3-19.1SiO_2-4.6MgO$	3	19.4	[57]

400 µm at 1600 °C	$33.6CaO\text{-}16.8Al_2O_3\text{-}33.6SiO_2\text{-}16MgO$	7	33.8	[57]
100 µm in 1750 s at 1504 °C	$16.3CaO\text{-}19.3Al_2O_3\text{-}64.5SiO_2$	1783	0.19	. [56,69, 80]
100 µm in 1100 s at 1550 °C	$16.3CaO\text{-}19.3Al_2O_3\text{-}64.5SiO_2$	1039	0.15	[56,69, 80]
100 µm in 150 s at 1577 °C	$16.3CaO\text{-}19.3Al_2O_3\text{-}64.5SiO_2$	767	1.10	[56,69, 80]
100 µm in 600 s at 1477 °C	$28.0CaO\text{-}23.7Al_2O_3\text{-}48.3SiO_2$	164	0.99	[56,69, 80]
100 µm in 200 s at 1504 °C	$28.0CaO\text{-}23.7Al_2O_3\text{-}48.3SiO_2$	127	1.62	[56,69, 80]
100 µm in 50 s at 1554 °C	$28.0CaO\text{-}23.7Al_2O_3\text{-}48.3SiO_2$	84	1.60	[56,69, 80]
500 µm in 4311 s at 1470 °C	$29.7CaO\text{-}24.1Al_2O_3\text{-}46.2SiO_2$	132	0.25	[59]
500 µm in 3712 s at 1500 °C	$29.7CaO\text{-}24.1Al_2O_3\text{-}46.2SiO_2$	100	0.28	[59]
500 µm in 2015 s at 1550 °C	$29.7CaO\text{-}24.1Al_2O_3\text{-}46.2SiO_2$	65	0.34	[59]
500 µm in 1268 s at 1600 °C	$29.7CaO\text{-}24.1Al_2O_3\text{-}46.2SiO_2$	43	0.42	[59]
500 µm in 620 s at 1630 °C	$29.7CaO\text{-}24.1Al_2O_3\text{-}46.2SiO_2$	34	0.84	[59]
200 µm in 580 s at 1450 °C	$48.4CaO\text{-}48.9Al_2O_3\text{-}0.5MgO$	11	Not Provided	[73]
200 µm in 260 s at 1470 °C	$48.4CaO\text{-}48.9Al_2O_3\text{-}0.5MgO$	9	Not Provided	[73]
200 µm in 180 s at 1500 °C	$48.4CaO\text{-}48.9Al_2O_3\text{-}0.5MgO$	8	Not Provided	[73]
200 µm in 580 s at 1450 °C	$51.5CaO\text{-}46.6Al_2O_3\text{-}0.5MgO$	9	Not Provided	[73]
200 µm in 90 s at 1470 °C	$51.5CaO\text{-}46.6Al_2O_3\text{-}0.5MgO$	8	Not Provided	[73]

200 µm in 70 s at 1500 °C	$51.5CaO-46.6Al_2O_3-0.5MgO$	7	Not Provided	[73]

Table 8-2. Dissolution data for MgO in different slag systems using CSLM

Particle Diameter (µm)	Slag Composition (Wt. %)	Viscosity (Poise)	Diffusivity (m^2/s)	Ref
400 µm in 570 s at 1450 °C	$48.4CaO-48.9 Al_2O_3-0.5MgO$	11	Not Provided	[73]
400 µm in 260 s at 1470 °C	$48.4CaO-48.9 Al_2O_3-0.5MgO$	9	Not Provided	
400 µm in 180 s at 1500 °C	$48.4CaO-48.9 Al_2O_3-0.5MgO$	8	Not Provided	
400 µm in 3000 s at 1450 °C	$46.3CaO-46.7 Al_2O_3-5.6MgO$	9	Not Provided	
400 µm in 1000 s at 1500 °C	$46.3CaO-46.7 Al_2O_3-5.6MgO$	7	Not Provided	
400 µm in 400 s at 1550 °C	$46.3CaO-46.7 Al_2O_3-5.6MgO$	5	Not Provided	
400 µm in 6000 s at 1500 °C	$29.7CaO-24.1Al_2O_3-46.2SiO_2$	100	Not Provided	[71]
400 µm in 3400 s at 1600 °C	$29.7CaO-24.1Al_2O_3-46.2SiO_2$	43	Not Provided	
400 µm in 4000 s at 1500 °C	$29.9CaO-23.5Al_2O_3-39.3SiO_2-7.3MgO$	35	Not Provided	
400 µm in 5700 s at 1600 °C	$29.9CaO-23.5Al_2O_3-39.3SiO_2-7.3MgO$	17	Not Provided	
300 µm at 1550 °C	$43.3CaO-5.0Al_2O_3-51.3SiO_2$	23	Not Provided	[72]
300 µm at 1550 °C	$48.7CaO-5.0Al_2O_3-46.3SiO_2$	13	Not Provided	

300 µm at 1550 °C	$43.5CaO-14.9Al_2O_3-41.5SiO_2$	19	Not Provided	
300 µm at 1550 °C	$38.4CaO-24.9Al_2O_3-36.7SiO_2$	24	Not Provided	
300 µm at 1550 °C	$33.2CaO-34.9Al_2O_3-31.8SiO_2$	25	Not Provided	
300 µm at 1550 °C	$53.4CaO-5.0Al_2O_3-41.6SiO_2$	9	Not Provided	

Table 8-3. Dissolution data for $MgAl_2O_4$ in different slag systems using CSLM

Particle Diameter (µm)	Slag Composition (Wt. %)	Viscosity (Poise)	Diffusivity $*10^{-10}$ (m^2/s)	Ref
80 µm in 990 s at 1477 °C	$16.3CaO-19.3Al_2O_3-64.5SiO_2$	1783	0.76	[80]
80 µm in 110 s at 1504 °C	$16.3CaO-19.3Al_2O_3-64.5SiO_2$	1783	0.76	[80]
80 µm in 30 s at 1532 °C	$16.3CaO-19.3Al_2O_3-64.5SiO_2$	1783	0.76	[80]
80 µm in 80 s at 1504 °C	$16.3CaO-19.3Al_2O_3-64.5SiO_2$	1783	0.76	[82]
80 µm in 45 s at 1504 °C	$22.1CaO-21.5Al_2O_3-56.4SiO_2$	413	1.50	[82]
80 µm in 30 s at 1504 °C	$28.0CaO-23.7Al_2O_3-48.3SiO_2$	127	2.22	[82]

Table 8-4. Dissolution data for SiO_2 in different slag systems using CSLM

Particle Diameter (µm)	Slag Composition (Wt. %)	Viscosity (Poise)	Diffusivity $*10^{-10}$ (m^2/s)	Ref
350 µm in 235 s at 1450 °C	$34.1CaO-10.6Al_2O_3-54.6SiO_2$	160	0.44	[76]
350 µm in 110 s at 1450 °C	$38.3CaO-10.6Al_2O_3-50.5SiO_2$	84	0.85	[76]
350 µm in 95 s at 1450 °C	$36.4CaO-26.5Al_2O_3-37.1-SiO_2$	60	0.60	[76]

350 µm in 85 s at 1450 °C	$38.8CaO-18.9Al_2O_3$ $-42.3SiO_2-$	62	1.8	[76]
350 µm in 36 s at 1450 °C	$43.7CaO-10.4Al_2O_3-45.3SiO_2$	43	2.4	[76]
350 µm in 34 s at 1450 °C	$46.6CaO-10.8Al_2O_3-42.8SiO_2$	32	0.38	[76]

8.2 Appendix A2 - Limitations of CSLM technique for inclusion dissolution

The CSLM poses certain limitations and challenges regarding inclusion dissolution studies. The slag needs to be free of transition elements such as Fe, Mn, Cr, and Ti. These elements hinder in situ observation of the process and limit the visibility of the phenomenon being recorded [71,91]. This constrains the scope of CSLM to relevant slag compositions encountered in the steelmaking process.

Another factor is the size of the particle that can be clearly observed in the CSLM. From preliminary experience, the equivalent particle diameter should be in the range of 50-1000 µm. This depends on the chemistry of particle and slag under investigation. In contrast, the size of real inclusions, which are of interest to steelmakers is in the range of 2-5 µm.

The dissolution studies with the current system are not genuinely isothermal. The system is heated at a very rapid rate from room temperature to steelmaking temperature. Although it would be safe to assume that the dissolution is isothermal, in the truest of sense, it is not. This sets a limitation to the size of the particle, specially in case of fast dissolving particles. In such a case, the particle reacts with the slag before reaching the experimental temperature, which might lead to a different reaction path than what would be. This limitation brings a tradeoff with the amount and size of an inclusion particle that is allowed in an experiment to make accurate measurements. Ideally, the amount of particle should be less than 1 wt pct of the slag [92].

The particles used for inclusion dissolution studies are obtained by crushing bigger irregular particles. The shape of the particle during the experiment is uncontrolled and mostly non-spherical in shape. However, when the kinetic analysis is done equations based on an SCM, the particle is assumed to be a sphere for the sake of simplicity. The effect of particle shape is studied by comparing the rate of change in the size of irregular particles and spherical particles. The three sets of spherical data used, named 'spherical' in the legend is obtained from work by Liu et al. [59], shown in Figure 8-1. The experimental data for irregular-1 and irregular-2 in for alumina particles were obtained from our work at McMaster University. The average dR/dt for Spherical-1, Spherical-2 and Spherical-3 case is 0.20, 0.19 and 0.13 µm/s while the average dR/dt for irregular -1 and irregular -2 is 0.43 and 0.58 µm/s. The rate of change in size for dense spherical particles is lower than that in case of dense irregular particle. In the case of dissolution of spherical particles, the rotation of these particles is either negligible or does not exist. Therefore, the rate of change in particle size is relatively steady. The average rate of change in size for spherical alumina particles is 2 to 3 times slower than the average rate of irregular alumina particles. This is most likely due to the rotation, which causes local convection and enhances the rate of transfer of mass from the particle to the slag. Thus, the controlled spherical shape of particles is important in proper kinetic analysis of CSLM data.

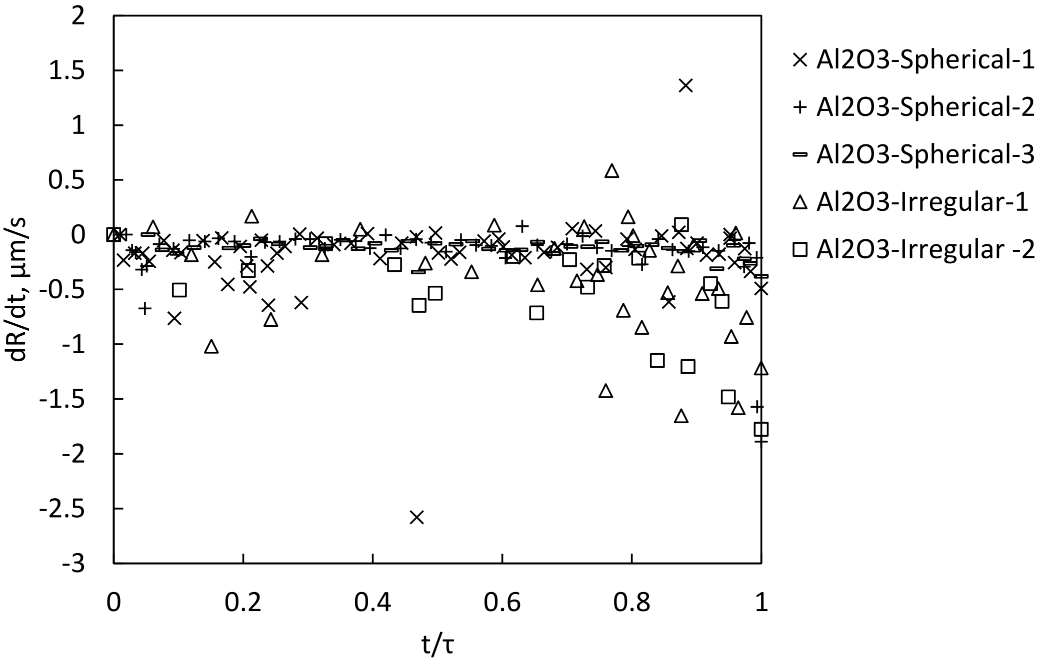

Figure 8-1 Comparison of rate of change in the size of regular and irregular alumina particle

8.3 Appendix A3 - Errors related to CSLM technique

The dissolution of inclusions in slag is studied by measuring the size change of a single particle as it dissolves in slag at steelmaking temperatures. There are many factors that can induce errors in measuring the dissolution kinetics of inclusions in slag. The sources of errors and their effect are discussed as follows:

1. Errors in slag weight measurements and composition analysis

The process of slag preparation involves weight measurements of slag constituents to be mixed and ICP analysis of the samples after preparation. The variation in slag weight measurements was negligible as a scale with a precision of 3 digits was used to reproducibly weigh the slag powder. The slag was powdered before melting every time until the final slag was produced. Thus, the composition of slag did not vary much in terms of components; Al_2O_3, CaO, and SiO_2. The error in ICP measurements of the chemical composition of the slag was within 1 wt %.

2. Error in temperature measurements

The high-temperature experiments in CSLM was performed in a cylinder shape platinum crucible with 5 mm diameter and 5 mm height. The height of the pre molten slag inside the platinum crucible is generally 1 mm, measured from the base of the crucible. The platinum crucible was placed inside another alumina crucible of 9 mm diameter and 5 mm height. The alumina crucible was positioned on a sample holder which is a thin annular platinum disc. The base of the disc is welded to thermocouple wires. The temperature in the CSLM was controlled with a B type thermocouple. The accuracy of the B type thermocouple is 0.5% of 1550 °C, which is approximately 8 °C. The inclusion dissolution was measured at a position in space which was anywhere from the base of the platinum crucible to 1 mm from the base. Thus, there is a difference in temperature between the reaction site and the position where the temperature was measured. To account for this temperature difference, the thermocouple was calibrated. The calibration was done every 6 months, or every time a part of the CSLM was repaired or replaced. The calibration was performed by using a 99.5 % pure iron disc of 1 mm thickness.

3. Errors from size measurement

The CSLM uses image frames obtained from in situ observation for the measurement of the rate of dissolution of a single particle in slag. The principal source of error arises from the measurement of the size of the dissolving particle. In general, three sets of experiments were performed for reproducibility to obtain each set of size versus time data. To measure the particle size during dissolution, a border was manually drawn around the particle. The area within the enclosed boundary was measured using image analysis software ImageJ ^{TM}. This area was equated to the area of a circle. The radius of the circle was calculated, and it was used to represent the size of the dissolving particle. The size obtained from the area enclosed within the border is subjective. Therefore, in order to be consistent with measuring the particle size, three sets of boundaries are drawn around the particle. The boundaries are drawn such as to include the maximum area, the minimum area and an average area enclosed by the boundary. Thus, three sets of radius are obtained for each image. The relative standard deviation on the radius measurement for each image was within 1 %.

The error was further propagated when the rate-controlling mechanism was evaluated in terms of the shrinking core model using the radius-time data. For the chemical reaction control, the slope of R/R_0 versus time relation was used to estimate the chemical reaction rate constant. For the diffusion in boundary layer control mechanism, the (R/R_0)^2 versus time relation was used to determine the diffusion coefficient of the dissolving species. Where R is the radius measured at an instantaneous time and R_0 is the radius at time zero. If $c= R/R_0$ and $d =(R/R_0)$ ^2, the error on c and d is obtained as shown in equation 8.1 and 8.2 respectively. :

$$\delta c = \sqrt{\left(\frac{\partial c}{\partial R}\,\delta R\right)^2 + \left(\frac{\partial c}{\partial R_0}\,\delta R_0\right)^2} \qquad 8.1$$

Where δR and δR_0 are errors in instantaneous radius and initial radius. For the case of Al_2TiO_5 dissolution in a 23.2 Al_2O_3-30.5CaO-46.3 SiO_2 slag at 1550 °C, R_0 is 93 µm, δR_0 =93*1%= 0.93 µm, R=79µm, δR_0=79*1% µm=0.79, c=0.85.

$$\delta c = \sqrt{\left|\frac{1}{R_0}\delta R\right|^2 + \left|\frac{R}{R_0^2}\delta R_0\right|^2} \rightarrow \delta c = \sqrt{\left|\frac{1}{93}0.79\right|^2 + \left|\frac{79}{93^2}0.93\right|^2} \rightarrow \delta c = 0.012$$

The percentage error in c = $\frac{\delta c}{c} * 100$ %= $\frac{0.012}{0.85} * 100$ %=1.4%

The same method of calculation was repeated to calculate the error in d. For the same set of values, the error in d can be calculated.

$$\delta d = \sqrt{\left(\frac{\partial d}{\partial R}\delta R\right)^2 + \left(\frac{\partial d}{\partial R_0}\delta R_0\right)^2} \qquad 8.2$$

$$\delta d = \sqrt{\left(\frac{2R}{R_0^2}\delta R\right)^2 + \left(\frac{2R^2}{R_0^3}\delta R_0\right)^2}$$

$$\delta d = \sqrt{\left|\frac{2*79}{93^2}0.79\right|^2 + \left|\frac{2*79^2}{93^3}0.93\right|^2} \rightarrow \delta d = 0.02$$

The percentage error in d = $\frac{\delta d}{d} * 100$ %= $\frac{0.02}{0.72} * 100$ %=2.8%

The error on the slope of straight line induces an error in the calculation of chemical reaction rate constant and diffusivity values. The error on the slope is calculated by considering the maximum variation in the R/R_0 and (R/R_0) ^2 values. The maximum and minimum values of the slope were calculated from maximum and minimum values of x and y variables. For the set of data used, the error in slope was approximately 10%. The chemical reaction rate constant and diffusivity values are a linear function of the values of the errors. They can be represented as K_R=slope of R/R_0*constant and D=slope of

R/R_0^2*constant. Therefore, the error in the chemical reaction rate constant and diffusivity values due to an error in slope was approximately 10 %.

8.4 Appendix A4 - Summary of regression analysis of dissolution experiments

A large number of dissolution experiments were performed for this research. However, a few set of data from those experiments were used in the publications. Table 8-5 to Table 8-10 show the data from regression analysis of dissolution of alumina, aluminum titanate and titanium oxide in the three slags studied. A represents R/R_0-1 and B represents (R/R_0)^2-1 where A and B are obtained from the chemical reaction control and diffusion in boundary layer control of shrinking core model.

Table 8-5 Summary of the R^2 values for sapphire-slag 1 system at 1500 °C and 1550 °C

Temperature	Initial particle radius (µm)	R^2, A vs t (Chemical reaction control)	R^2, B vs t (Boundary layer diffusion control)
1500 °C	150	0.91	1
	175	0.98	0.93
	105	0.97	0.97
1550 °C	87	0.95	0.93
	120	0.99	0.96
	170	0.96	0.97

Table 8-6 Summary of the R^2 values for sapphire-slag 2 system at 1500°C, 1550°C, 1600 °C and 1650°C

Temperature	Initial particle radius (µm)	R^2, A vs t (Chemical reaction control)	R^2, B vs t (Boundary layer diffusion control)
1500 °C	159	0.95	0.95
	157	0.95	0.95
1550 °C	112	0.93	0.99
	88	0.93	0.99
1600 °C	78	1.0	0.96
	78	0.95	0.99
1650 °C	181	0.95	0.80
	280	0.96	0.72

Table 8-7 Summary of the R^2 values for aluminium titanate-slag 1 system at 1500°C and 1550°C

Temperature	Initial particle radius (µm)	R^2, A vs t (Chemical reaction control)	R^2, B vs t (Boundary layer diffusion control)
1500 °C	131	0.95	0.81
	122	0.95	0.98
	335	1.0	0.98
1550 °C	191	0.82	0.45
	113	0.97	0.73

Table 8-8 Summary of the R^2 values for aluminium titanate-slag 2 system at 1500°C and 1550°C

Temperature	Initial particle radius (µm)	R^2, A vs t (Chemical reaction control)	R^2, B vs t (Boundary layer diffusion control)
1500 °C	152	0.83	0.53
	335	0.97	0.91
	383	0.94	0.96
	134	0.62	0.65
	255	0.95	0.86
1550 °C	201	0.88	0.99

	451	0.88	0.95
	416	0.97	0.98

Table 8-9 Summary of the R^2 values for aluminium titanate-slag 3 system at 1500°C

Temperature	Initial particle radius (µm)	R^2, A vs t (Chemical reaction control)	R^2, B vs t (Boundary layer diffusion control)
1500 °C	311	0.95	1.0
	215	1.0	0.99

Table 8-10 Summary of the R^2 values for titanium oxide-slag 1 system at 1430°C

Temperature	Initial particle radius (µm)	R^2, A vs t (Chemical reaction control)	R^2, B vs t (Boundary layer diffusion control)
1430 °C	287	0.97	0.98
	301	0.96	0.94
	278	0.93	0.96